Spring 2019

Effects of uncertainty refinement on satellite collision probability

Bruce Thomas Morrison

Department:

EFFECTS OF UNCERTAINTY REFINEMENT ON SATELLITE COLLISION PROBABILITY

by

BRUCE THOMAS MORRISON

A THESIS

Presented to the Graduate Faculty of the

MISSOURI UNIVERSITY OF SCIENCE AND TECHNOLOGY

In Partial Fulfillment of the Requirements for the Degree

MASTER OF SCIENCE IN AEROSPACE ENGINEERING

2019

Approved by

Kyle J. DeMars, Advisor
Serhat Hosder
Henry Pernicka

ABSTRACT

Due to the drastic increase in orbital debris about the Earth, the likelihood for new and current mission satellites to collide with other objects grows. When a mission satellite is placed in a highly populated orbit in the vicinity of other satellites or debris, it is necessary to consider the probability of collision to assess any possible conjunctions. The computation of the collision probability is heavily dependent on the relative position and velocity of the objects during conjunction, as well as the combined covariance. There are two main types of analytic collision probability computations; the first assumes that the objects in conjunction are characterized by linear relative motion at the time of closest approach, and the second assumes that the objects will maintain highly nonlinear relative motion.

The size of the covariances of both objects plays a significant role in the computation of collision probability. In order to decrease the size of the combined covariance, both objects will be tracked through time, generating measurements from the states of position and velocity. These measurements are utilized by an extended Kalman filter to develop a more confident estimate of the relative position, velocity, and covariance, which will affect the size of the combined covariance and ultimately alter the probability of collision. This allows a method of analyzing the probability of collision for any case, as it will no longer be a single and somewhat arbitrary value.

To further understand the analysis on the probability of collision, Monte Carlo trials are conducted to validate the effects of observation on the probability of collision. These trials offer insight to every collision probability application and can be utilized more effectively to gage whether or not a satellite should maneuver.

ACKNOWLEDGMENTS

Firstly, I would like to thank my advisor, Dr. Kyle DeMars; your guidance has been crucial to my success as a graduate student. I appreciate your patience as I struggled understanding various topics; I will always value your insights and professional judgment. Studying under you has greatly increased the quality of my technical work and I appreciate you sacrificing so much of your time to help me complete this thesis during such a time crunch.

Secondly, I would like to thank my committee members, Dr. Henry Pernicka and Dr. Serhat Hosder. The information I learned from your lessons has provided me with tools that I have been able to utilize to accomplish many tasks; I look forward to applying these concepts to future projects. Your influence both inside and outside of the classroom will continue to inspire my professional career.

I would also like to give an immense thank you to my parents for working so hard and allowing me the opportunity to achieve my dreams. For that I will always be thankful. You are truly the reason for my ambitious goals, and my driving force to continue working hard.

Finally, I would like to thank all of my lab-mates who battled alongside me throughout this endeavor. Specifically I would like to thank Christine Schmid for listening to me ramble as I would think out-loud and assisting me where I needed help. I would like to thank the entire lab and my friends: Cameron Helmuth, Gunner Fritsch, Kari Ward, Matt Gualdoni, James Brouk, Sasha Petrenko, James McCabe, Casey Smith, and Kenny Kratzer. You all made coming into the lab every day a pleasant experience and the support you offered to not only me but to each other has always been inspiring.

TABLE OF CONTENTS

Page

LIST OF ILLUSTRATIONS

Figure Page

LIST OF TABLES

Table Page

SECTION

1. INTRODUCTION

Due to the drastic increase of orbiting satellites, interest in potential collisions between mission satellites and orbital debris or some other satellite has grown. NASA defines orbital debris as any man-made object in Earth's orbit without a purpose (Hall (2019)). In 2013, NASA reported more than 21,000 pieces of tracked orbital debris that were at least the size of a softball. NASA also estimates around 500,000 pieces of debris about the size of a marble and at least 100 million pieces of tiny, untrackable orbital debris (Hall (2019)). Each new satellite not only has to be "aware" of all this debris, but also of other satellites. As of 2014, there were about 1,100 orbiting active satellites, and this number has only risen exponentially since then. New satellites have to be aware of the debris population as well as other satellites.

Interestingly, most of the Earth's debris originates from man-made objects launched into space over the last fifty years. The first examination of orbital debris affecting a mission spacecraft was during the Apollo program in 1966. At the time, the debris was sufficiently low enough that no action had to be taken, but the increase in debris over these fifty years could be detrimental to future launches (Kessler (1981)). It is a well-known fact that the first artificial satellite placed in orbit was Sputnik I by the Soviet Union on October 2nd, 1957. However, Sputnik I did not contribute to the cloud of orbital debris, as it burned up in the atmosphere during reentry a month after launch; the core stage of the rocket was soon to follow a month later. The debris issue arguably began with the launch of Vanguard I by the United States in March, 1958. This satellite stopped transmitting six years after its launch, but remains in a medium Earth orbit (MEO) to this day and is expected to remain for nearly 200 years (Green and Lomask (1970), and Easton and Votaw (1959)). In 1959,

two additional Vanguard satellites were launched, and they too remain inactive in similar orbits. All three of these satellites are now considered as orbital debris. Currently, the United States Air Force catalogs every object larger than 10 cm, that enters Earth's orbit. When a cataloged object is damaged, each new fragment is then cataloged with a specific, individual identifier (Kelso (1997)). There are a few ways that orbital debris is generated from these mission satellites: mission related operations, accidental debris, and intentional acts resulting in debris.

Mission related debris is formed from the normal implementation, use, and disintegration of mission satellites. For example, when a satellite detaches from the upper stage of a launch vehicle, an explosive bolt is used to separate the components. This explosion causes small fragments to break off from the launch vehicle, creating debris. This debris may seem trivial and small, but in some orbits, these pieces of "junk"can travel up to tens of km/s, which will seriously damage a mission satellite (Council (1995)). Another source of debris is when a protective shield or some piece of hardware disintegrates and separates entirely from a decommissioned satellite.

Accidental debris is generated from unforeseen events, such as an astronaut losing equipment while working on the exterior of the International Space Station (ISS). In 1965, a thermal glove drifted out of an open hatch of the Gemini IV capsule. In 1966, Mike Collins dropped a camera while working on the outside of the Gemini X capsule. In 2008, Heidemarie Stefanyshyn-Piper lost a tool-bag, roughly the size of a backpack, while cleaning a spill outside the ISS (Hall (2019)). However, accidental debris is mostly from the result of a collision or explosion.

During the Cold War, the ability to control the realm of space came into question and introduced the means of intentional debris. Between 1968 and 1985, the United States and the Soviet Union developed anti-satellite weapons. The United States developed a weapon that would destroy a target with a direct impact. The Soviet Union designed a weapon to explode near a target and use the shrapnel to destroy the satellite. Both methods

would exponentially increase the amount of orbiting debris. By 1990, twelve tests of these weapons had produced 7% of the cataloged orbital debris (U.S. Congress (1990)). Unfortunately, these actions were not limited to the duration of the Cold War; in 2007, China destroyed a Chinese weather satellite using a ballistic missile. Similarly, in 2019, India destroyed a satellite in low Earth orbit using a ground-to-space missile.

The issue of debris now orbiting the Earth causes potential catastrophic events for any current or future mission satellites. This crisis will only increase as it is becoming more difficult to regulate the number of satellites that other countries or corporations launch into orbit. For example, SpaceX is currently working on a satellite constellation project called Starlink to implement a new space-based Internet communication system. In November of 2018, the FCC approved SpaceX to launch 7,518 broadband satellites, in addition to the 4,425 satellites that were approved in March earlier that year (Harris (2019)). Eventually, all of these satellites will be decommissioned and could potentially cause more debris if there is not a successful means of destroying the constellation during reentry.

With the vast amount of orbiting debris, the likelihood of a collision increases for every new satellite. As a result, each collision contributes more debris to the cloud, thus further increasing the likelihood of future collisions. The current way of detecting a collision is by computing the probability that a mission satellite will come into contact with debris or another satellite, then comparing that value to some arbitrary user set threshold value. If the probability of collision is larger than the threshold value, a maneuver is performed to place the satellite onto a new trajectory. Picking the threshold value is somewhat arbitrary; it is essentially a comfort number for the user to discern what amount of probability of collision is acceptable not to maneuver. The order of this threshold value is generally between 10^{-4} and 10^{-5} (Chan (2008)). However, this threshold value may require some satellites to maneuver when the debris would not have collided, wasting precious fuel. An additional issue with maneuvering is that the primary spacecraft could be placed into a new trajectory

with a new collision from a different secondary object. One of the goals for this work is to investigate a method of observing and tracking the objects through time in order to better describe the probability of collision.

This work presents various methods to calculate the probability of a collision between a primary spacecraft and some arbitrary, secondary object. The computation is heavily dependent on the relative positions, velocities, and the sum of the covariances for both objects at the time of closest approach. The emphasis of this work is not only to compare the presented methods but also to analyze the effects of observations on the probability of collision. Additional measurements from the observations tend to shrink the combined covariance of the two objects, altering the probability of collision. Depending on the case, the collision may be proven false, or it may become more definitive. The overall result in the observation method increases the understanding of all collision probability computations, producing an alternative to maneuvering to avoid an imminent collision.

This work defines the relative encounter frame; where all collision probabilities will be computed, in Section 2 as well as present preliminary Monte Carlo simulations. Section 3 discusses analytical methods that assume linear relative motion, as well as analytical methods leveraging the assumption of nonlinear relative motion to compute the probability of collision. Section 4 introduces the concept of taking measurements on the objects traveling through time, while Section 5 analyzes the effects of these measurements on the computation of collision probability. The conclusion to this work is provided in Section 6.

2. BACKGROUND

Currently, the most accepted model for determining the probability of collision revolves around assuming a Gaussian distribution to describe the position uncertainty for each object. The probability of collision is heavily dependent on a Gaussian assumption on the distribution of the relative positions, but there has been some work on approximating the collision probability if this assumption is not entirely Gaussian by utilizing Gaussian mixtures (DeMars *et al.* (2014)). Therefore, the probability computation for a colliding pair of objects is formulated in terms of a combined covariance matrix producing a general Gaussian distribution in three dimensions. The combined covariance matrix is found by summing the individual covariance matrices of each object, expressed in the same coordinate system. This is possible if the measurements used for the orbit determination for each object are independent or uncorrelated, which is true for most mission applications (Coppola *et al.* (2005)).

This work assumes that the knowns are initial position, velocity, and respective covariances for each object, given in some inertial frame (usually Earth Centered Inertial frame) at epoch. The state vectors contain the respective position and velocities, such that

$$\mathbf{x}_p = \begin{bmatrix} x_p, & y_p, & z_p, & \dot{x}_p, & \dot{y}_p, & \dot{z}_p \end{bmatrix}^T \quad \text{and} \quad \mathbf{x}_s = \begin{bmatrix} x_s, & y_s, & z_s, & \dot{x}_s, & \dot{y}_s, & \dot{z}_s \end{bmatrix}^T,$$

where p denotes the primary spacecraft and s denotes the secondary object. This work presents a comparison between various computational methods utilizing six of Alfano's 12 cases (Alfano (2009)) outlined in Section 2.3.

The states are propagated through time with the covariance using a simple two body propagator to a point of conjunction, defined as the point of minimum separation distance between the primary spacecraft and secondary object. This point of conjunction is

known as the time of closest approach (TCA) and will be referred to as such. At TCA, the positional covariance matrices of each object are summed and centered about the secondary object. Similarly, the volume of each object will be combined and attributed to the primary spacecraft as shown in Figure 2.1. For the scope of this work, the volume of each object can be approximated by circumscribing spheres of radius r_p and r_s for the primary spacecraft and secondary object, respectively. A combined hard-body sphere is then generated with radius $R_a = r_p + r_s$ and is centered about the primary spacecraft.

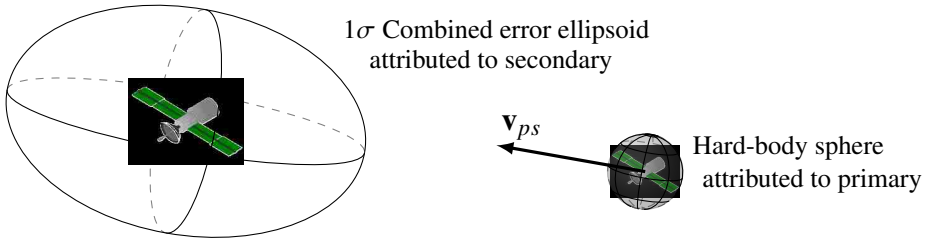

Figure 2.1. Imminent collision between two objects

A collision may occur if the hard-body sphere occupies the same space as the combined covariance ellipsoid. Over the span of the encounter, the hard-body sphere sweeps out a cylindrical volume through the combined covariance ellipsoid as shown in Figure 2.2.

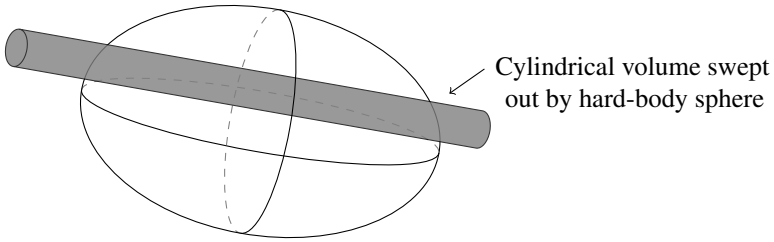

Figure 2.2. Cylinder swept out through error ellipsoid

The general, applicable case follows this trend of rectilinear motion during the encounter region; for the remainder of this work, these cases will be referred to as linear cases. The linearity of a case is apparent if the relative encounter velocity causes a straight cylinder that is larger than the distance traversed through a $m\sigma$ shell. The value m is a user defined scalar that will alter the size of the covariance shell, typically the user should set

this value to be between 3 and 8. This range will increase the volume of the shell, encompassing conjunction possibilities from 97.070911% to 99.999999% (Alfano (2009)). The initial covariance data at epoch used in this work will be given as 1σ, the user must scale this by the factor m to accommodate a larger encounter region, producing accurate results. There are rare cases when the relative velocity is too low to meet the linearity requirement and the cylinder curves throughout the encounter; these cases are referred to as nonlinear and will be examined further in later sections. The collision probability is then obtained by integrating the relative position probability density function over the swept out volume during the encounter. The relative position probability density between the primary spacecraft and the secondary object is given by

$$f(x, y, z) = \frac{1}{\sqrt{(2\pi)^3|\mathbf{C}|}}\exp(-\frac{1}{2}\mathbf{r}_{ps}\mathbf{C}^{-1}\mathbf{r}_{ps}),$$

where $\mathbf{r}_{ps}$ is the relative position between the primary spacecraft and the secondary object, and $\mathbf{C}$ is the combined covariance matrix. The encounter frame will be thoroughly defined in later sections, but let the $\hat{y}$-axis be along the relative velocity direction from the secondary object to the primary spacecraft. Let the $\hat{z}$-axis be defined along the direction of the cross product between the primary spacecraft's velocity vector and the secondary object's velocity vector. The $\hat{x}$-axis then completes the right-handed triad. The origin of this coordinate system is centered on the secondary object. Therefore, the probability of collision is

$$P = \iiint_V f(x, y, z)dxdydz, \tag{2.1}$$

where V is the volume swept out in the covariance ellipsoid by the sphere of radius R_a. During the encounter, the relative trajectory of the two objects is assumed to be a straight line. From a quantitative view, the orbiting velocities are of the order of several km/s and the time spent in the encounter region is only a fraction of a second or at most a few seconds, so the gravitational effects are negligible. This allows the trajectories to follow rectilinear

motion over a large region− tens or hundreds of standard deviations, which is much larger than the 3σ required for linearity. Producing a long cylinder swept out by the volume of the hard-body sphere, essentially extending along the $\hat{y}$-direction from $-\infty$ to $+\infty$. Thus, simplifying the 3-dimensional probability density function (pdf) to a 2-dimensional pdf. The relative position is described by the following bivariate Gaussian pdf

$$f(x,z) = \frac{1}{2\pi\sigma_x\sigma_z\sqrt{1-\rho_{xz}^2}} \times \exp\left(-\left[\left(\frac{x}{\sigma_x}\right)^2 - 2\rho_{xz}\left(\frac{x}{\sigma_x}\right)\left(\frac{z}{\sigma_z}\right) + \left(\frac{z}{\sigma_z}\right)^2\right] / \left(2(1-\rho_{xz}^2)\right)\right), \tag{2.2}$$

where σ_x and σ_z are the standard deviations in the $\hat{x}$-direction and $\hat{z}$-direction, respectively; with the correlation, ρ_{xz}, between the two. The probability of collision becomes

$$P = \iint_A f(x,z)dxdz, \tag{2.3}$$

where A is the collision cross section area circle with radius R_a. The methods presented in the following sections approximate the collision probability based on the relative rectilinear motion between the orbiting objects.

2.1. THE ENCOUNTER FRAME

The analytical methods for computing collision probability between orbiting objects require the positions, velocities, and respective covariances of each object to be converted into a relative encounter frame at TCA. During the time of closest approach, the encounter frame is defined with the $\hat{y}_m$-axis in the direction of the relative velocity of the

primary spacecraft from the secondary object (Chan (2008)), such that

$$\begin{aligned} \mathbf{v}_{ps} &= \mathbf{v}_p - \mathbf{v}_s \\ \hat{y}_m &= \frac{\mathbf{v}_{ps}}{||\mathbf{v}_{ps}||}. \end{aligned} \tag{2.4}$$

The $\hat{z}_m$-axis is defined in the direction of the cross product of the two velocity vectors

$$\begin{aligned} \mathbf{n} &= \mathbf{v}_p \times \mathbf{v}_s \\ \hat{z}_m &= \frac{\mathbf{n}}{||\mathbf{n}||}. \end{aligned} \tag{2.5}$$

The $\hat{x}_m$-axis completes the right-handed triad. The $(\hat{x}_m,\hat{z}_m)$-plane is referred to as the encounter plane. The combined covariance ellipsoid and the hard-body sphere are projected onto this encounter plane as an ellipse and circle respectively. This $(\hat{x}_m,\hat{y}_m,\hat{z}_m)$ coordinate system acts as an intermediate encounter frame transformed from the inertial frame to the utilized encounter coordinate frame, which requires another transformation. The first transformation uses the matrix $\mathbf{T}_i^m$, defined by a directional cosine matrix relating the inertial frame to the $(\hat{x}_m,\hat{y}_m,\hat{z}_m)$ coordinate system.

$$\mathbf{T}_i^m = \begin{bmatrix} \hat{x}_i \cdot \hat{x}_m & \hat{x}_i \cdot \hat{y}_m & \hat{x}_i \cdot \hat{z}_m \\ \hat{y}_i \cdot \hat{x}_m & \hat{y}_i \cdot \hat{y}_m & \hat{y}_i \cdot \hat{z}_m \\ \hat{z}_i \cdot \hat{x}_m & \hat{z}_i \cdot \hat{y}_m & \hat{z}_i \cdot \hat{z}_m \end{bmatrix}. \tag{2.6}$$

The $(\hat{x}_i,\hat{y}_i,\hat{z}_i)$ frame here denotes the inertial frame and should not be confused with the $(\hat{x},\hat{y},\hat{z})$ encounter frame defined later. Once transformed, the encounter frame is then rotated about the $\hat{y}_m$-axis until a new plane defines the $\hat{x}$-axis such that the primary object is nominally located at the point $(x_e,0,0)$, where x_e is the nominal miss distance, otherwise known as the minimum separation distance at closest approach. The new $\hat{y}$-axis is located along the same direction as the $\hat{y}_m$-axis. The $\hat{z}$-axis completes the right-handed triad. It is

an important note that the $(\hat{x},\hat{z})$-plane coincides with the $(\hat{x}_m,\hat{z}_m)$-plane, but that the $\hat{x}$-axis does not coincide with the $\hat{x}_m$-axis, and that the $\hat{z}$-axis does not coincide with the $\hat{z}_m$-axis. To meet the condition defined for the $\hat{x}$ axis, let it be along the direction of the relative position vector $\mathbf{r}_{ps}$ in the $(\hat{x}_m,\hat{y}_m,\hat{z}_m)$ coordinate frame, given by

$$\begin{aligned} \mathbf{r}_{ps} &= \mathbf{r}_p - \mathbf{r}_s \\ \hat{x} &= \frac{\mathbf{r}_{ps}}{||\mathbf{r}_{ps}||}. \end{aligned} \tag{2.7}$$

The rotation to the new encounter frame axes requires a transformation matrix $\mathbf{T}_m^e$, which is defined by a rotation about the $\hat{y}_m$-axis, utilizing the angle γ. This transformation matrix is

$$\mathbf{T}_m^e = \begin{bmatrix} \cos(\gamma) & 0 & \sin(\gamma) \\ 0 & 1 & 0 \\ -\sin(\gamma) & 0 & \cos(\gamma) \end{bmatrix}, \tag{2.8}$$

where, the rotation angle γ is

$$\gamma = \arctan\left(\frac{\mathbf{r}_{ps,z}}{\mathbf{r}_{ps,x}}\right).$$

The positions, velocities, and covariances must be transformed from the inertial frame to the $(\hat{x},\hat{y},\hat{z})$ encounter coordinate system at TCA. Once in this frame, the two individual covariance matrices can be summed to form the combined covariance matrix

$$\mathbf{C} = \mathbf{C}_p + \mathbf{C}_s,$$

where $\mathbf{C}_p$ and $\mathbf{C}_s$ are the primary spacecraft's covariance and the secondary object's covariance, respectively, at TCA. Figure 2.3 illustrates how the two objects will be oriented in the two encounter coordinate planes.

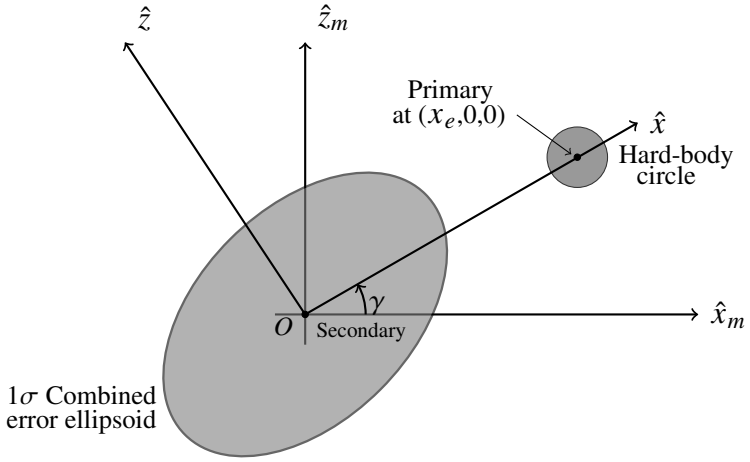

Figure 2.3. Rotation from the $(\hat{x}_m, \hat{z}_m)$ plane to the $(\hat{x}, \hat{z})$ plane

In this $(\hat{x},\hat{y},\hat{z})$ encounter coordinate system, the combined covariance becomes

$$\mathbf{C} = \begin{bmatrix} \sigma_{xx}^2 & \rho_{xy} & \rho_{xz} \\ \rho_{xy} & \sigma_{yy}^2 & \rho_{yz} \\ \rho_{xz} & \rho_{yz} & \sigma_{zz}^2 \end{bmatrix}.$$

This yields a very undesirable cross term when any of the correlation terms ρ_{ij} are non-zero. Meaning, the Gaussian pdf used to describe the relative position can be reduced by eliminating the correlation terms, ρ_{ij}. To simplify the analysis, the $(\hat{x},\hat{z})$ plane needs to be rotated again to a $(\hat{x}',\hat{z}')$ plane, defined along the principle axes of the combined covariance ellipsoid. The transformation matrix $\mathbf{T}$ that defines this rotation can be found by taking the transpose of an eigenvector matrix. Taking the eigenvector of any covariance matrix will produce the directions of the principle axes for the matrix. This transformation matrix defines the $\hat{x}'$-axis along the major axis of the combined error ellipsoid, and the $\hat{z}'$-axis along the minor axis. This transformation matrix can also be simply defined by using the properties of the combined covariance matrix to obtain the angle α and using another rotation transformation about the $\hat{y}'$-axis. This is done by calculating α using Equation (2.9) and

plugging the result into Equation (2.8), replacing the γ.

$$\alpha = \frac{1}{2}\arctan\left(\frac{2\rho_{xz} - \sigma_{xx}\sigma_{zz}}{\sigma_{xx}^2 - \sigma_{zz}^2}\right) \tag{2.9}$$

$$\mathbf{T} = \begin{bmatrix} \cos(\alpha) & 0 & \sin(\alpha) \\ 0 & 1 & 0 \\ -\sin(\alpha) & 0 & \cos(\alpha) \end{bmatrix}.$$

Because the ellipsoid and the sphere have been projected onto this 2-dimensional ($\hat{x}'$,$\hat{z}'$)-plane, we only need to focus on the $\hat{x}'$ and $\hat{z}'$ elements for further analysis. This rotation yields the covariance matrix $\mathbf{C}'$:

$$\mathbf{C}' = \begin{bmatrix} \sigma_x'^2 & 0 & 0 \\ 0 & \sigma_y'^2 & 0 \\ 0 & 0 & \sigma_z'^2 \end{bmatrix}.$$

Once the position, velocities, and combined covariance are transformed into this ($\hat{x}'$,$\hat{z}'$) encounter plane, they are input into the collision probability computations.

2.2. MINIMUM SEPARATION DISTANCE

A general process to calculate the nominal miss distance or minimum separation distance at TCA is given in (Chan (2008)). As before, let $\mathbf{v}_p$ and $\mathbf{v}_s$ denote the velocities of the primary spacecraft, P, and the secondary object, S. Also, denote $\mathbf{n}$ as the vector defined by the cross product of these two vectors, shown in Equation (2.5). Note that the two velocity vectors are generally assumed to be nonparallel, as cases with parallel vectors are virtually nonexistent; however, Chan provides some insight on these rare cases (Chan (2008)). Two planes are constructed that are perpendicular to $\mathbf{n}$: one plane contains the vector $\mathbf{v}_p$ and the other contains the vector $\mathbf{v}_s$. Let H denote the height between these two planes.

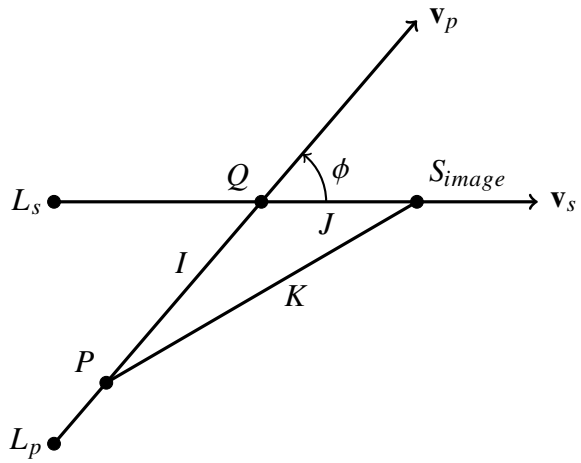

Figure 2.4. Primary plane with projected secondary elements

To analyze the rectilinear motion of the two objects, they must be comparable within a single plane. Therefore, let the vector $\mathbf{v}_s$ be projected onto the plane containing $\mathbf{v}_p$. As the secondary object moves along the path of $\mathbf{v}_s$, its projected image S_{image} moves along the path of the projected $\mathbf{v}_s$. This can be seen in Figure 2.4. Let Q denote the intersection point between $\mathbf{v}_p$ and the projected $\mathbf{v}_s$, and let ϕ be the angle between them. Figure 2.4 also illustrates points P and S_{image} at any instant of time, t, where I and J denote their respective distances from point Q. The value K is the distance between the primary spacecraft, P, and the projection of the secondary spacecraft, S_{image}, using the law of cosines provides

$$K^2 = I^2 + J^2 \pm 2IJ\cos\phi. \tag{2.10}$$

The magnitudes of $\mathbf{v}_p$ and $\mathbf{v}_s$ can be related by some scaling, λ, such that

$$||\mathbf{v}_s|| = \lambda||\mathbf{v}_p||,$$

the scalar λ must then satisfy the relationship of

$$\frac{dJ}{dI} = \pm\lambda. \tag{2.11}$$

The necessary condition for achieving the minimum distance, K, is

$$\frac{dK}{dI} = 0. \tag{2.12}$$

Substituting Equations (2.11) and (2.12) into Equation (2.10), one obtains the following condition for minimum separation in the projective plane:

$$\frac{I^*}{J^*} = \pm\left(\frac{\lambda - \cos\phi}{1 - \lambda\cos\phi}\right), \tag{2.13}$$

where I^* and J^* denote the values of I and J at minimum separation, respectively. At the point of minimum separation, the points P, Q, and S_{image} form a set of similar triangles, thus simplifying analysis on this system. Using Equation (2.13) to substitute for J in Equation (2.10) yields

$$(K^*)^2 = \kappa^2 (I^*)^2, \tag{2.14}$$

where K^* is the value of K at minimum separation, and κ is

$$\kappa^2 = 1 + \left(\frac{1 - \lambda\cos\phi}{\lambda - \cos\phi}\right)^2.$$

Now, considering the encounter between the two objects in the three-dimensional region as shown in Figure 2.5, let M denote the minimum separation distance between them, such that

$$M^2 = H^2 + (K^*)^2.$$

Let L_p and L_s denote the distances of the primary spacecraft P and secondary image S_{image} from the point Q at time t_0. Let t_m denote the time corresponding to the point of minimum separation. Equating the time it takes each object to reach the point of minimum separation yields

$$\frac{L_p - I^*}{v_p} = \frac{L_s \pm J^*}{v_s}. \tag{2.15}$$

It is important to note that the sign of J^* is dictated by the placement of S_{image} in relation to the point Q. If the projected image is to the right of Q then the sign is positive, and to the left of point Q, the sign is negative. Substituting Equation (2.13) into Equation (2.15)

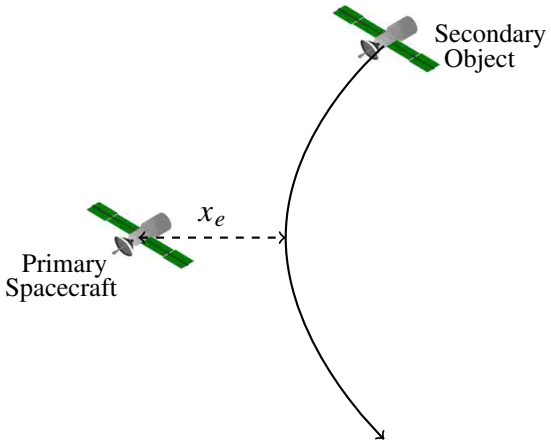

Figure 2.5. Minimum separation distance at TCA (modified from Chan (2008))

yields

$$L_p - I^* = \frac{1}{\lambda}\left[L_s + I^*\left(\frac{1-\lambda\cos\phi}{\lambda-\cos\phi}\right)\right]. \tag{2.16}$$

Solving for I^* from Equation (2.16), it follows that

$$I^* = \frac{(\lambda L_p - L_s)(\lambda - \cos\phi)}{1 - 2\lambda\cos\phi + \lambda^2}. \tag{2.17}$$

The time to minimum separation is therefore given by

$$t_m = t_0 + \left(\frac{L_p - I^*}{v_p}\right).$$

The next step is to calculate the beginning positions of each object on this primary plane, L_p for the primary spacecraft and L_s for the secondary object. To do this, the positions and velocities of each object must be in the $(\hat{x}_m,\hat{y}_m,\hat{z}_m)$ intermediate encounter frame defined in Section 2. Therefore, the state vectors for both objects at TCA must be transformed from the inertial (x_i,y_i,z_i) frame to the (x_m,y_m,z_m) frame using the defined transformation matrix

$\mathbf{T}_i^m$, resulting in

$$\begin{aligned}
\mathbf{R}_p &= \mathbf{T}_i^m \mathbf{r}_p \\
\mathbf{R}_s &= \mathbf{T}_i^m \mathbf{r}_s \\
\mathbf{V}_p &= \mathbf{T}_i^m \mathbf{v}_p \\
\mathbf{V}_s &= \mathbf{T}_i^m \mathbf{v}_s .
\end{aligned} \tag{2.18}$$

The vectors $\mathbf{R}_p = (X_p, Y_p, Z_p)$ and $\mathbf{R}_s = (X_s, Y_s, Z_s)$ are projected onto the (X,Y) plane by dropping the Z components. These projected points are denoted by $A = (X_p, Y_p)$ and $B = (X_s, Y_s)$. The velocity vectors are also projected onto this plane and have directional components $\mathbf{V}_p = (U_p, V_p)$ and $\mathbf{V}_s = (U_s, V_s)$. There are now two straight lines on the plane, one passing through point A with the $\mathbf{V}_p$ components and one passing through the point B with the $\mathbf{V}_s$ components. The equations of these lines are

$$Y = \frac{V_p}{U_p}(X - X_p) + Y_p \tag{2.19}$$

$$Y = \frac{V_s}{U_s}(X - X_s) + Y_s . \tag{2.20}$$

These lines will intersect at some point $D = (X_i, Y_i)$. Setting these equations equal and solving for X_i yields

$$X_i = \frac{\left(Y_s - Y_p\right) + \left(V_p/U_p\right)X_p - \left(V_s/U_s\right)X_s}{\left(V_p/U_p\right) - \left(V_s/U_s\right)} \tag{2.21}$$

Substituting Equation (2.21) into Equation (2.20) allows one to obtain an expression for Y_i as a function of X_i, and the components of the positions. Next, the distances L_p and L_s are computed in relation to point Q by

$$L_p = \sqrt{(X_i - X_p)^2 + (Y_i - Y_p)^2} \tag{2.22}$$

$$L_s = \sqrt{(X_i - X_s)^2 + (Y_i - Y_s)^2}. \tag{2.23}$$

Equations (2.22) and (2.23) are substituted into Equation (2.17) to obtain I^*, which is then used in Equation (2.14) to calculate the minimum separation, K^*, in the projection plane. The height between the planes, H, is given by

$$H = |\hat{\mathbf{n}} \cdot (\mathbf{r}_p - \mathbf{r}_s)|,$$

with the positional vectors, $\mathbf{r}_p$ and $\mathbf{r}_s$, in the (x_m, y_m, z_m) intermediate encounter frame. The minimum separation, M, in the three-dimensional space (x_e) is obtained by

$$x_e = M = \sqrt{H^2 + (K^*)^2}.$$

The value for the minimum separation distance, x_e, is extremely important when calculating the collision probability using any method because indicates if the hard-body sphere is within the volume of the combined covariance ellipsoid. Note that if the state vectors for both objects are correctly converted into the final $(\hat{x},\hat{y},\hat{z})$ encounter frame, then the relative distance in the $\hat{x}$-direction between the two objects should be equal to the minimum separation distance found through this process. There is some interesting work on using a chi-squared distribution of the minimum separation distance, rather than the Gaussian distribution describing relative position uncertainty, to approximate the probability of collision (Chan (2011)).

2.3. TEST CASES

Alfano presented twelve test cases that are useful when comparing methods for computing collision probability, this work utilizes six of the test cases. Most of the selected cases involve a primary spacecraft and a secondary object in geosynchronous Earth orbits (GEO), while the remaining cases operate in low Earth orbits (LEO). For three of the cases, the relative velocity between the primary and secondary objects is large, meaning that the distance traversed by the primary spacecraft through the encounter region is larger than the size of the ellipsoidal covariance shell, in direction of the relative velocity. The aforementioned straight cylinder is formed from the path of the primary traversing the encounter region, allowing the high relative velocity cases to be referred to as linear because the cylinder would be larger than the ellipsoid. The remaining three cases have low relative velocities, meaning that the cylinder is no longer straight, but is now curved, causing a nonlinear relative motion between the two objects during the encounter. These low relative velocity cases are referred to as nonlinear, Table 2.1 outlines the specific cases.

Table 2.1. Alfano's test cases

	Orbit	**Relative Velocity [m/s]**	**Linearity**	**Hard-body radius [m]**
Case 1	GEO	0.0141424	Nonlinear	15
Case 2	GEO	0.0141424	Nonlinear	4
Case 3	GEO	16.066923	Linear	15
Case 4	GEO	0.0190334	Nonlinear	15
Case 5	LEO	0.5196224	Linear	10
Case 6	LEO	0.1732265	Linear	10

The positions, velocities, and covariances for each object at both epoch and TCA can be found in the Appendix.

2.3.1. Case 1. Case 1 involves two satellites in GEO, with nonlinear relative motion. The nominal miss distance, x_e, is less than the combined object radius, $R_a = 15$ [m], at the point of closest approach, meaning that all methods computing the probability of col-

lision should register some finite value that a collision could occur. The objects in this case will reach conjunction (i.e. time of closest approach) 280,800 seconds after epoch, with a relative velocity of 0.0141424 [m/s]. This low relative velocity indicates that the primary will spend a vast amount of time in the encounter region, possibly tens of thousands of seconds.

2.3.2. Case 2. Case 2 is identical in trajectory and covariance to Case 1, but has a smaller combined object radius, $R_a = 4$ [m]. At TCA, the combined hard-body will only be partially encompassed by the ellipsoid, meaning that there should be a collision recorded, but it should be less than the collision probability computed from Case 1. Case 1 and 2 are valuable assets when analyzing methods because the cases are easily comparable. Due to Case 2 having the exact trajectories and covariances as Case 1, then, the objects will reach the conjunction at the same time, 280,800 seconds after epoch, with a relative velocity of 0.0141424 [m/s]. This low relative velocity indicates that the primary will spend a vast amount of time in the encounter region, possibly tens of thousands of seconds.

2.3.3. Case 3. Case 3 involves linear relative motion between two objects in GEO, where the nominal miss distance at TCA is less than the combined object radius, $R_a = 15$ [m], meaning that the methods presented in this work should produce some probability of collision. Case 3 and Case 1 have the same hard-body radius, offering a nice way of comparing a nonlinear and linear case. The objects in this case will reach the conjunction 280,800 seconds after epoch, with a relative velocity of 16.0669 [m/s]. The relative velocity in Case 3 is orders of magnitude larger than the relative velocity of any other case, which could prove detrimental to the computation of some methods. This high relative velocity indicates that the primary object will be in the encounter region for fractions of a second.

2.3.4. Case 4. Case 4 involves two objects in GEO with nonlinear relative motion, where the nominal miss distance is greater than the combined object radius, $R_a = 15$ [m]. The objects in this case will reach the conjunction 250,560 seconds after epoch, with a relative velocity of 0.0190334 [m/s]. This is among the lowest relative velocity for the

cases in GEO, which could have just as much of an effect on the computational methods as Case 3. The low relative velocity enables highly nonlinear motion in this specific case, consequently, most of the collision probability will not be generated about TCA, like most cases, but instead throughout the encounter region.

2.3.5. Case 5. Case 5 involves two LEO objects, where the nominal miss distance at TCA is less than the combined object radius, $R_a = 10$ [m]. The parameters in Case 5 offer an inverse scenario to that of Case 2; where the primary spacecraft in Case 2 was only partially inside the ellipsoid, the primary in Case 5 is completely within the ellipsoid. All methods to calculate collision probability should result in a probability for Case 5. The objects in this case will reach the conjunction 172,800 seconds after epoch, with a relative velocity of 0.5196224 [m/s]. Case 5 and 6 have the shortest time to conjunction out of any of the methods, meaning that the covariances of each object in these cases could be lower than the other four cases, resulting in smaller ellipsoids.

2.3.6. Case 6. Case 6 also involves two LEO objects, where the nominal miss distance at TCA is less than the combined object radius, $R_a = 10$ [m]. Case 6 is unique due to the nature of the relative velocity between the two objects, the path generated from the relative velocity by the primary spacecraft creates a straight cylinder spanning longer than the ellipsoid, but just barely. Meaning, that this relative velocity is right on the edge of being low, so some algorithms could treat this as a nonlinear case. The objects in this case will reach the conjunction 172,800 seconds after epoch, with a relative velocity of 0.1732265 [m/s].

2.4. THE MONTE CARLO METHOD

An accurate form of calculating spacecraft collision probability is by utilizing a Monte Carlo simulation with a sufficient number of samples. This is done by generating samples from a Gaussian distribution about the mean using the covariance and essentially counting how many of those samples collide with each other. The general process for

the Monte Carlo method involves propagating given position, velocity, and covariances to the point of conjunction. Then at TCA, generate n samples about the mean using the covariance. Setting the number of samples, n, to 1×10^8 has been proven to be sufficient (Alfano (2009)). The samples can be generated by taking the lower triangular Cholesky factorization of both objects' full state covariances at TCA. The Cholesky factor is defined as $\mathbf{P} = \mathbf{S}\mathbf{S}^T$. The samples are generated about the mean as

$$\mathbf{x}_p = \mathbf{m}_{p,TCA} + \mathbf{S}_p \boldsymbol{\nu}_1 \tag{2.24}$$

$$\mathbf{x}_s = \mathbf{m}_{s,TCA} + \mathbf{S}_s \boldsymbol{\nu}_2, \tag{2.25}$$

where $\mathbf{m}$ is the states, position and velocity, of each object at TCA, $\boldsymbol{\nu}_1$ and $\boldsymbol{\nu}_2$ are vectors of normally distributed random numbers. It is important to note that the randomized vector for both populating equations above is different. All of the samples are then converted into Keplerian orbital elements from Cartesian (Prussing and Conway (2013)) and (Hintz (2008)), i.e.

$$\left[x, y, z, \dot{x}, \dot{y}, \dot{z}\right] \Rightarrow \left[a, e, i, \Omega, \omega, M\right],$$

where the inputs are the Cartesian positions and velocities of each object $(x, y, z, \dot{x}, \dot{y}, \dot{z})$, a is the semi-major axis of the elliptical orbit, e is the eccentricity of the orbit, i is the inclination, Ω is the right ascension of the ascending node, ω is the argument of periapsis, and M is the mean anomaly. These Keplerian samples are then propagated both forward and backward in time one quarter of the primary spacecraft's orbital period from TCA. This one quarter of an orbit in each direction is sufficient to encompass the entire encounter region, this will be thoroughly shown in Section 3. This becomes the span of the conjunction that is analyzed for the collision probability and should encompass half an orbital period (Alfano (2009)). For all time steps, the Keplerian orbital elements are converted back into Cartesian coordinates. Then, starting with the closest time to epoch, a collision is recorded if the dif-

ference in the positions of both objects is smaller than the radius of the hard-body sphere. That is, if $\mathbf{r_i}$ and $\mathbf{r_j}$ are the positions of the samples in Cartesian coordinates generated from the primary spacecraft and secondary object respectively, at each time step, a collision is recorded if $||\mathbf{r_i} - \mathbf{r_j}|| \leq R_a$.The instantaneous probability of collision then becomes the number of recorded collisions at each time step divided by the number of samples used in the Monte Carlo simulation; that is

$$P_{C,inst} = \frac{n_{collision}}{n},$$

where $n_{collision}$ is the number of particles or samples that collided. Although the instantaneous probability of collision is an accurate measure of collision, it does not analyze the probability over the entire time span. For an accurate measure of the cumulative probability, $P_{C,inst}$ must be integrated over the span of the encounter. However, this will provide a misleading result due to the nature of the instantaneous collision probability counting similar collisions multiple times. Therefore, a check must be implemented to remove samples from the cloud of samples as they collide so that they cannot be recounted in future time steps. This will generate a unique instantaneous collision probability $P_{C,unique}$. An accurate measure of the collision probability over the span can now be found as (Burton *et al.* (2018))

$$P_{C,cum} = \int_{t_2}^{t_1} P_{C,unique} dt.$$

It is important to note that $P_{C,cum}$ must always be at least the value of $P_{C,inst}$. Figure 2.6 shows the relation between the three probabilities of collision explained using the data from Case 1.

Figure 2.6 illustrates the growth in the cumulative collision probability over the duration of the encounter with large increases when the instantaneous collision probability peaks. It is difficult, however, to see the change of the unique collision probability in this plot. Figure 2.7 illustrates the unique collision probability of the span of the encounter.

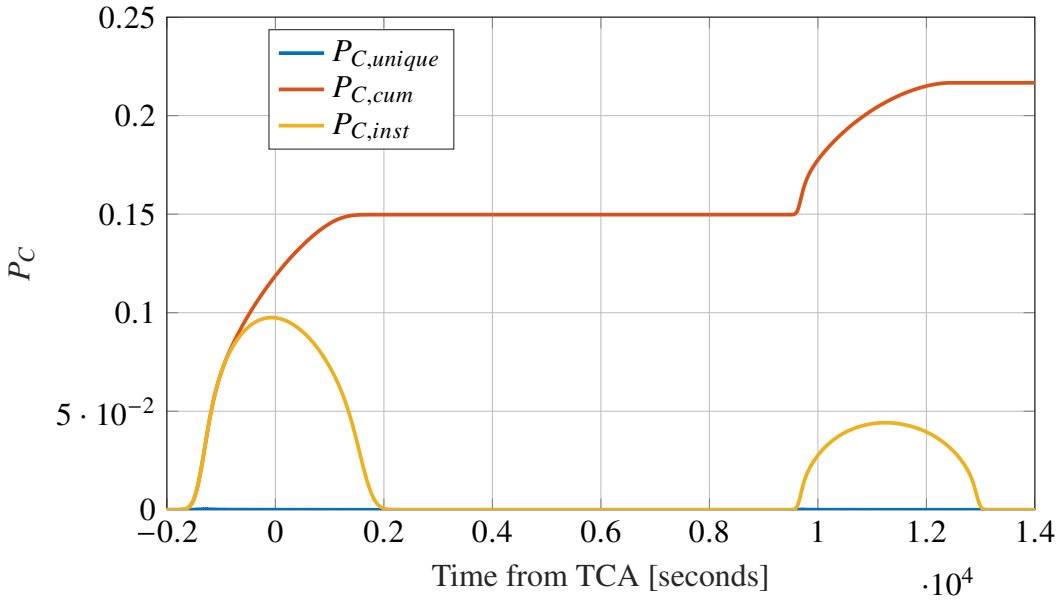

Figure 2.6. Relation of the three probabilities using Case 1

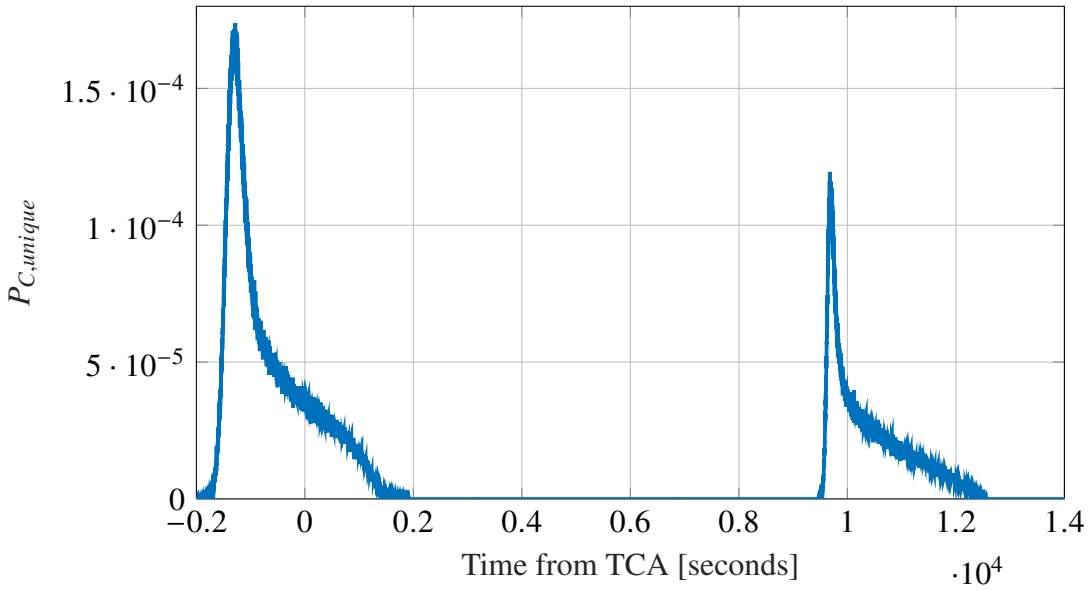

Figure 2.7. Unique probability of collision for Case 1

Figure 2.7 brings to light that the unique collision probability has a relatively unnoticeable change over the span of the encounter when compared to the instantaneous calculation. The peaks for the unique probability of collision occur during the same times as

Table 2.2. Comparison of the Keplerian Monte Carlo to Alfano's results

	Alfano's $P_{C,cum}$ Results [1×10^9]	**Keplerian MC $P_{C,cum}$ [1×10^7]**	**Error [%]**
Case 1	0.2174671	0.2167888	0.3119
Case 2	0.0157366	0.0155358	1.2761
Case 3	0.1008464	0.0996768	1.1598
Case 4	0.0730895	0.0736101	0.7122
Case 5	0.0444989	0.0444666	0.0726
Case 6	0.0043005	0.0043201	0.4558

the instanteous and cumulative collision probabilities, which is to be expected. Figure 2.7 makes it apparent that the cumulative collision probability is sum of the unique probability, even if it is difficult to visualize in Figure 2.6.

2.4.1. Numerical Implementation. The three cases of greatest value are Cases 1, 2, and 3, because they lie on such similar trajectories, and the largest difference between them is their respective relative velocities. As shown in Table 2.2, the results for each case are compared to Alfano's results of a Monte Carlo simulation with 1×10^9 samples. It is apparent that the data produced from the Keplerian Monte Carlo method with 1×10^7 samples is within 1.3% accuracy of the 1×10^9 results (Alfano (2009)). Therefore, the assumption of utilizing only 1×10^7 samples is sufficient for the scope of this analysis. It is an important note that for the linear cases 3, 5, and 6 the total computation time for a Keplerian Monte Carlo simulation with 1×10^7 samples took between 2 and 4 hours. Alternatively, the remaining nonlinear cases using the same number of samples required 16 to 20 hours to complete the process. A thorough analysis of each case is presented in the following section to examine the ability of the Keplerian Monte Carlo simulations to accurately describe the collision probability for specific cases.

2.4.1.1. Case 1. Case 1 involves nonlinear relative motion for two geosynchronous (GEO) satellites, where the nominal miss distance, x_e, is less than the combined object radius ($R_a = 15$ [m]). The Monte Carlo results in this work only differ by 0.3% from Alfano's proposed results, and this case required 16 and a half hours to process. Case 1 has been illustrated in the context of the aforementioned method, so there is no need to examine it further. However, the cumulative probability grows throughout time, mostly during two peaks, the largest occurring around TCA. If the time span of forward and backward propagation is expanded further, the cumulative probability continues to grow with various peaks. This is due to future possible encounter regions and should not be confused with the one of interest at TCA.

2.4.1.2. Case 2. This case also involves nonlinear relative motion for two GEO satellites and is identical in trajectory and covariance, but has a smaller combined object radius ($R_a = 4$ [m]). This case is interesting because at TCA, the nominal miss distance should exceed the hard-body radius. There is just over a 1% difference between the results from the Keplerian propagation of the Monte Carlo method when compared to the 1×10^9 results that Alfano proposes. This case with 1×10^7 samples required a run time of just over 16 hours. The probabilities over the span of the encounter can be seen in Figure 2.8.

Figure 2.8 illustrates that there is a spike in the cumulative probability at TCA, which is to be expected, but there is an additional spike about $11,000$ seconds later. This occurs because the primary object has "wandered " back into the covariance ellipsoid due to the highly nonlinear relative motion. This additional spike justifies the duration of the half orbit time span to encompassing the entire encounter region.

2.4.1.3. Case 3. This case involves linear relative motion for two geosynchronous orbits, where the nominal miss distance at TCA is less than the combined object radius ($R_a = 15$ [m]), meaning that there should be an imminent collision. Note that this is the same hard-body radius as the first test case, making the first and third cases ideal for testing and comparing methods. There is a surprisingly large discrepancy of 1.2% between this

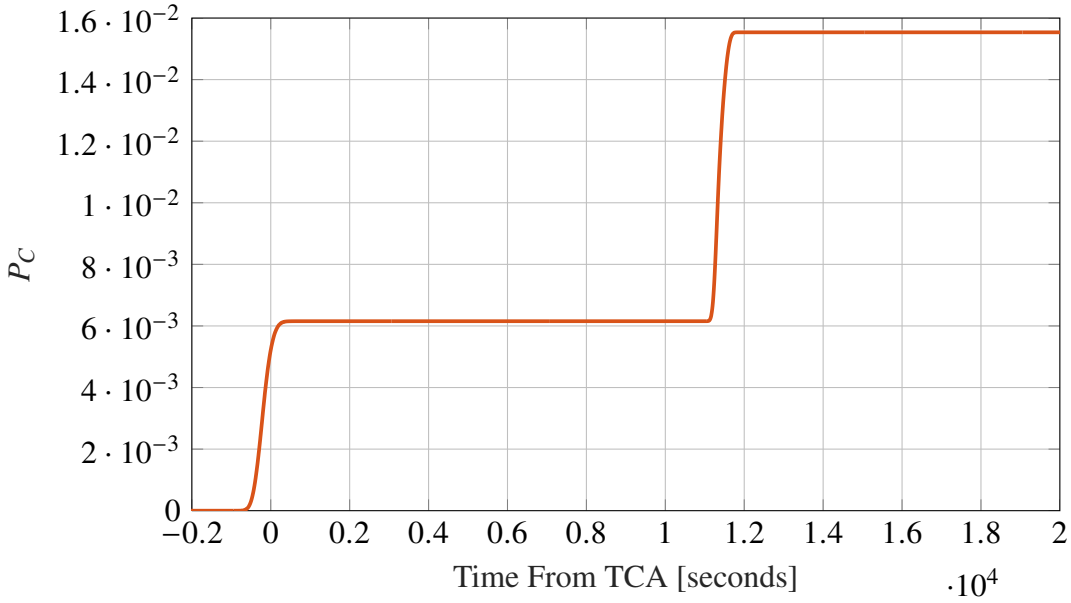

Figure 2.8. Cumulative probability of collision for Case 2 using Monte Carlo simulations [1×10^7 samples]

Monte Carlo and Alfano's published results, which could simply come from the relative velocity of this case being 16.6 [m/s] when all the other cases are less than 1 [m/s]. This could also be a source of error from numerical integration accuracy during the propagation steps or from the lack of sampling. If given enough samples, this Keplerian Monte Carlo method may converge to the same results. This case was the most efficient as it only took 2 hours to produce results.

Figure 2.9 illustrates the probabilities computed for Case 3. As expected for a linear encounter, there is only one spike at TCA, and the slope of the cumulative probability is very near zero at both ends of the time span.

2.4.1.4. Case 4. This case involves nonlinear relative motion for two satellites in geosynchronous orbits, where the nominal miss distance is greater than the combined object radius (R_a = 15 [m]). There is less than a 1% difference between the published results and the produced results in this work. This case required the most time out of all the runs with 22 hours.

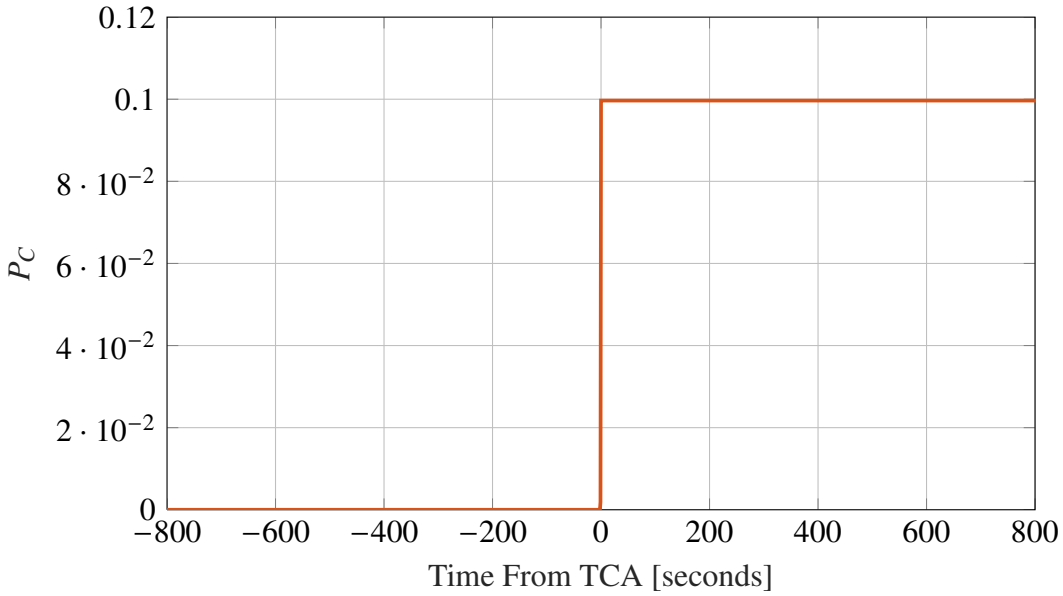

Figure 2.9. Cumulative probability of collision for Case 3 using Monte Carlo simulations [1×10^7 samples]

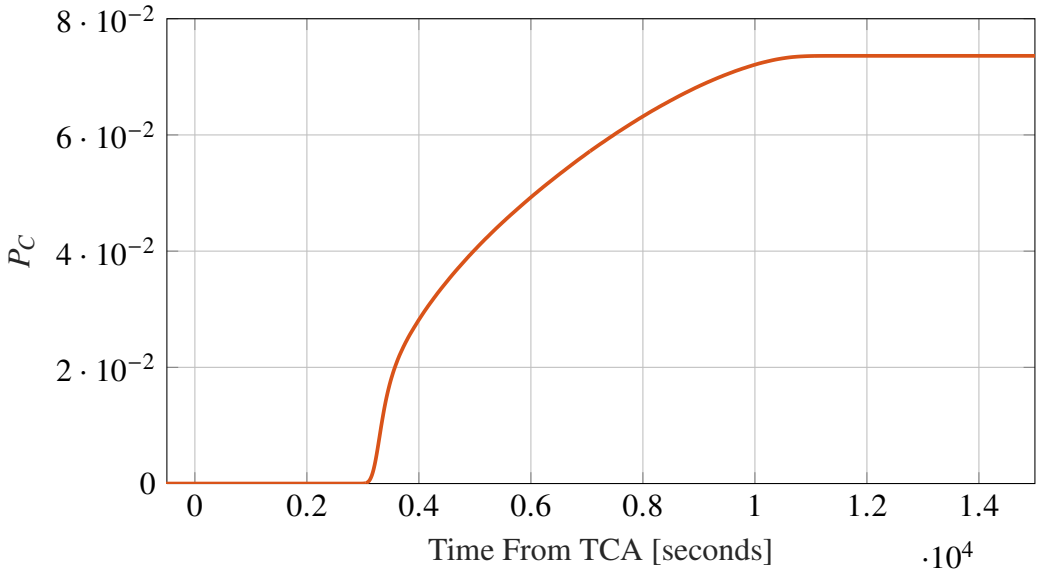

Figure 2.10. Cumulative probability of collision for Case 4 using Monte Carlo simulations [1×10^7 samples]

Figure 2.10 illustrates a case where the spike in collision probability is not near TCA. This is due to the particular combination of relative motion and covariance shape. Later, it will be seen that this can greatly affect some of the analytical methods.

2.4.1.5. Case 5. This case involves two low Earth orbiting (LEO) satellites, where the nominal miss distance at TCA is less than the combined object radius ($R_a = 10$ [m]). This is another interesting case because the entire hard-body object is essentially engulfed within the combined covariance ellipsoid; with the other cases, the object is only partially or barely inside the ellipsoid. This will have an interesting effect on the analytical methods in later sections. The Keplerian Monte Carlo results differ by less than 0.01% for this case as seen in Table 2.2.

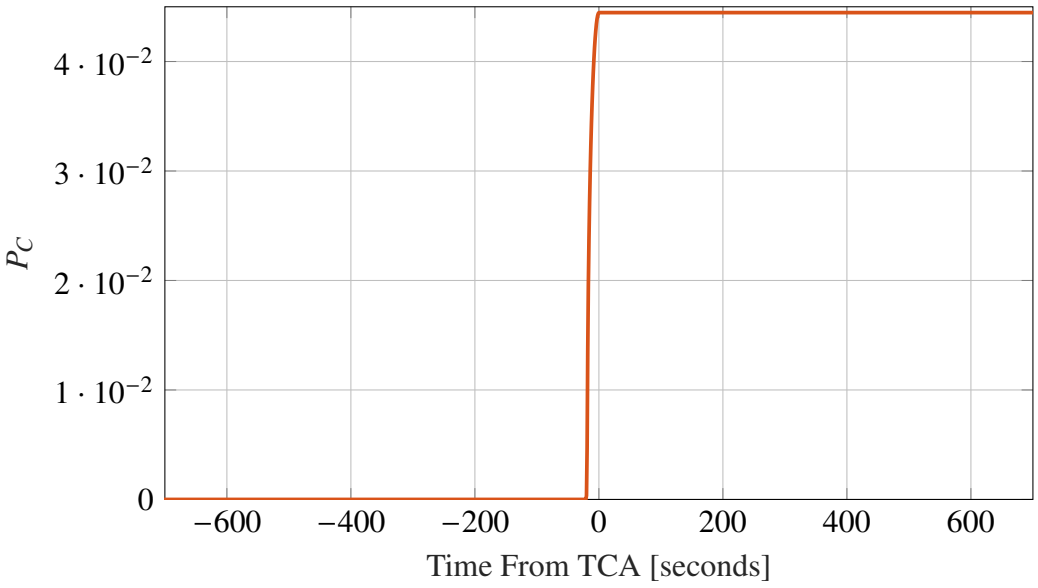

Figure 2.11. Cumulative probability of collision for Case 5 using Monte Carlo simulations [1×10^7 samples]

Figure 2.11 illustrates that this case is in fact following linear relative motion at TCA, because the slope in the cumulative collision probability is essentially zero at both ends of the time span. Another interesting aspect is that this linear case does not have as sharp of a peak at TCA as Case 3; it is seemingly more gradual of an incline. This could simply be due to the difference in scaling, as Case 3 is examined over a longer time span.

2.4.1.6. Case 6. The final case considered is another linear case in LEO, where the nominal miss distance at TCA is less than the combined object radius ($R_a = 10$ [m]). This case examines the extremity of having a relative velocity that is essentially linear, but would

be better examined as nonlinear. The relative velocity is low enough that the cylinder may begin to curve throughout the encounter region, transforming it to a nonlinear case. The probability of collision result for this case differs from Alfano's published result by only 0.5%.

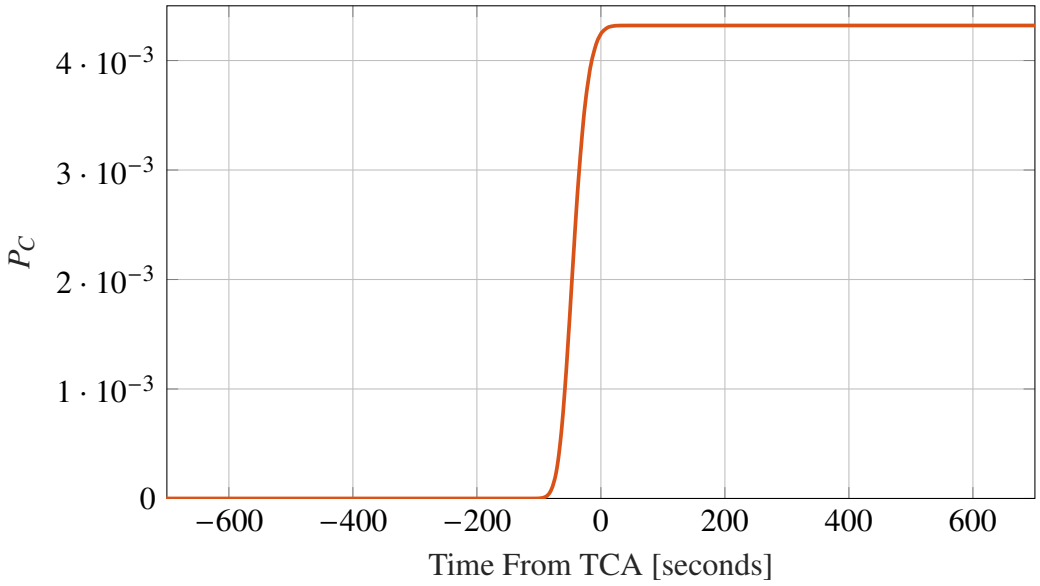

Figure 2.12. Cumulative probability of collision for Case 6 using Monte Carlo simulations [1×10^7 samples]

Figure 2.12 is similar to the results of Case 5, which is to be expected as they are both linear relative motion in LEO. There is a gradual increase in cumulative probability around TCA, and the slope at both ends of the time is once again essentially zero.

For an actual implementation of computing the probability of collision for a spacecraft, one would need to increase the number of samples by at least one factor of 10 (1×10^8 samples), which would exponentially increase the computational time for this Monte Carlo simulation. Therefore, other methods must be investigated to approximate the probability of collision without being as computationally demanding.

3. ANALYTICAL METHODS

3.1. LINEAR METHODS

To improve computational efficiency, one may turn to an analytical method to approximate the probability of a spacecraft colliding with a secondary object. An analytical method utilizes the relative position, relative velocity, and combined covariance of both objects at TCA in the encounter frame defined in Section 2. A simple linear extension to the analytical methods will approximate a solution under the assumption that the relative velocity will sweep out a straight, right cylinder through the encounter region, meaning that the method will only approximate a single solution at the point of closest approach. The linear methods assume rectilinear relative motion at the time of closest approach and assume that the relative velocity is large enough that the path of the primary object through the encounter region is a straight line.

The objective of this next section is to evaluate the linear methods' ability to approximate the cumulative probability of collision using an analytical process. The linear methods investigated in this work come from the works of Patera (Patera (2005)) and Alfano (Alfano (2005)). These methods operate by converting the position, velocity, and covariances of each object at TCA into the relative encounter frame defined earlier. Utilizing this information, each method analytically approximates the quantity of the hard body sphere within the combined ellipsoid. This process is only interested in the projection of these three-dimensional surfaces onto the two-dimensional $(\hat{x},\hat{z})$-plane.

3.1.1. Patera's Method. Once a spacecraft is identified to have a collision risk with an object, both objects are propagated to a time near the closest approach, where their relative motion is assumed linear. Once propagated, the Cartesian states and covariances of each object are converted into the encounter frame and are then used to determine the

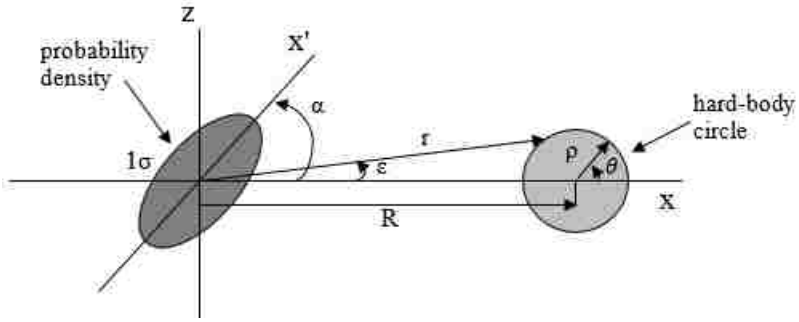

Figure 3.1. Projected hard-body and covariance ellipsoid on the encounter plane (modified from Patera (2005))

distance of minimum separation. The combined position error covariance ellipsoid and hard-body sphere are generated, then centered about the secondary object and primary spacecraft, respectively. It is important to note that the center of the secondary object is treated as the origin of the encounter coordinate system. The ellipsoid and hard-body sphere are projected onto the ($\hat{x}$,$\hat{z}$) encounter plane as an ellipse and circle, respectively, as illustrated in Figure 3.1. The collision probability is then the integral of the probability density defining the relative position over the hard-body area, as presented in Equation (2.3). Patera, however uses an interesting technique of integrating over the perimeter of the hard-body instead, resulting in

$$P = \frac{1}{2\pi} \oint_{perimeter} \left[1 - \exp\left(\frac{-r^2}{2\sigma^2} \right) \right] d\epsilon, \tag{3.1}$$

where P is the probability of collision, r is the distance to the hard-body perimeter from the center of the secondary object, and ϵ is the contour integration parameter. The axis having the largest position error standard deviation, σ_x, makes an angle α with the $\hat{x}$-axis. The largest standard deviation is also used for σ in Equation (3.1) (Patera (2001)). Figure 3.1 also shows the path along the perimeter that the integration will take. Equation (3.1) can be converted to a definite integral by changing to polar coordinates.

Let the polar coordinate system be centered at (R, 0), where R is the minimum separation distance, x_e, expressed in polar coordinates. For the remainder of this work, it will be referred to as just x_e. Any points on the hard-body perimeter are then defined as

$$x = x_e + \rho\cos(\theta) \tag{3.2}$$
$$z = \rho\sin(\theta),$$

where ρ is the radial position and θ is the angular position of a point on the perimeter. A spherical assumption is used, such that the hard-body radius, R_a, is used for ρ. Once all the input data is defined within the ($\hat{x}'$, $\hat{z}'$) encounter plane defined earlier, a scale change is completed to transform the perimeter points to a symmetrized coordinate frame, shown in Figure 3.2 and given by

$$\begin{bmatrix} x' \\ z' \end{bmatrix} = \begin{bmatrix} 1 & 0 \\ 0 & f \end{bmatrix} \begin{bmatrix} x \\ z \end{bmatrix},$$

where f is the ratio of the standard deviation in the x-axis to the standard deviation of the position in the z axis, i.e.

$$f = \frac{\sigma'_x}{\sigma'_z}.$$

This scale change reshapes the combined covariance ellipse into a circle and the hard-body circle into an ellipse. To simplify the integration, the contour integration parameter ϵ in Equation (3.1) is related to θ by

$$\tan(\epsilon) = \frac{fR_a\cos(\alpha)\sin(\theta) - x_e f\sin(\alpha) - fR_a\sin(\alpha)\cos(\theta)}{x_e\cos(\alpha) + R_a\cos(\alpha)\cos(\theta) + R_a\sin(\alpha)\sin(\theta)},$$

or

$$\tan(\epsilon) = \frac{fR_a\sin(\theta-\alpha) - x_e f\sin(\alpha)}{x_e\cos(\alpha) + R_a\cos(\theta-\alpha)}. \tag{3.3}$$

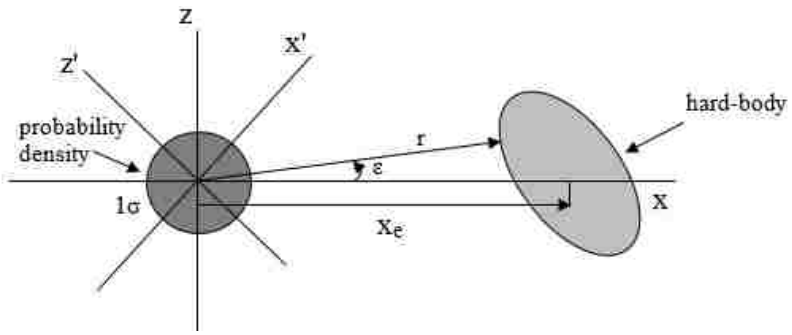

Figure 3.2. Projected hard-body and covariance ellipsoid on the symmetrized encounter plane (modified from Patera (2005))

The derivative of Equation (3.3) with respect to ϵ is

$$\frac{d\epsilon}{d\theta} = \cos^2(\epsilon)\frac{d[\tan(\epsilon)]}{d\theta} = \frac{fR_a^2 + fR_a x_e \cos(\theta) + x_e f R_a'}{r^2}, \tag{3.4}$$

where

$$\begin{aligned} r^2 =& \sqrt{(x')^2 + (y')^2} \\ =& \Big[x_e + R_a\cos(\theta)\Big]^2\Big[\cos^2(\alpha) + f^2\sin^2(\alpha)\Big] + R_a^2\sin^2(\theta)\Big[\sin^2(\alpha) + f^2\cos^2(\alpha)\Big] \\ &+ 2R_a(1-f^2)\cos(\alpha)\sin(\alpha)\sin(\theta)\Big[x_e + R_a\cos(\theta)\Big], \end{aligned}$$

and

$$R_a' = \frac{dR_a}{d\theta}.$$

Leveraging Equation (3.4), Equation (3.1) can be transformed from a contour integral to a definite integral, given by

$$P = \frac{1}{2\pi}\int_0^{2\pi}\left[\frac{fR_a^2 + x_e f R_a\cos(\theta) + x_e f R_a'\sin(\theta)}{r^2}\right]\left[1 - \exp\left(\frac{-r^2}{2\sigma^2}\right)\right]d\theta. \tag{3.5}$$

Equation (3.5) provides an accurate method for computing collision probability for most applications. This will been seen later with a comparison of all of the methods for each of the six cases. It is important to note that, for spherical hard-bodies, R_a is a constant; therefore, the R_a' term vanishes. If, however, one chooses to examine the effects of different shapes defining the hard-body, then R_a' would be retained (Patera (2005)). For implementation, one can transform the integral in Equation (3.5) to a finite sum, from zero to $\frac{2\theta}{n}$, where n is a user set number of desired steps. The number of steps to achieve accurate results from Equation (3.5) may differ between cases; this will be examined in later sections.

3.1.2. Alfano's Method. Alfano's method differs from Patera's by utilizing a summation to approximate the one-dimensional integral rather than integrating over the perimeter or area of the hard-body (Alfano (2005)). Similar to the other methods, at the point of closest approach, the combined covariance ellipsoid and hard-body are projected onto the plane perpendicular to the relative velocity, otherwise known as the encounter plane. The collision probability is then calculated by the amount of area of the hard-body within the projected two-dimensional covariance ellipse. The result for the probability of collision is given by the double integral shown in Equation (2.3), which can be reduced to a single integral by using an error function. Alfano's method utilizes Simpson's one-third rule to approximate this single integral.

This method requires the inputs of σ_x' and σ_z', which should be the standard deviations of the major and minor axes of the projected, combined covariance ellipse, respectively. Additional required parameters are the position of the primary spacecraft relative to the secondary object on the projected plane, x_p and z_p, and the radius of the combined object, R_a. The position of the primary relative to the secondary can be expressed as

$$\begin{aligned} x_p &= x_e \cos(\alpha) \\ z_p &= -x_e \sin(\alpha). \end{aligned} \tag{3.6}$$

The angle α is the same angle used to rotate the ($\hat{x}$,$\hat{z}$) encounter plane to the ($\hat{x}'$,$\hat{z}'$) plane, where each axis is directed along the major and minor axes of the combined covariance ellipse. The two-dimensional probability equation for the primary spacecraft relative to the secondary is given by

$$P = \frac{1}{2\pi\sigma'_x\sigma'_z}\int_{-\rho}^{\rho}\int_{-\sqrt{\rho^2-x^2}}^{\sqrt{\rho^2-x^2}} \exp\left[-\frac{1}{2}\left[\left(\frac{x+x_p}{\sigma'_x}\right)^2 + \left(\frac{z+z_p}{\sigma'_z}\right)^2\right]\right] dz dx. \tag{3.7}$$

Throughout in this section, ρ represents the hard-body radius, R_a. Equation (3.7) can be reduced to a single integral through the use of the error function as

$$P = \frac{1}{\sqrt{8\pi}\sigma'_x}\int_{-\rho}^{\rho}\left[\operatorname{erf}\left(\frac{z_p+\sqrt{\rho^2-x^2}}{\sqrt{2}\sigma'_z}\right) + \operatorname{erf}\left(\frac{-z_p+\sqrt{\rho^2-x^2}}{\sqrt{2}\sigma'_z}\right)\right] \times \exp\left(\frac{-(x+x_p)^2}{2(\sigma'_x)^2}\right) dx, \tag{3.8}$$

where erf in Equation (3.8) refers to the error function and is usually readily available in mathematical software packages. Alfano simplifies this one-dimensional error function integral into an n-series expression via the change of variables (Alfano (2005))

$$x = \frac{\rho(2i-n)}{n}, \tag{3.9}$$

and

$$dx = \frac{2\rho}{n}. \tag{3.10}$$

Substituting Equations (3.9) and (3.10) into Equation (3.8), the probability of collision becomes

$$P = \frac{2\rho}{\sqrt{8\pi}\sigma'_x n}\sum_{i=0}^{n}\left[\left[\operatorname{erf}\left(\frac{z_p + \frac{2\rho}{n}\sqrt{(n-i)i}}{\sqrt{2}\sigma'_z}\right) + \operatorname{erf}\left(\frac{-z_p + \frac{2\rho}{n}\sqrt{(n-i)i}}{\sqrt{2}\sigma'_z}\right)\right] \times \exp\left(\frac{-\left(\frac{\rho(2i-n)}{n} + x_p\right)^2}{2(\sigma'_x)^2}\right)\right]. \tag{3.11}$$

If desired, Equation (3.11) can be simplified further to admit a computationally lighter implementation by using Simpson's one-third rule and breaking the series into m-even and m-odd components (Alfano (2005)), where a sufficient number for the m terms is given by

$$m = \operatorname{int}\left(\frac{5R_a}{\min\left(\sigma'_x, \sigma'_z, \sqrt{\left(x_p\right)^2 + \left(z_p\right)^2}\right)}\right).$$

Otherwise, Equation (3.11) requires the number of steps, n, to be specified; for the scope of this work, n is typically taken to be the same number of steps that is used in calculating collision probability with Patera's method. Otherwise, 360 steps will be sufficient for most cases; this will be explained further when discussing implementation of the cases.

3.1.3. Numerical Implementation. Each of the six cases described in Section 2.3 is processed using both of the presented linear analytical methods; the results of the cases are summarized in Table 3.1. There is no need to examine the plots of these results, as every case yields a zero slope at all time steps and a vertical peak to the solution at TCA. This is due to the nature of the analytic linear methods; these methods only examine the collision probability generated at the point of closest approach. All of the plots will have similar trends to that of Case 3 shown in Figure 2.9, which was obtained with the Monte Carlo approach.

Table 3.1. Comparison of linear and Monte Carlo results

	Patera's Method $P_{C,cum}$	**Alfano's Method** $P_{C,cum}$	**MC** $P_{C,cum}$ $[\mathbf{1 \times 10^7}]$
Case 1	0.146791	0.146747	0.216789
Case 2	0.006248	0.006222	0.015536
Case 3	0.100381	0.100351	0.099677
Case 4	0.050669	0.049323	0.073610
Case 5	0.044506	0.044493	0.044467
Case 6	0.004346	0.004334	0.004320

For most of the cases considered, a value of $n = 100$ proves to be sufficient; however, Case 5 produces inaccurate results with this value. This is because the hard-body sphere is completely within the combined covariance ellipsoid. The value of n must be increased to ensure that the entire hard-body sphere is considered; the value of n in this case should be 360. For simplicity, all the results presented in Table 3.1 are computed with $n = 360$. Since these are an analytical methods, the increase in the value n does not significantly contribute to a decrease in computational efficiency. One interesting observation is that Case 6 is still approximated within 1% error with respect to the Monte Carlo results, even though this case was just barely defined as linear. These results illustrate the accuracy of the analytic solutions when approximating the probability of collision for linear relative motion. When one tries to compute the collision probability of a nonlinear relative motion case with a linear analytic method, however, the approximation will always underestimate the true probability. This trend can be seen in all of the nonlinear cases attempted, such as Cases 1, 2, and 4. This is because the methods are only approximating the collision probability of a single point, and cases with highly nonlinear relative motion tend to stay within the encounter region for much longer than several seconds, invalidating the use of

the linear analytical methods with nonlinear cases. To consider the entire time span, an analytical method must be used at varying time steps with varying covariances, positions, and velocities.

3.2. NONLINEAR METHODS

The numerical implementation of the linear methods demonstrates that the linear analytical solutions can have difficulties approximating cases that involve low relative velocity objects. This is due to the assumption of a static combined covariance over the encounter, as well as the decoupling of the parameters within the $\hat{y}$-direction. These assumptions are sufficient for high relative velocity objects since the encounter region is traversed in such minuscule time spans (usually fractions of a second to a couple of seconds), so the relative motion can be seen as linear, and the conjunction only needs to be examined at a single time step. Low relative velocity cases, however, may not be linear through this encounter region because it could take up to hundreds or even thousands of seconds to traverse the conjunction. This means that the velocity changes through time, similarly, the covariance shell changes through time.

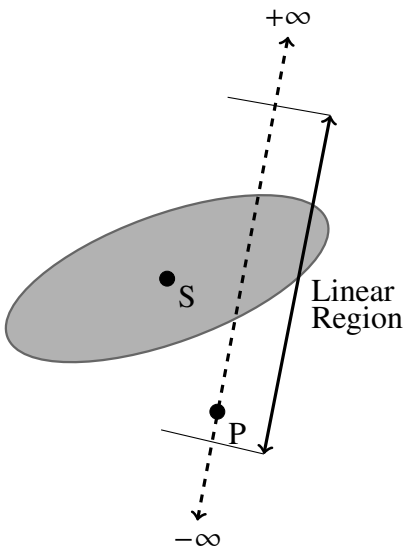

Figure 3.3. Linear trajectory over the encounter region (modified from (Patera (2003)))

Figure 3.3 illustrates the path of a linear trajectory for relative motion across the encounter frame. In theory, one should be able to pick an arbitrary point at some time step within the linear region and calculate essentially the same probability as would be computed from a linear method at TCA. Therefore, one does not necessarily have to propagate the objects to TCA for a linear case, only to the beginning of the linear region. This would, however, add complexities to the propagator, so for simplicity sake, one should simply propagate the objects to the point of closest approach to utilize the methods. Figure 3.4, on the other hand, illustrates the case where low relative velocity drastically decreases the linear region to a fraction of the combined covariance ellipsoid.

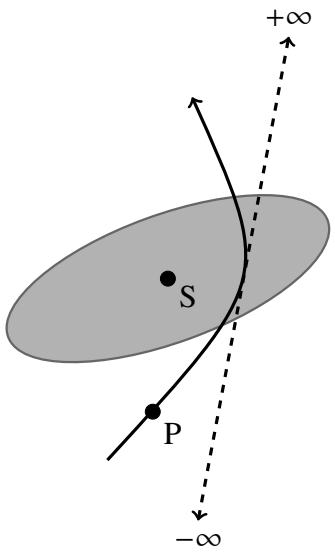

Figure 3.4. Nonlinear trajectory over the encounter region (modified from Patera (2003))

Revisiting the linear cases, i.e. Cases 3, 5, and 6, it is possible to decouple any probability that is generated from the parameters in the $\hat{y}$-direction. Forming a straight cylinder extending from $-\infty$ to $+\infty$, integration along the $\hat{y}$-direction yields a probability of one. In these low relative velocity cases, however, the cylinder formed at TCA will have finite extent that does not span the entire encounter region. To approach this problem, one needs to calculate the time span that the two objects occupy the encounter region, i.e. when the primary spacecraft is within the combined covariance ellipsoid. Then, at

each time step, a right cylinder with the length along the direction of the relative velocity vector, $\mathbf{v}_{ps}$, is formed. Each cylinder has a corresponding collision probability based on the three-dimensional properties. The cumulative probability for the encounter region is then determined as the sum of all of the individual probabilities. This method is referred to as the adjoining cylinders method (Alfano (2008)).

3.2.1. Adjoining Cylinders. The first step in the adjoining cylinders method, and any other, is to begin with the position, velocity, and covariance in the inertial frame at TCA. This data is then propagated forward and backward in time until a specified limit is reached. To cover the entire encounter span, one quarter of an orbit in each direction of time is usually sufficient. At each time step, a right cylinder is formed, the length of which depends on the relative velocity at TCA, and the radius of the cylinder is the same as the radius of the hard-body sphere, because the hard-body sphere is the object sweeping out the cylinder at each time step. For an accuracy check on defining the size of the cylinders, a method of defining a linearity requirement is presented in (Alfano (2008)). Over each cylinder, the relative motion is assumed to be linear and the covariance is assumed to be constant, this is only true if all the cylinders are sufficiently small. The time step containing the relative velocity at TCA defines the length of the cylinder; therefore, smaller time steps define proportionally smaller right cylinders. This time step is case dependent. At each time step, the objects, as well as their positions and covariances, are transformed into an encounter frame that normalizes the combined covariance. In this frame, each cylinder section has a two-dimensional probability, P_{2d}, and a one-dimensional probability, P_{1d}. The product of these two probabilities yields the sectional probability of collision for the individual cylinder. The sum of all of the sectional probabilities yields the cumulative probability of collision for the encounter.

3.2.1.1. Normalized encounter frame. In the inertial frame, the covariance of the primary spacecraft is summed with the covariance of the secondary object,such that

$$\mathbf{C} = \mathbf{C}_p + \mathbf{C}_s.$$

A transformation, $\mathbf{T}_i^p$, is then conducted to align a new coordinate frame to be along the axes of this three-dimensional combined covariance ellipsoid. Consider the spectral decomposition of $\mathbf{C}$, given by

$$\mathbf{C} = \mathbf{V}\boldsymbol{\lambda}\mathbf{V}^T,$$

where $\mathbf{V}$ is a square matrix whose i^{th} column is the i^{th} eigenvector of $\mathbf{C}$ and $\boldsymbol{\lambda}$ is a square diagonal matrix whose i^{th} element is the i^{th} eigenvalue of $\mathbf{C}$. The transformation matrix, $\mathbf{T}_i^p$, is formed as the transpose of the eigenvector matrix, such that

$$\mathbf{T}_i^p = \mathbf{V}^T.$$

All of the objects' positions, velocities, and covariances must then be converted into a scaled system defined by the scaling matrix $\mathbf{S}$, where

$$\mathbf{S} = \boldsymbol{\lambda}^{-1/2}.$$

This scaling transformation normalizes the covariance and scales all other data values respectively. To analyze the probability of collision between the objects, all positions, velocities, and covariances must be in one relative frame, so another transformation must be completed to scale these normalized components into the previously defined relative encounter frame. Simply put, the normalized components are transformed back into the inertial frame using the transpose of the transformation matrix $\mathbf{T}_i^p$, then the directional cosine matrix defined in Equation (2.8) in Section 2 is used to rotate the data into the relative

encounter frame. The transformation from inertial to a scaled inertial using the eigenvalues becomes

$$\mathbf{M} = \mathbf{T}_p^i \mathbf{S} \mathbf{T}_i^p \tag{3.12}$$

$$\begin{Bmatrix} x_{scale} \\ y_{scale} \\ z_{scale} \end{Bmatrix} = \mathbf{M} \begin{Bmatrix} x \\ y \\ z \end{Bmatrix} \tag{3.13}$$

$$\mathbf{C}_{scale} = \mathbf{M}\mathbf{C}\mathbf{M}^T,$$

resulting in,

$$\mathbf{C}_{scale} = \begin{bmatrix} \sigma(1) & 0 & 0 \\ 0 & \sigma(1) & 0 \\ 0 & 0 & \sigma(1) \end{bmatrix} = \mathbf{I}_{3\times 3}, \tag{3.14}$$

where $\sigma(1) = 1$.

The same transformation matrices previously used to rotate the system into the relative encounter frame can now be applied. Without the normalized scale change, if the combined covariance ellipsoid was in the encounter frame, then the principle directions would not be aligned with the axes; in some cases they could be essentially aligned, but not exactly aligned. This develops complexities when defining the encounter region in terms of relative positions and velocities. In the scale encounter frame, the combined covariance ellipsoid will become a sphere, and due to the nature of a unit sphere, when the user aligns the system to be in the relative encounter frame, the principle axes no longer matter because a sphere does not have principle axes. An important note is that, due to the covariance, position, and velocities being converted by a scale change, the hard-body sphere must also undergo a scale change. Doing so transforms the hard-body sphere into a hard-body

ellipsoid, where the semi-axes of the ellipsoid are

$$\mathbf{R}_{Ellipse} = R_a\mathbf{S} = \begin{bmatrix} \rho_x & 0 & 0 \\ 0 & \rho_y & 0 \\ 0 & 0 & \rho_z \end{bmatrix}.$$

With the scaled positions and scaled velocities of each object in terms, once again, of the Cartesian inertial frame, rotate the data to the normalized encounter frame by

$$\begin{Bmatrix} x_{norm} \\ y_{norm} \\ z_{norm} \end{Bmatrix} = \mathbf{U}_m^e\mathbf{U}_i^m \begin{Bmatrix} x_{scale} \\ y_{scale} \\ z_{scale}. \end{Bmatrix}$$

The transformation matrices $\mathbf{U}_i^m$ and $\mathbf{U}_m^e$ can be found as Equations (2.6) and (2.8) in the encounter frame section of Section 2.

Due to the nature of the combined covariance sphere, there is no need for an additional rotation to the principle axes because they become arbitrary. Meaning that a means to identify the time span of the encounter region is now possible. Starting from the time closest to epoch, the positions, velocities, and covariance at each time step are converted into the normalized encounter frame, and is compared to the relative position vector along the $\hat{y}$-direction, i.e. the y-component of the relative position vector in the normalized encounter frame ($\mathbf{r}_{ps,y} = \mathbf{r}_{p,y} - \mathbf{r}_{s,y}$), to the standard deviation in the $\hat{y}$-direction, $\sigma_{y,norm}$, or $\sigma(1)$ in the normalized encounter frame. This process is not possible if the encounter coordinate frame is not aligned with the principle axes of the combined covariance ellipsoid, but because this new scale change normalizes the ellipsoid to a sphere, this process becomes possible. In this frame, all the standard deviations are 1, as shown in Equation (3.14). If the relative position vector is larger than the standard deviation in the $\hat{y}$-direction at any time step, then that data is omitted from further processing. This process is continued until the furthest time step from epoch has been omitted. If the final time step is not omitted, then

the overall time span of propagating forward and backward should be expanded. There should be some times at the beginning and at the end of the time span that are omitted to verify that all of the encounter region is accounted for. The cylinders are formed about the time steps that remain, then the one-dimensional and two-dimensional probabilities are computed for each cylinder at its corresponding time step.

3.2.1.2. One dimensional probability. Each time step acts as the center of a straight cylinder, the ends of the cylinder are defined as R_i and R_f, which are based on the relative velocity along the $\hat{y}$-direction in the normalized encounter frame at TCA and the time step between processed times. The relative velocity along the $\hat{y}$-direction should essentially be all the velocity because the $\hat{y}$-axis is defined as being along the relative velocity vector. The ends of the cylinder are given by

$$\begin{aligned} R_i &= r_{ps,y} - \delta R \\ R_f &= r_{ps,y} + \delta R, \end{aligned} \tag{3.15}$$

where

$$\delta R = v_{ps,y} \left(\frac{\Delta t}{2} \right),$$

$r_{ps,y}$ and $v_{ps,y}$ are the $\hat{y}$-components of the relative position and velocity in the normalized encounter frame, respectively, and Δt is the specified time step, which also defines the size of the cylinders.

Now that all the data is in the normalized encounter frame with a spherical covariance shell describing a symmetric probability density, the probability density along each axis can be decoupled from the other axes. Revisiting the cumulative collision probability integral from Equation (2.1), it follows that

$$P = \frac{1}{(2\pi)^{3/2}} \iiint_V \exp\left[\frac{-(x^2 + y^2 + z^2)}{2} \right] dxdydz. \tag{3.16}$$

The limits of integration for this three-dimensional integral are defined by the volume of the cylinder swept out by the sphere. It becomes convenient to transform Equation (3.16) into cylindrical coordinates with the $\hat{y}$-axis aligned with the axis of the cylinder. The cumulative collision probability is given by

$$P = \frac{1}{(2\pi)^{3/2}} \iiint_V \exp\left(\frac{-y^2}{2}\right) \exp\left(\frac{-r^2}{2}\right) r\,dr\,d\theta\,dy,$$

where r is the radial distance from the secondary to the primary, and θ is the angle between r and the $\hat{x}_{norm}$-axis. The integration along each time increment assumes that the probability, hard-body area, and relative velocity are constant for each time step. At each step, the integration can be performed, yielding

$$P = \left[\frac{1}{\sqrt{2\pi}} \int_{Ri}^{Rf} \exp\left(\frac{-y^2}{2}\right) dy\right] \frac{1}{2\pi} \oint_{perimeter} \left[1 - \exp\left(\frac{-r^2}{2}\right)\right] d\theta. \tag{3.17}$$

Now, the probability density defined in the direction along the relative velocity vector, $\hat{y}$-direction, is decoupled from the probability density described by the $(\hat{x}_{norm}, \hat{z}_{norm})$-encounter plane. There are a finite number of cylindrical volumes, each with an associated collision probability that is formed as the product of the two decoupled probabilities. If the relative velocity and the covariance are constant over the encounter, then the cylinders form a single cylinder extending from $-\infty$ to $+\infty$; in this case, the integration of the first bracketed term in Equation (3.17) is equal to one, and the cumulative collision probability from Equation (3.17) becomes

$$P_C = \frac{1}{2\pi} \oint_{perimeter} \left[1 - \exp\left(\frac{-r^2}{2}\right)\right] d\theta \tag{3.18}$$

Equation (3.18) is a version of Equation (3.5) used in the proof of Patera's method in Section 3.1.1, meaning that when given an infinite cylinder, the probability of collision along the relative velocity vector, or $\hat{y}$-direction, is one. Validating that the adjoining cylinders method can be applied to linear and nonlinear cases.

To simplify the computation of the probability along the relative velocity direction, apply the cumulative distribution function of a Gaussian distribution, $q(x)$, which states

$$\int_a^b q(x)dx = \frac{1}{2}\left[\text{erf}\left(\frac{b-m}{\sqrt{2P}}\right) - \text{erf}\left(\frac{a-m}{\sqrt{2P}}\right)\right], \tag{3.19}$$

where m and P are, respectively, the mean and covariance of the Gaussian distribution. Applying Equation (3.19) to the first bracketed term in Equation (3.17), noting that $a = R_i$, $b = R_f$, $m = 0$, and $P = 1$, it follows that

$$P_{1d} = \frac{1}{2}\left[\text{erf}\left(\frac{R_f}{\sqrt{2}}\right) - \text{erf}\left(\frac{R_i}{\sqrt{2}}\right)\right], \tag{3.20}$$

Thus providing a solution for the decoupled probability of collision along the axis defined by the relative velocity vector. The next step is to calculate the remaining two dimensional probability for each time step.

3.2.1.3. Two dimensional probability. After decoupling the probabilities, the two-dimensional probability density function is given by Equation (3.18), which can be simplified to Patera's linear method of Equation (3.5), or

$$P_C = \frac{1}{2\pi}\int_0^{2\pi}\left[\frac{fR_a^2 + x_e f R_a \cos(\theta) + x_e f R_a' \sin(\theta)}{r^2}\right]\left[1 - \exp\left(\frac{-r^2}{2\sigma^2}\right)\right]d\theta, \tag{3.21}$$

Due to the aligning of the relative encounter frame with the covariance ellipsoidal axes and symmetrizing to unity, f in Equation (3.21) does not appear because all the standard deviations are 1. This new rotation also converts the hard-body shape into an ellipse with magnitudes ρ_x and ρ_z defining the two-dimensional ellipse on the normalized encounter plane, located at (x_{norm}, z_{norm}). The center is the x and z components of the relative position vector in the normalized encounter frame. After much manipulation, a series can

be formed to represent the two-dimensional probability computation as (Alfano (2008))

$$P_{2d} = \frac{\rho_x \rho_z}{n} \sum_{i=1}^{n} \left[\left(1 + \frac{x_{norm}}{\rho_x} \cos\left(\frac{2i\pi}{n}\right) + \frac{z_{norm}}{\rho_z} \sin\left(\frac{2i\pi}{n}\right) \frac{1}{\alpha_i^2} \left(1 - \exp\left(\frac{\alpha_i^2}{-2}\right)\right)\right)\right], \tag{3.22}$$

where

$$\alpha_i^2 = \left(\rho_x \cos\left(\frac{2i\pi}{n}\right) + x_{norm}\right)^2 + \left(\rho_z \sin\left(\frac{2i\pi}{n}\right) + z_{norm}\right)^2.$$

It is important to note that this is a manipulation of Patera's method in the normalized encounter frame. The n in the summation of Equation (3.22) is the same $n = 360$ that is used when computing the series version of Patera's linear method from Equation (3.5). An alternative to this version of the two-dimensional probability of collision is to simply utilize the linear methods that have come before; in theory, the computed probability should come out essentially the same, and this will be investigated in the next section. The cumulative collision probability for the adjoining cylinders nonlinear method becomes

$$P_{C,cum} = \sum_{n=1}^{N} P_{1d} P_{2d},$$

where N is the number of cylinders that is generated by the defined step size.

3.2.2. Numerical Implementation. When implementing the adjoining cylinders method, it becomes imperative to incorporate enough of a time span to completely evaluate the encounter region; otherwise, the method will drastically underestimate the collision probability. It is also crucial not to overestimate the time span, because there will be potential "conjunctions" in the future, or at least the algorithms will see them as conjunctions. The collision probability computed at these times will be minuscule in comparison to those at TCA, but will still corrupt the results, by overestimating the true probability of collision. These other conjunctions can be seen in Figure 3.5, which shows that the encounter region of interest is sufficiently within the bounds of the one quarter orbit propagation, both

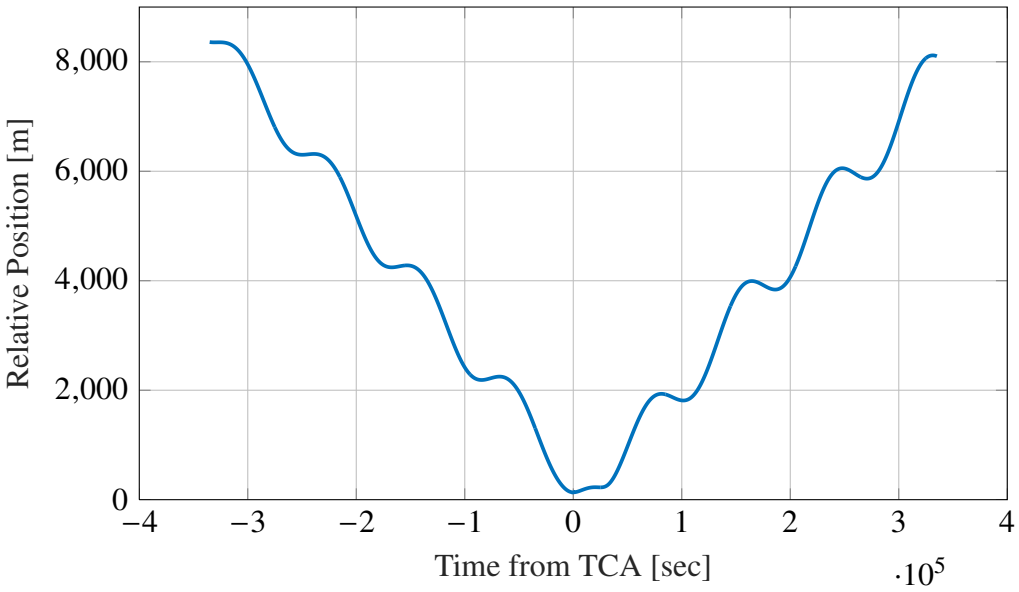

Figure 3.5. Relative distance between the primary spacecraft and the secondary object

forward and backward in time from TCA. Each valley in Figure 3.5 represents a possible encounter region, but the only one of interest is the most severe region, or the one that will perpetuate the largest probability of collision.

The results for all six cases are given in Table 3.2, it is clear in these results that all but one of the cases is sufficiently approximated. All of the cases tested utilized a time step of 0.5 seconds for the propagation both forward and backward to produce the cylinders.

Table 3.2. Comparison of nonlinear to Monte Carlo results

	Adj. Cylinders Patera's 2-d $P_{C,cum}$	**Adj. Cylinders Eq.** (3.22) $P_{C,cum}$	**MC** $P_{C,cum}$ $[\mathbf{1 \times 10^7}]$
Case 1	0.218586	0.218165	0.216789
Case 2	0.016397	0.016239	0.015536
Case 3	0.100380	0.100353	0.099677
Case 4	2.0633×10^{-5}	1.4552×10^{-5}	0.073610
Case 5	0.044399	0.044385	0.044467
Case 6	0.004232	0.004223	0.004320

An interesting outcome of Table 3.2 is that the results from using the adjoining cylinders with a two-dimensional probability calculated using Patera's linear method and the normalized two-dimensional method in Equation (3.22) only differ by 0.2%. Therefore, it is not critically important which method is chosen to calculate the two-dimensional probability, thus providing a degree of flexibility. There are more linear methods that are not covered in this work that could also be implemented in place for the two-dimensional probability computation. Another important aspect to the adjoining cylinders method is that these results required at most one minute to compute the collision probability for any case, including those involving highly nonlinear relative motion. This is drastically more computationally efficient than the Monte Carlo simulations and more accurate for almost every case than the linear methods.

3.2.2.1. Case 1. Knowing that Case 1 involves low relative velocity between two satellites in GEO, the nonlinear adjoining cylinders method should be able to accurately approximate the value of collision probability. The results from the adjoining cylinders method using the presented, normalized, two-dimensional probability computation differ by only 0.8% from the Monte Carlo results. It is clear that the nonlinear, adjoining cylinders method drastically improves upon the accuracy from the analytic linear methods, regardless of which two-dimensional implementation is used. The cumulative probability is illustrated in Figure 3.6.

Figure 3.6 is similar to the one presented for Case 1 in the Monte Carlo section, Figure 2.6, with two similar peaks, one around TCA and one 11,000 seconds later. It is crucial to use the same propagation time forward and backward with the adjoining cylinders method as was used in the Monte Carlo simulations; otherwise, the method will underestimate the collision probability.

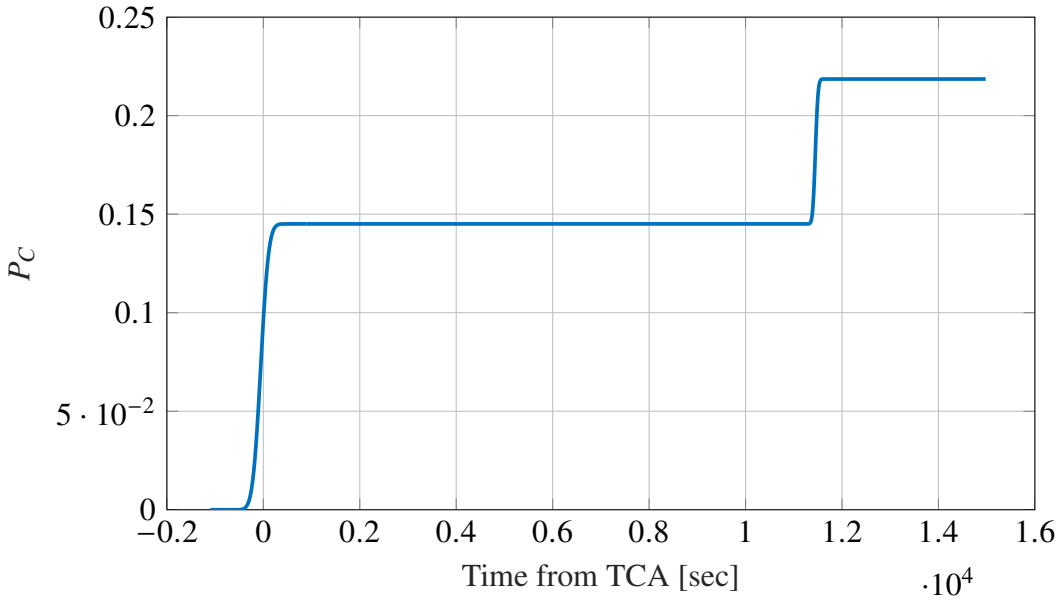

Figure 3.6. Cumulative probability for Case 1 using the adjoining cylinders method

3.2.2.2. Case 2. This case is essentially the same as Case 1; however, the hard-body radius is less than the nominal miss distance, effectively lowering the overall probability of collision. The values from the adjoining cylinders method differ by less than 5% from the Monte Carlo simulations. Figure 3.7 shows the cumulative probability of this case over the encounter region.

Figure 3.7 shows similar results to the Monte Carlo simulations as seen in Figure 2.8 with peaks occurring at the same time steps. An interesting observation is that this method overestimates the true probability of collision for this case and Case 1, which becomes the motivation for Section 5.

3.2.2.3. Case 3. This case involves linear relative motion in GEO; therefore, using a nonlinear method is not necessarily required, but the results show that approximation is essentially the same as was produced by the linear methods. In all of the linear cases, the one-dimensional probability should approach 1, as was discussed in Section 3.2.1.2, and the results produced in this work reflect that. Figure 3.8 illustrates the cumulative probability of collision expected from this approximation.

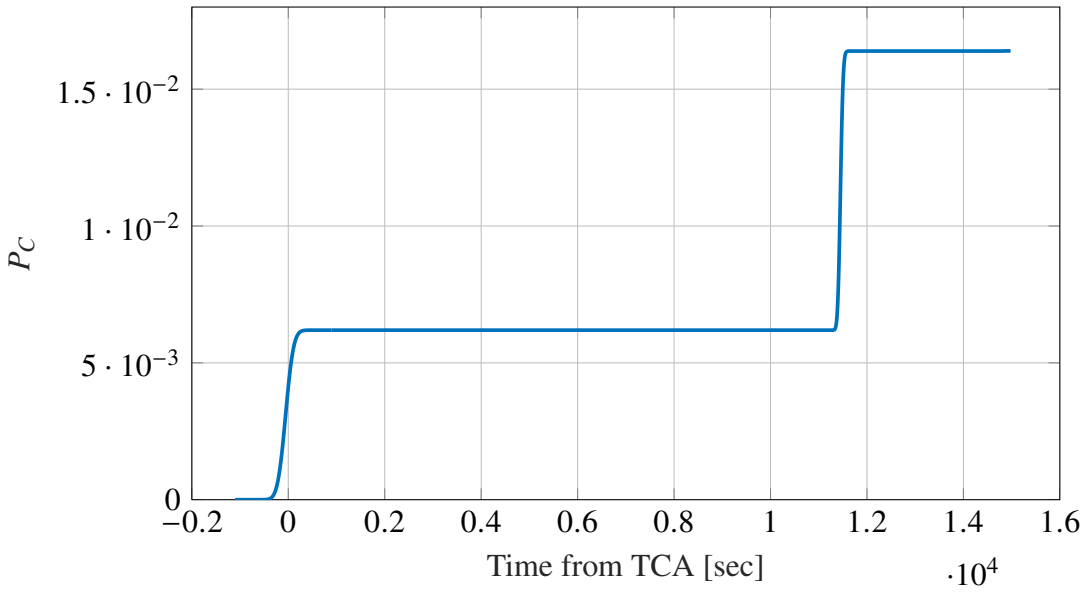

Figure 3.7. Cumulative probability for Case 2 using the adjoining cylinders method

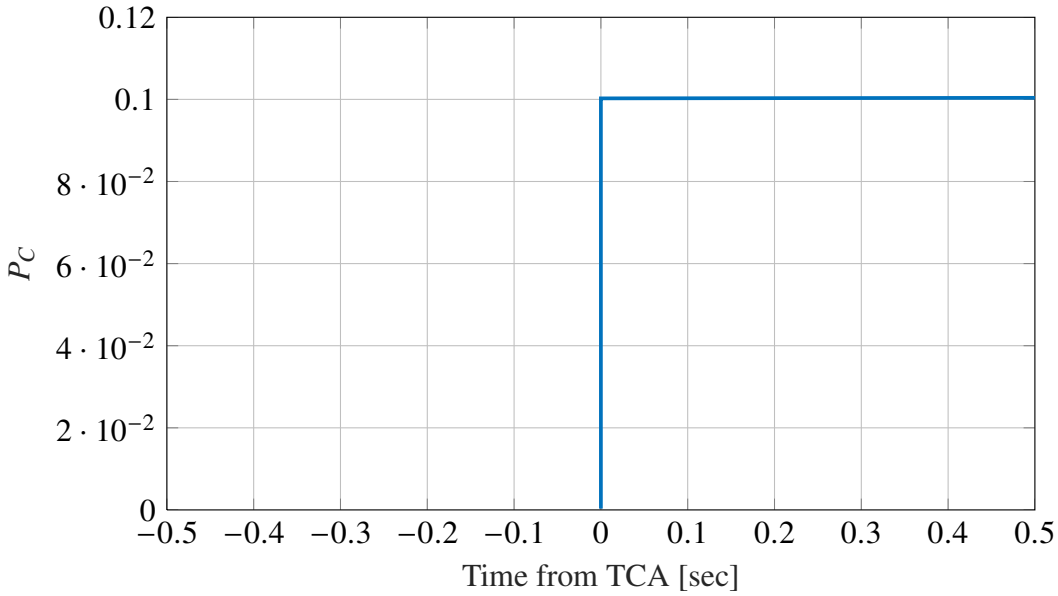

Figure 3.8. Cumulative probability for Case 3 using the adjoining cylinders method

Figure 3.8 shows that the method only picks out a single time for the encounter region. Most likely, this time is exactly at TCA because, for a true linear relative motion case, the only time step within the combined covariance shell should be right at the point of

closest approach. This specific case contains a steeper peak than the other linear cases due to the relative velocity being a factor of 10 greater than the relative velocity of any other case.

3.2.2.4. Case 4. An important note when implementing this method is that utilizing the relative velocity at TCA to define the length of the cylinders causes overlaps and gaps between them. This introduces some amount of error, which can be seen effectively in the implementation of Case 4. A refinement can be implemented at the edges of the cylinders so they merely touch and do not overlap (Alfano (2008)). The sizing of the cylinders is the most difficult task when implementing this method; any slight change among the cylinders catastrophically affects the results.

Case 4 shows the inaccuracies that can be generated from the gaps and overlaps of the adjoining cylinders. It is the inaccuracies of cases such as this one that drives the need to develop an alternative mitigation technique to simply maneuvering. Using the most accurate method that was derived in this work, the collision probability is still drastically underestimated. This would cause a mission spacecraft to not maneuver; however, from the Monte Carlo results in Table 2.2, it is apparent that there is a true possibility of a collision. Figure 3.9 shows that the cumulative probability follows the same shape as the Monte Carlo simulations but the cylinders miss enough of the encounter region that the probability is vastly underestimated.

Figure 3.9 illustrates that the probability of collision only begins to be accumulated some time after TCA and then continues to grow until plateauing when the primary spacecraft exits the encounter region.

3.2.2.5. Case 5. The results for Case 5 are essentially the same to those seen in the linear methods and Monte Carlo sections. This is a linear case with high relative velocity, and any of the methods will be able to accurately approximate the probability of collision. The trend of the cumulative probability can be seen in Figure 3.10.

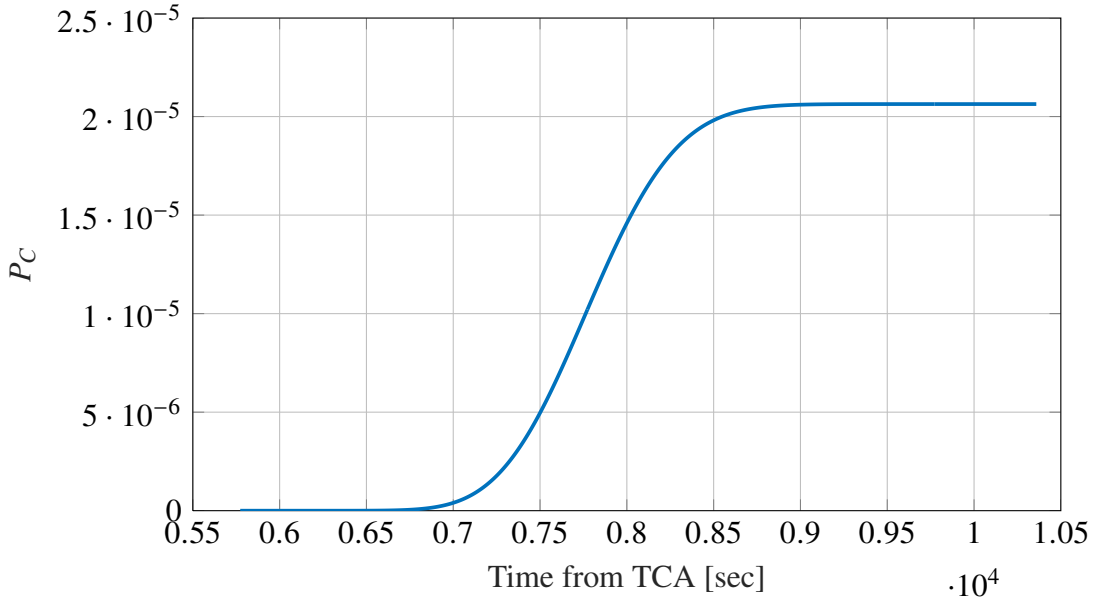

Figure 3.9. Cumulative probability for Case 4 using the adjoining cylinders method

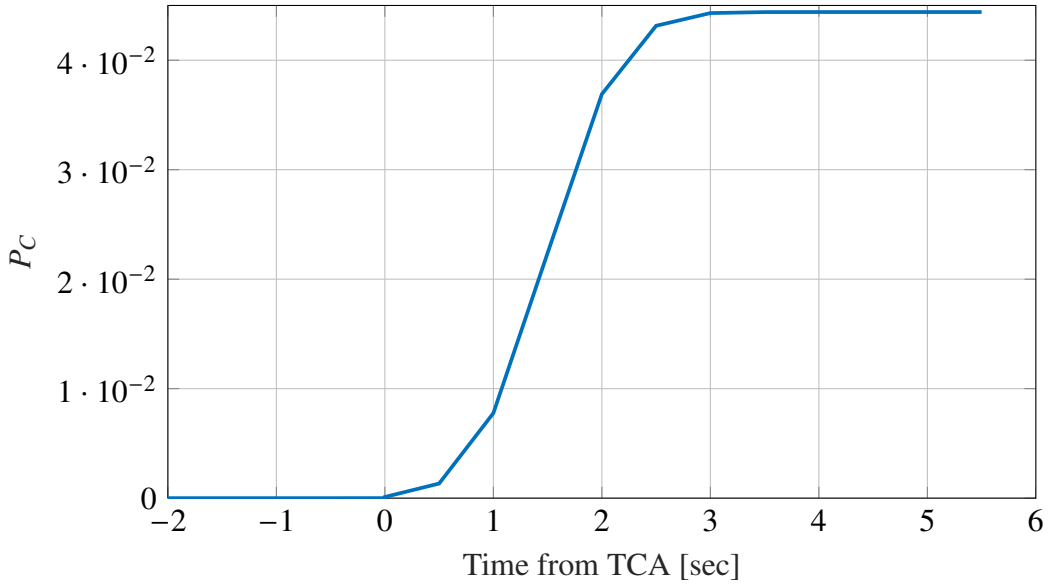

Figure 3.10. Cumulative probability for Case 5 using the adjoining cylinders method

Figure 3.10 shows that there is only a gradual peak in probability near TCA, which is what would be expected of a linear case. The sharp edges in Figure 3.10 illustrate the probability across each individual cylinder; if the step size of the propagation is decreased,

the number of cylinders would increase, smoothing out overall curve. However, this increase in cylinders would not increase the accuracy for the cumulative probability in this case because the time step of half a second is still sufficient.

3.2.2.6. Case 6. This case is similar to the previous one; it is a linear scenario in LEO, and any of the methods should be able to approximate the collision probability. One interesting aspect to this case is that the nonlinear method applied records multiple times when the hard-body object is within the combined covariance shell. This case is on the edge of being nonlinear, and the method treats it as such, so it becomes an interesting outcome to see such similar results to the linear methods. The trend of the cumulative collision probability can be seen in Figure 3.11. Figure 3.11 illustrates that this case can be considered as either linear or nonlinear and still produce accurate estimations of the Monte Carlo results.

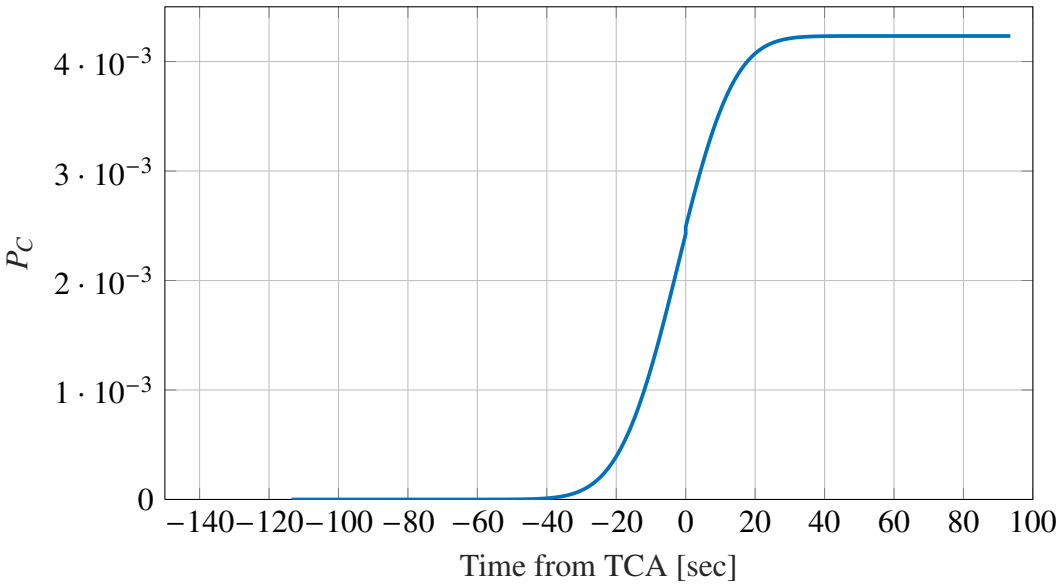

Figure 3.11. Cumulative probability for Case 6 using the adjoining cylinders method

4. BRIEF REVIEW OF KALMAN FILTERING

Given the developments thus far, it is apparent that the probability of collision is heavily dependent on not only the relative positions and velocities of the two objects, but also on the size of the combined covariance ellipsoid. The larger this ellipsoid, the higher likelihood that the hard-body sphere will occupy the same space, potentially increasing the probability of collision. In an attempt to decrease the likelihood of the hard-body occupying the ellipsoid, the combined covariance ellipsoid will have to shrink. The size of the ellipsoid is based on the confidence of the propagated position estimates of both objects. Currently, the covariance grows as these objects are propagated through time. To bound this growth, measurements of the states can be taken and used to refine the estimates of position and velocity, increasing the confidence in the states. Orbit determination accuracy can also have a large effect on the measurements taken in this work (Gottlieb *et al.* (2001)).

There are various methods of taking measurements to track objects as they orbit the Earth; for instance ground-based optical measurements or Global Positioning System (GPS) measurements can be used. Measurements are functionally dependent on the true states of the observed object through time. Optical measurements represent two angles that can be used to define the line of sight to the object at any time. The angles observed are dependent on the location of the observer. For example, astronauts on the International Space Station (ISS) could be using optical angle measurements to predict if a debris object will collide with them. The angles are then formed in a relative frame to the ISS (i.e. the observer). However, most angles-only measurements come from an optical observer on the surface of the Earth, such as the ground-based electro-optical deep space surveillance (GEODSS) site in Maui (Burgio and Grant (2011)). Angles measurement data can be utilized via a measurement model to correct estimated states, which will be seen in Section 5. The angles that will be used in this work are the right ascension, α, and declination, δ,

of the object at any time. Right ascension is the angular distance of an object measured eastward along the celestial equator from the vernal equinox, and declination is the angular distance measured from the equatorial plane to the object (Vallado (2004)). These astronomical coordinates specify the object in the equatorial coordinate system. While any measurements can be used in the estimation process, angles-only measurements are used in this work due to their prevalence in space object tracking methods.

It is important to note that there are some limitations to using optical measurements, such as the fact that measurements can only be taken at night, when the objects are visible. The objects have to be overhead, some degree above the horizontal of the observer, meaning that there is a limited time span at night that measurements can be taken. The limitations of measurements will be negligible in the scope of this work, as the goal is to simply illustrate the effects that measurements have on the probability of collision. Aside from taking measurements, there has been some discussion on better understanding the value of probability of collision itself because it can be seemingly arbitrary in some cases (Hejduk and Johnson (2016)).

4.1. KALMAN FILTER

With the chosen means of taking measurements, a model is now needed to implement the new information and develop an improved estimate of the states. One approach is to apply a Kalman filter to the propagation and updates of the state estimates and their associated covariances. A Kalman filter is an algorithm developed by Rudolph Kalman, used to process error-corrupted measurement data to better determine the parameters or variables associated with the process that generated the measurements (Lear (1985)). This means that angles-only measurements, such as α and δ, can be input into the filter, and the outputs will be estimates of the object's position and velocity at some time as well as the confidence in the estimates compared to the truth, i.e. the covariance. Kalman filtering has been used for many applications, including landing the lunar module on the surface of

the Moon (McGee and Schmidt (1985)). A Kalman filter processed Earth-based Doppler data as the lunar module approached the surface of the Moon and a real-time correction was voice-linked to the astronauts to adjust their position to ensure an accurate landing. Kalman filters have become useful and popular in modern estimation problems, especially those requiring real-time solutions.

The Kalman filter is typically composed of two stages, a propagation stage and an update stage. The propagation stage predicts the estimated states and covariance of the system one time step into the future. The update stage corrects the predicted states using measurements for a more confident estimation.

Assume that the system dynamics are given by,

$$\dot{\mathbf{x}}(t) = \mathbf{F}(t)\mathbf{x}(t) + \mathbf{M}(t)\mathbf{w}(t), \tag{4.1}$$

where $\mathbf{F}(t)$ is the linear dynamics of the states, $\mathbf{x}(t)$, at some time, t. The states for this application are the position and velocity of an object in Cartesian coordinates. In Equation (4.1), $\mathbf{M}(t)$ is a shape matrix that maps the zero-mean white-noise process, $\mathbf{w}(t)$, into the dynamics. It is assumed that the initial state has a mean $\mathbf{m}(t_0) = \mathbf{m}_0$ and a covariance $\mathbf{P}(t_0) = \mathbf{P}_0$. The mean of the state is taken to be a function of time, given by

$$\mathbf{m}(t) = E[\mathbf{x}(t)],$$

where $E[]$ is the expectation operator. Taking the time rate of change yields

$$\dot{\mathbf{m}}(t) = E[\dot{\mathbf{x}}(t)].$$

Appyling the expectation operator to the system dynamics yields

$$\dot{\mathbf{m}}(t) = E\left[\mathbf{F}(t)\mathbf{x}(t)\right] + E\left[\mathbf{M}(t)\mathbf{w}(t)\right].$$

Assuming $\mathbf{F}(t)$ and $\mathbf{M}(t)$ to be deterministic and recalling that the process noise is zero-mean, the time rate of change of the mean becomes

$$\dot{\mathbf{m}}(t) = \mathbf{F}(t)\mathbf{m}(t). \tag{4.2}$$

This becomes the prediction step for the mean, but a similar equation is needed for the prediction of the covariance. A similar, but lengthy derivation provides the covariance prediction equation as (Kalman, 1960)

$$\dot{\mathbf{P}}(t) = \mathbf{F}(t)\mathbf{P}(t) + \mathbf{P}(t)\mathbf{F}^T(t) + \mathbf{M}(t)\mathbf{Q}_s(t)\mathbf{M}^T(t), \tag{4.3}$$

where $\mathbf{Q}_s$ is the power spectral density, which is constant for white-noise processes. The mean and covariance from the previous update are given by

$$\mathbf{m}(t_{k-1}) = \mathbf{m}_{k-1}^+ \quad \text{and} \quad \mathbf{P}(t_{k-1}) = \mathbf{P}_{k-1}^+,$$

where the $(+)$ superscripts denote the mean and covariance after an update and the $(-)$ superscripts will denote the mean and covariance after a propagation. Propagating the equations for the mean and covariance from $t = t_{k-1}$ (the time of the previous update) to the time of the next measurement, $t = t_k$ yields the propagated mean and covariance, which are referred to as the *a priori* mean and covariance. The *a priori* mean and covariance are

$$\mathbf{m}_k^- = \mathbf{m}(t_k) \quad \text{and} \quad \mathbf{P}_k^- = \mathbf{P}(t_k),$$

where $\mathbf{m}(t_k)$ is the result of integrating Equation (4.2) from t_{k-1} to t_k and $\mathbf{P}(t_k)$ is the result of integrating Equation (4.3) from t_{k-1} to t_k. At time t_k the measurement $\mathbf{z}_k$, which is a function of the state, is given by

$$\mathbf{z}_k = \mathbf{H}_k\mathbf{x}_k + \mathbf{L}_k\mathbf{v}_k,$$

where $\mathbf{v}_k$ is the measurement noise, which is assumed to be a zero mean white-noise sequence with covariance $\mathbf{R}_k$. The new information provided by the measurement is then used to update the *a priori* mean and covariance of the state. Assuming that the *posteriori* mean is given by a linear combination of the *a priori* mean and the new measurement data, the *posteriori* estimate is

$$\mathbf{m}_k^+ = \mathbf{m}_k^- + \mathbf{K}_k \left[\mathbf{z}_k - \hat{\mathbf{z}}_k\right],$$

where $\hat{\mathbf{z}}_k$ is the expected measurement, which is based on the *a priori* state, and is given by

$$\hat{\mathbf{z}}_k = \mathbf{H}_k \mathbf{m}_k^-. \tag{4.4}$$

In Equation (4.4), $\mathbf{H}_k$ is the measurement mapping matrix that transforms the *a priori* mean into a measurement. The $\mathbf{K}_k$ is the linear Kalman gain, given as

$$\mathbf{K}_k = \mathbf{C}_k \mathbf{W}_k^{-1},$$

which is dependent on the innovations covariance, $\mathbf{W}_k$, and the cross covariance $\mathbf{C}_k$, these covariances are

$$\begin{aligned}\mathbf{W}_k &= \mathbf{H}_k \mathbf{P}_k^- \mathbf{H}_k^T + \mathbf{L}_k \mathbf{R}_k \mathbf{L}_k^T \\ \mathbf{C}_k &= \mathbf{P}_k^- \mathbf{H}_k^T,\end{aligned}$$

where it is assumed that $\mathbf{H}_k$ and $\mathbf{L}_k$ are deterministic and that the state is uncorrelated with measurement noise. Given the Kalman gain, innovation covariance, and cross covariance, the update step for the covariance is given by

$$\mathbf{P}_k^+ = \mathbf{P}_k^- - \mathbf{C}_k \mathbf{K}_k^T - \mathbf{K}_k \mathbf{C}_k^T + \mathbf{K}_k \mathbf{W}_k \mathbf{K}_k^T.$$

The equations used to propagate, take measurements, and update have now been presented in the scope of a Kalman filter. To summarize, these equations are used to take the initial estimated states of position and velocity in Cartesian coordinates and propagate them forward from some time, t_{k-1}, to t_k, which is one time step into the future. Then, measurements are taken at t_k and used to update the estimate to form more confidence in the states. This process is then repeated until some defined time is reached; for the scope of this work, the end time should be the time of closest approach, when both objects will be in conjunction. It is important to note that the Kalman filter strictly works on linear systems, which is inadequate in this case because the propagation of an object in orbit obeys a nonlinear dynamical model, and α and δ are nonlinear. Therefore, the Kalman filter must be modified to account for this nonlinearity.

4.2. NONLINEAR EXTENSIONS TO THE KALMAN FILTER

The Kalman filter operates on linear dynamical/observational systems, but some systems involve nonlinear dynamics, nonlinear measurements, or in this case, both. The scope of this work involves an object under the influence of two-body dynamics, which obeys a set a nonlinear differential equations in Cartesian coordinates; the angles-only measurements used in this process will also obey a set of nonlinear differential equations. To modify the Kalman filter to handle nonlinear systems, the extended Kalman filter (EKF) was developed. The EKF handles nonlinearity through the use of linearization. Using the EKF technique, estimated trajectories can be shown to converge to the true trajectories, even with large initial trajectory estimation errors (Grewal and Andews (2010)). In this variation, the nonlinear dynamical system is given by,

$$\dot{\mathbf{x}}(t) = \mathbf{f}(\mathbf{x}(t)) + \mathbf{M}(t)\mathbf{w}(t),$$

Where $\mathbf{f}(\mathbf{x}(t))$ is now the nonlinear dynamics of the states, $\mathbf{x}(t)$, at some time t. Once again, the time varying mean of the state is

$$\mathbf{m}(t) = E[\mathbf{x}(t)],$$

Taking the time derivative of this function and simplifying yields

$$\dot{\mathbf{m}}(t) = E[\dot{\mathbf{x}}(t)].$$

Applying the nonlinear system dynamics, it follows that

$$\dot{\mathbf{m}}(t) = E\left[\mathbf{f}(\mathbf{x}(t))\right] + E\left[\mathbf{M}(t)\mathbf{w}(t)\right] \tag{4.5}$$

To linearize the nonlinear dynamics, $\mathbf{f}(\mathbf{x}(t))$ can be expressed as a first-order Taylor series expansion about the mean as

$$\mathbf{f}(\mathbf{x}(t)) = \mathbf{f}(\mathbf{m}(t)) + \mathbf{F}(\mathbf{m}(t))(\mathbf{x}(t) - \mathbf{m}(t)) + H.O.T.,$$

where $H.O.T.$ denotes any higher order terms larger than a first order in the Taylor series and $\mathbf{F}(\mathbf{m}(t))$ is the dynamics Jacobian, defined as (Sorenson (1985))

$$\mathbf{F}(\mathbf{m}(t)) = \left[\left.\frac{\partial \mathbf{f}(\mathbf{x}(t))}{\partial \mathbf{x}(t)}\right|_{\mathbf{x}(t)=\mathbf{m}(t)}\right].$$

Substituting the first order Taylor series expansion into the expected value of the dynamics, Equation (4.5), yields

$$\dot{\mathbf{m}}(t) = E\left[\mathbf{f}(\mathbf{m}(t)) + \mathbf{F}(\mathbf{m}(t))(\mathbf{x}(t) - \mathbf{m}(t))\right] + E\left[\mathbf{M}(t)\mathbf{w}(\mathbf{t})\right].$$

Define the error in the mean with respect to the true state to be

$$\mathbf{e}(t) = \mathbf{x}(t) - \mathbf{m}(t).$$

Now, assuming that $\mathbf{f}(\mathbf{m}(t))$, $\mathbf{F}(\mathbf{m}(t))$, and $\mathbf{M}(t)$ are deterministic and recalling that the process noise, $\mathbf{w}(t)$, is taken to be zero-mean, the expected value of the nonlinear dynamics becomes

$$\dot{\mathbf{m}} = \mathbf{f}(\mathbf{m}(t)) + \mathbf{F}(\mathbf{m}(t))E\left[\mathbf{e}(t)\right]. \tag{4.6}$$

Also assuming that the estimate is unbiased, i.e. that $\mathbf{e}(t)$ is a zero mean process, then Equation (4.6) yields

$$\dot{\mathbf{m}} = \mathbf{f}(\mathbf{m}(t)). \tag{4.7}$$

This is the differential equation governing the forward evolution of the mean through time. The confidence in the mean, or the state estimation error covariance is found via

$$\mathbf{P}(t) = E\left[\mathbf{e}(t)\mathbf{e}^T(t)\right].$$

The derivation for the covariance prediction equation follows the same procedure as that used for the Kalman filter, but replacing the dynamics Jacobian, $\mathbf{F}(\mathbf{m}(\mathbf{t}))$, in place of $\mathbf{F}(t)$, yielding

$$\dot{\mathbf{P}}(t) = \mathbf{F}(\mathbf{m}(t))\mathbf{P}(t) + \mathbf{P}(t)\mathbf{F}^T(\mathbf{m}(t)) + \mathbf{M}(t)\mathbf{Q}_s(t)\mathbf{M}^T(t). \tag{4.8}$$

The mean and covariance are numerically integrated across the interval $t \in [t_{k-1}\ t_k]$ using Equations (4.7) and (4.8) with the initial conditions

$$\mathbf{m}(t_{k-1}) = \mathbf{m}^+_{k-1} \quad \text{and} \quad \mathbf{P}(t_{k-1}) = \mathbf{P}^+_{k-1}.$$

The values obtained after integrating Equations (4.7) and (4.8) over the time span become the *a priori* mean and covariance, $\mathbf{m}_k^-$ and $\mathbf{P}_k^-$. At time t_k, measurements are taken to be of the form

$$\mathbf{z}_k = \mathbf{h}(\mathbf{x}_k) + \mathbf{L}_k\mathbf{v}_k, \tag{4.9}$$

where $\mathbf{v}_k$ is still assumed to be a zero mean, white noise with covariance $\mathbf{R}_k$. Noting that the measurement model in Equation (4.9) is nonlinear, one can linearize in a similar method as with the dynamics model. Taking the expected value of Equation (4.9) yields

$$\hat{\mathbf{z}} = E\left[\mathbf{z}_k\right] = E\left[\mathbf{h}(\mathbf{x}_k)\right] + E\left[\mathbf{L}_k\mathbf{v}_k\right].$$

Linearizing the measurement function about the *a priori* mean expressed as a first-order Taylor series expansion via

$$\mathbf{h}(\mathbf{x}_k) = \mathbf{h}(\mathbf{m}_k^-) + \mathbf{H}(\mathbf{m}_k^-)(\mathbf{x}_k - \mathbf{m}_k^-) + H.O.T.,$$

where $\mathbf{H}((\mathbf{m}_k^-))$ is the measurement Jacobian and is defined as

$$\mathbf{H}(\mathbf{m}_k^-) = \left[\left.\frac{\partial \mathbf{h}(\mathbf{x}_k)}{\partial \mathbf{x}_k}\right|_{\mathbf{x}=\mathbf{m}}\right],$$

where $\mathbf{x} = \mathbf{x}_k$ and $\mathbf{m} = \mathbf{m}_k^-$ in the evaluation operator. Substituting the first-order Taylor series expression for the measurement model into the expected value of the measurement model yields

$$\hat{\mathbf{z}}_k = E\left[\mathbf{h}(\mathbf{m}_\mathbf{k}^-)\right] + E\left[\mathbf{H}(\mathbf{m}_\mathbf{k}^-)\mathbf{e}_k^-\right] + E\left[\mathbf{L}_k\mathbf{v}_k\right].$$

Assuming that $\mathbf{h}(\mathbf{m}_k^-)$, $\mathbf{H}(\mathbf{m}_k^-)$, and $\mathbf{L}_k$ are deterministic, recalling that the measurement noise is taken to be zero-mean, and assuming that the prediction error is to be zero-mean (unbiased), the expected value of the measurement is

$$\hat{\mathbf{z}}_k = \mathbf{h}(\mathbf{m}_k^-).$$

Once again, this new information is needed to update the mean and covariance. The update equation for the mean is given exactly as before, such that

$$\mathbf{m}_k^+ = \mathbf{m}_k^- + \mathbf{K}_k(\mathbf{z}_k - \hat{\mathbf{z}}_k),$$

where $\hat{\mathbf{z}}_k$ is still the expected measurement from the *a priori* mean. The equation to update the *a priori* covariance also remains the same, such that

$$\mathbf{P}_k^+ = \mathbf{P}_k^- - \mathbf{C}_k\mathbf{K}_k^T - \mathbf{K}_k\mathbf{C}_k^T + \mathbf{K}_k\mathbf{W}_k\mathbf{K}_k^T,$$

where the Kalman gain, $\mathbf{K}_k$, is given by

$$\mathbf{K}_k = \mathbf{C}_k\mathbf{W}_k^{-1},$$

where $\mathbf{C}_k$ is the cross covariance, and $\mathbf{W}_k$ is the innovations covariance, which are defined as

$$\begin{aligned} \mathbf{C}_k &= E\left[(\mathbf{x}_k - \mathbf{m}_k^-)(\mathbf{z}_k - \hat{\mathbf{z}}_k)^T\right] \\ \mathbf{W}_k &= E\left[(\mathbf{z}_k - \hat{\mathbf{z}}_k)(\mathbf{z}_k - \hat{\mathbf{z}}_k)^T\right]. \end{aligned} \tag{4.10}$$

Substituting in the measurement model, expected measurement, and recalling that $\mathbf{H}(\mathbf{m}_k^-)$ and $\mathbf{L}_k$ are deterministic, yields

$$\begin{aligned} \mathbf{W}_k &= \mathbf{H}(\mathbf{m}_k^-)\mathbf{P}_k^-\mathbf{H}^T(\mathbf{m}_k^-) + \mathbf{L}_k\mathbf{R}_k\mathbf{L}_k^T \\ \mathbf{C}_k &= \mathbf{P}_k^-\mathbf{H}^T(\mathbf{m}_k^-). \end{aligned} \tag{4.11}$$

The nonlinear extension to the Kalman filter has now been presented. Note that the EKF is a linear filter used for nonlinear systems. This work will use an EKF with angles only measurements, right ascension and declination, to better estimate the states of one or both of the objects at TCA. Thus, it is expected that a decrease in the uncertainty of the positions of the objects will be achieved, ultimately shrinking the size of the combined covariance ellipsoid.

It is an important note that there are various filters that can be used in place of the EKF, such as the Unscented Kalman filter (Julier and Uhlmann (1997)).

5. EFFECTS OF MEASUREMENTS ON THE PROBABILITY OF COLLISION

With the general EKF framework at hand, one requires expressions for the dynamics Jacobian, measurement Jacobian, and the nonlinear dynamical system used to propagate the states forward in time. Sections 5.1 and 5.2 will derive all of these expressions in terms of observing and taking measurements of an object in orbit. It is an important note that this work utilizes simple two body motion to describe the orbiting objects, which is sufficient for the scope of this work. The dynamics Jacobian and nonlinear dynamical model used to propagate the states presented in Section 5.2 are standard for any two body motion propagation. The measurement Jacobian presented in Section 5.2 is standard for an EKF only utilizing right ascension and declination measurements. This work will implement an EKF to estimate the states and covariance of the primary object to discern the effect that measurements will have on the probability collision. As well as using an EKF on both objects to discern if more measurements within the system will have a similar effect on the probability of collision.

5.1. ELEMENTS OF THE EKF

Keeping the framework of the EKF in mind, the Jacobians for both the measurement and the dynamical models have to be constructed. This work utilizes angles-only measurements in the form of right ascension, α, and declination, δ, defined as

$$\alpha = \arctan\left(\frac{\rho_y}{\rho_x}\right) \tag{5.1}$$

$$\delta = \arctan\left(\frac{\rho_z}{\sqrt{(\rho_x)^2 + (\rho_y)^2}}\right), \tag{5.2}$$

where the components of $\boldsymbol{\rho} = [\rho_x, \rho_y, \rho_z]^T$ are found as the difference between the position of the object object under observation, $\mathbf{r}$, and the position of a ground-based observer $\mathbf{q}$; that is,

$$\boldsymbol{\rho} = \mathbf{r} - \mathbf{q}. \tag{5.3}$$

Note that $\mathbf{r}$ and $\mathbf{q}$ are both given with respect to the center of the Earth in the Earth centered inertial frame. For this work, the observer is placed on the surface of the Earth, along the radial direction of the tracked object at epoch. Meaning that if measurements are being taken of the primary spacecraft, then the observer would be located on the surface of the Earth along the radial axis of the primary spacecraft; the same can be done with the secondary object. The observer can not be stationary with respect to the inertial frame, however, as it will remain fixed to the Earth while the observed object is orbiting. Noting that the observer is fixed to the Earth, then the time rate of change of the observer position at any time can by found using the transport theorem, or basic kinematics equation as

$$\dot{\mathbf{q}} = \frac{^I d}{dt}\{\mathbf{q}\} = \frac{^R d}{dt}\{\mathbf{q}\} + \boldsymbol{\omega}_{R/I} \times \mathbf{q} = \boldsymbol{\omega}_{R/I} \times \mathbf{q},$$

where the notation $\frac{d}{dt}\{\}$ denotes the time rate of change of some vector; and where I and R denote the inertial and rotating frames of the Earth, respectively, and $\boldsymbol{\omega}_{R/I}$ is

$$\boldsymbol{\omega}_{R/I} = \begin{bmatrix} 0 & 0 & \omega \end{bmatrix}^T,$$

where ω is the angular velocity of the Earth (7.292115 [rad/s]). Note that $\frac{d}{dt}\{\mathbf{q}\}$, with respect to the rotating frame, R, is zero in this case because the observer is fixed to the Earth. The velocity of the observer, $\dot{\mathbf{q}}$, is used to propagate the position of the observer through time. The velocity, however, does not remain constant; it, too, will evolve through

time according to

$$\ddot{\mathbf{q}} = \frac{^{I}d}{dt}\{\dot{\mathbf{q}}\} = \frac{^{R}d}{dt}\{\dot{\mathbf{q}}\} + \boldsymbol{\omega}_{R/I} \times \dot{\mathbf{q}} = \boldsymbol{\omega}_{R/I} \times \boldsymbol{\omega}_{R/I} \times \mathbf{q}.$$

As the observer's position and velocity propagate through time, so must the object's position and velocity. Initializing the propagation process with the positions and velocities of the object at epoch; keeping in mind that the position of each object will evolve through time based on the velocity at that time step, the velocity should then evolve by the acceleration at that time step. Given the position of an object, the acceleration is found from the nonlinear differential equation for the two-body problem, given by

$$\ddot{\mathbf{r}} + \frac{\mu}{||\mathbf{r}||^3}\mathbf{r} = \mathbf{0}, \tag{5.4}$$

where μ is the gravitational parameter of Earth (Prussing and Conway (2013)) and $||\mathbf{r}|| = r$, which is the magnitude of the position vector of the object. Solving for the acceleration of the object yields

$$\ddot{\mathbf{r}} = -\frac{\mu}{||\mathbf{r}||^3}\mathbf{r} = -\frac{\mu}{||\mathbf{r}||^3}\begin{bmatrix} x & y & z \end{bmatrix}^T = \begin{bmatrix} \ddot{x} & \ddot{y} & \ddot{z} \end{bmatrix}^T. \tag{5.5}$$

Equation (5.5) describes the acceleration of the object through time. The states of position and velocity will then evolve through time as

$$\dot{\mathbf{x}} = \mathbf{f}(\mathbf{x}(t)) = \begin{bmatrix} \dot{x} & \dot{y} & \dot{z} & \ddot{x} & \ddot{y} & \ddot{z} \end{bmatrix}^T, \tag{5.6}$$

where $\dot{x}$, $\dot{y}$, and $\dot{z}$ are the Cartesian components of the velocities of the object in the inertial frame. One can now propagate the observer's position and velocity, $\mathbf{q}$ and $\dot{\mathbf{q}}$, and the true position and velocity of the observed object, $\mathbf{x}(t)$, to time t. At time t, measurements can be generated in the form of right ascension and declination according to Equations (5.1) and

(5.2). These measurements are given by the true right ascension and declination corrupted by some white noise as

$$\mathbf{z}_k = \begin{bmatrix} \alpha \\ \delta \end{bmatrix} + \mathbf{v}_k,$$

where $\mathbf{v}_k$ is a zero mean with covariance

$$\mathbf{R}_k = \begin{bmatrix} 100 & 0 \\ 0 & 100 \end{bmatrix}. \tag{5.7}$$

It is important to note that $\mathbf{R}_k$ is in (arcseconds)^2, and the measurements, α and δ, are in arcseconds. Note that the $\mathbf{L}_k$ in Equation (4.9) is an identity matrix. The measurements, $\mathbf{z}_k$, are then passed into the EKF to estimate the states of the observed object.

5.2. CONSTRUCTING THE EKF

The EKF is initialized with the mean, $\mathbf{m}_{k-1}^{+}$, and covariance, $\mathbf{P}_{k-1}^{+}$, where the initial mean, $\mathbf{m}_{k-1}^{+}$, is taken as the position and velocity of the observed object at epoch, and the initial covariance, $\mathbf{P}_{k-1}^{+}$, is the covariance of the observed object at epoch. The initial mean and covariance are then propagated using Equations (4.7) and (4.8) by numerically integrating to time t_k to obtain the *a priori* mean and covariance. Note that the power spectral density, $\mathbf{Q}_s$, in Equation (4.8) is zero for this work. The nonlinear dynamical model that predicts the states of the mean are the same derived in Equation (5.6). The covariance propagation, however, requires the formation of the dynamics Jacobian, which

is defined by

$$\mathbf{F}(\mathbf{x}(t)) = \begin{bmatrix} \frac{\partial \dot{x}}{\partial x} & \frac{\partial \dot{x}}{\partial y} & \frac{\partial \dot{x}}{\partial z} & \frac{\partial \dot{x}}{\partial \dot{x}} & \frac{\partial \dot{x}}{\partial \dot{y}} & \frac{\partial \dot{x}}{\partial \dot{z}} \\ \frac{\partial \dot{y}}{\partial x} & \frac{\partial \dot{y}}{\partial y} & \frac{\partial \dot{y}}{\partial z} & \frac{\partial \dot{y}}{\partial \dot{x}} & \frac{\partial \dot{y}}{\partial \dot{y}} & \frac{\partial \dot{y}}{\partial \dot{z}} \\ \frac{\partial \dot{z}}{\partial x} & \frac{\partial \dot{z}}{\partial y} & \frac{\partial \dot{z}}{\partial z} & \frac{\partial \dot{z}}{\partial \dot{x}} & \frac{\partial \dot{z}}{\partial \dot{y}} & \frac{\partial \dot{z}}{\partial \dot{z}} \\ \frac{\partial \ddot{x}}{\partial x} & \frac{\partial \ddot{x}}{\partial y} & \frac{\partial \ddot{x}}{\partial z} & \frac{\partial \ddot{x}}{\partial \dot{x}} & \frac{\partial \ddot{x}}{\partial \dot{y}} & \frac{\partial \ddot{x}}{\partial \dot{z}} \\ \frac{\partial \ddot{y}}{\partial x} & \frac{\partial \ddot{y}}{\partial y} & \frac{\partial \ddot{y}}{\partial z} & \frac{\partial \ddot{y}}{\partial \dot{x}} & \frac{\partial \ddot{y}}{\partial \dot{y}} & \frac{\partial \ddot{y}}{\partial \dot{z}} \\ \frac{\partial \ddot{z}}{\partial x} & \frac{\partial \ddot{z}}{\partial y} & \frac{\partial \ddot{z}}{\partial z} & \frac{\partial \ddot{z}}{\partial \dot{x}} & \frac{\partial \ddot{z}}{\partial \dot{y}} & \frac{\partial \ddot{z}}{\partial \dot{z}} \end{bmatrix}.$$

With the equation of motion for the observed object known from Equation (5.6), and knowing that the position of the object evolves based on the velocity, the Jacobian becomes

$$\mathbf{F} = \begin{bmatrix} 0 & 0 & 0 & 1 & 0 & 0 \\ 0 & 0 & 0 & 0 & 1 & 0 \\ 0 & 0 & 0 & 0 & 0 & 1 \\ \frac{-\mu}{r^3} + \frac{3\mu x^2}{r^5} & \frac{3\mu xy}{r^5} & \frac{3\mu xz}{r^5} & 0 & 0 & 0 \\ \frac{3\mu yx}{r^5} & -\frac{\mu}{r^3} + \frac{3\mu y^2}{r^5} & \frac{3\mu yz}{r^5} & 0 & 0 & 0 \\ \frac{3\mu zx}{r^5} & \frac{3\mu zy}{r^5} & -\frac{\mu}{r^3} + \frac{3\mu z^2}{r^5} & 0 & 0 & 0 \end{bmatrix}.$$

Now, one has the capability of obtaining the *a priori* mean and covariance by numerically integrating Equations (4.7) and (4.8) to time t_k.

The *posteriori* mean and covariance are found by processing the measurements, $\hat{\mathbf{z}}_k$. Recall that the expected measurement is computed as

$$\hat{\mathbf{z}} = \begin{bmatrix} \hat{\alpha} \\ \hat{\delta} \end{bmatrix},$$

where $\hat{\alpha}$ and $\hat{\delta}$ are computed by evaluating Equations (5.1) and (5.2) at $\mathbf{m}_k^-$. The estimated measurement, $\hat{\mathbf{z}}_k$, depends on the relative position between the observer at time t_k and the *a priori* mean, whereas $\mathbf{z}_k$ depends on the relative position between the observer at time t_k and the true position of the object within $\mathbf{x}(t)$ defined in Equation (5.3). In the EKF, the

measurements need to be mapped into the dynamics space to be used for the update step via the measurement Jacobian formed by

$$\mathbf{H} = \begin{bmatrix} \frac{\partial \alpha}{\partial x} & \frac{\partial \alpha}{\partial y} & \frac{\partial \alpha}{\partial z} & \frac{\partial \alpha}{\partial \dot{x}} & \frac{\partial \alpha}{\partial \dot{y}} & \frac{\partial \alpha}{\partial \dot{z}} \\ \frac{\partial \delta}{\partial x} & \frac{\partial \delta}{\partial y} & \frac{\partial \delta}{\partial z} & \frac{\partial \delta}{\partial \dot{x}} & \frac{\partial \delta}{\partial \dot{y}} & \frac{\partial \delta}{\partial \dot{z}} \end{bmatrix}.$$

Calculating the measurement Jacobian from Equations (5.1) and (5.2) yields

$$\mathbf{H} = \begin{bmatrix} H_{11} & H_{12} & 0 & 0 & 0 & 0 \\ H_{21} & H_{22} & H_{23} & 0 & 0 & 0 \end{bmatrix},$$

where

$$\begin{aligned} H_{11} &= -\frac{\rho_y}{(\rho_x)^2 + (\rho_y)^2} \\ H_{12} &= -\frac{\rho_x}{(\rho_x)^2 + (\rho_y)^2} \\ H_{21} &= -\frac{\rho_z \rho_x}{((\rho_x)^2 + (\rho_y)^2)\sqrt{(\rho_x)^2 + (\rho_y)^2 + (\rho_z)^2}} \\ H_{22} &= \frac{\rho_z \rho_y}{((\rho_x)^2 + (\rho_y)^2)\sqrt{(\rho_x)^2 + (\rho_y)^2 + (\rho_z)^2}} \\ H_{23} &= \frac{\sqrt{(\rho_x)^2 + (\rho_y)^2}}{(\rho_x)^2 + (\rho_y)^2 + (\rho_z)^2}, \end{aligned}$$

where it is reminded that $\boldsymbol{\rho} = \begin{bmatrix} \rho_x, \rho_y, \rho_z \end{bmatrix}^T$ is the relative position of the estimated object with respect to the observer. Now, everything needed to update the *a prior* estimate to the *a posteriori* is readily available and is done by

$$\mathbf{m}_k^+ = \mathbf{m}_k^- + \mathbf{K}_k \left(\mathbf{z}_k - \hat{\mathbf{z}}_k \right).$$

The *a posteriori* covariance can also be generated by

$$\mathbf{P}_k^+ = \mathbf{P}_k^- - \mathbf{C}_k\mathbf{K}_k^T - \mathbf{K}_k\mathbf{C}_k^T + \mathbf{K}_k\mathbf{W}_k\mathbf{K}_k^T,$$

where

$$\begin{aligned}\mathbf{K}_k &= \mathbf{C}_k\mathbf{W}_k^{-1}\\ \mathbf{W}_k &= \mathbf{H}_k\mathbf{P}_k^-\mathbf{H}_k^T + \mathbf{R}_k\\ \mathbf{C}_k &= \mathbf{P}_k^-\mathbf{H}_k^T.\end{aligned}$$

The *a posteriori* mean and covariance are then propagated to the next time step, forming a new set of *a priori* mean and covariance, forming an iterative process. This is continued until a specified time is reach, in this case, TCA.

5.3. IMPLEMENTING SELECT CASES

Three cases are chosen to investigate the effects of processing data via the EKF on the probability of collision. The three chosen cases are Cases 1, 2, and 5. Case 1 is simply chosen due to the fact that it has the exact same trajectory as Case 2, making them easy to compare. Case 2 is chosen because the combined hard-body sphere should partially overlap the covariance ellipsoid. If the covariance shrinks due to processing measurements in this case, then the probability of collision should decrease. The inverse can be said about Case 5, which has a hard-body sphere that is completely engulfed by the covariance ellipsoid. Cases 1 and 2 both involve two objects in GEO, and they both require $280,800$ seconds after epoch to reach the conjunction time (TCA). These cases are implemented using 60 measurements, centered at the time halfway between epoch and TCA, defined as T_m. Case 5 involves two objects in LEO, which has a much smaller period than the cases in GEO. Therefore, only 20 measurements are considered to estimate the state of the object. It is

Table 5.1. Effects of measurements of the primary object on probability of collision

	Patera's Linear Method $P_{C,cum}$	**Adj. Cylinders Patera's** 2-d $P_{C,cum}$	**Adj. Cylinders Normalized** $P_{C,cum}$
Case 1	0.132245	0.196259	0.195181
Case 2	0.005739	0.012380	0.012014
Case 5	0.052903	0.052091	0.051980

important to note that the observer generating the measurements is simply placed on the surface of the Earth relative to the radial axis of the observed object. While this does not indicate a real application observer, it is sufficient for the scope of this work. Extending the implementation of this process to utilize real observation sites is reasonably straight forward.

The implementation of Cases 1, 2, and 5 involve taking measurements of only the primary object, then using those measurements in the defined EKF to refine the state estimates and reduce the uncertainty in the estimate. A second implementation is conducted in which measurements of both the primary and secondary objects are used to refine the state estimates of both objects. In both implementations, it is expected that the refined state estimates will lead to an alteration of the probability of collision.

5.3.1. Measurements on Only Primary Spacecraft. Implementing the first scenario, where only measurements of the primary object yields the results, shown in Table 5.1. It is important to note that all of the collision probability in the results presented in this section are computed from the nonlinear adjoining cylinders method using Equation (3.22) for the two dimensional contributions.

5.3.1.1. Case 1. From the nonlinear results in Section 3.2.2, it is known that the adjoining cylinders nonlinear method estimated the probability of collision for Case 1 to be 0.218165 using Equation (3.22). Taking measurements of only the primary object leads

to the covariance (in [m] and [m/s]) at TCA of the primary object being

$$\mathbf{C}_p = \begin{bmatrix} 6272.6915 & -363.22411 & -2.0790739 \times 10^{-7} \\ -363.22410 & 21.806126 & 1.1943 \times 10^{-8} \\ -2.0791 \times 10^{-7} & 1.1943 \times 10^{-8} & 1.2050205 \end{bmatrix}. \tag{5.8}$$

Comparing Equation (5.8) to the value given by Equation (1) in the Appendix, it is seen that a slightly smaller covariance of this object at TCA is obtained by processing measurement data. The effect that these measurements has on the probability of collision can be seen in Figure 5.1.

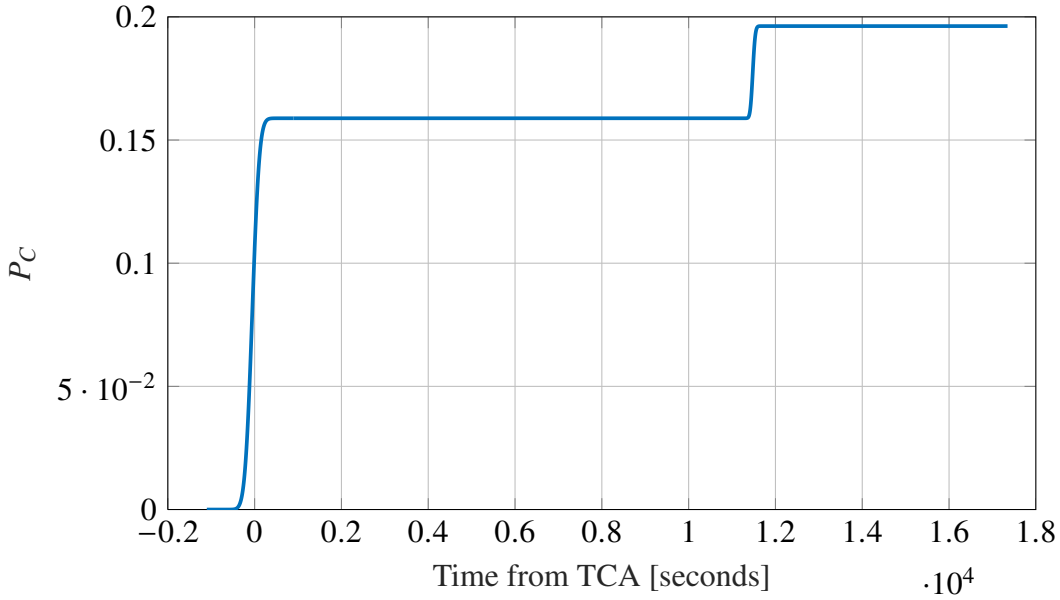

Figure 5.1. Cumulative probability of collision for Case 1 with primary-only measurements

Figure 5.1 illustrates that the probability of collision decreased for Case 1 by nearly 11% to 0.195181 as seen in Table 5.1. This probability of collision now indicates that there will still be a collision, but the combined hard-body sphere is not entirely encompassed within the covariance ellipsoid during the entire encounter region. The states of the primary object from the EKF in Case 1 can be seen in Figures 5.2 and 5.3.

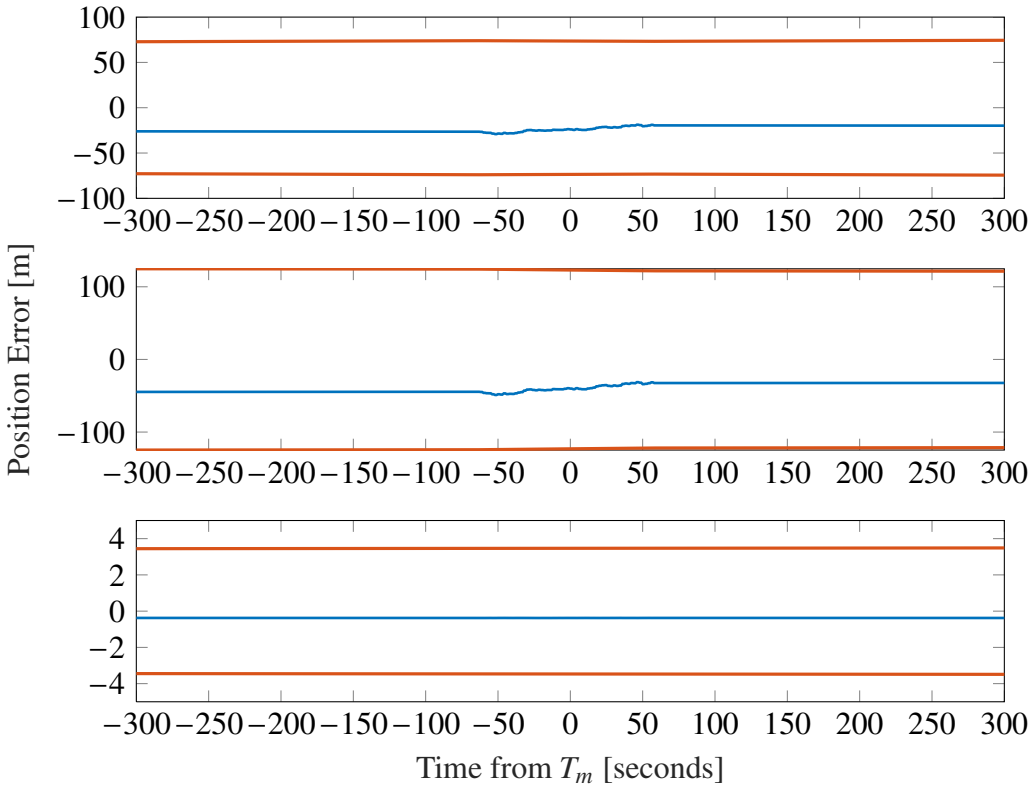

Figure 5.2. Position errors and uncertainties for Case 1 with primary-only measurements

The orange lines in Figures 5.2 and 5.3 denote the 3σ interval defined by the *a priori* and *a posteriori* covariance, and the position and velocity errors, denoted by the blue lines, are generated by the difference between the estimated state and the true state of the observed object. For Case 1, 60 measurements are simulated, centered about the time T_m = 140,400 seconds from epoch, which is half of the time to conjunction. The effect of the measurements can plainly be seen in Figures 5.2 and 5.3, as the squiggly lines that appear as disturbances to the flat estimate change. Figures 5.2 and 5.3 illustrate that the state estimates barely change over each time step, but tend to drift, either up or down, depending on the state component. It is important to note that the position error and velocity error in the z-direction appear as horizontal lines with no disturbances, this is because the states of

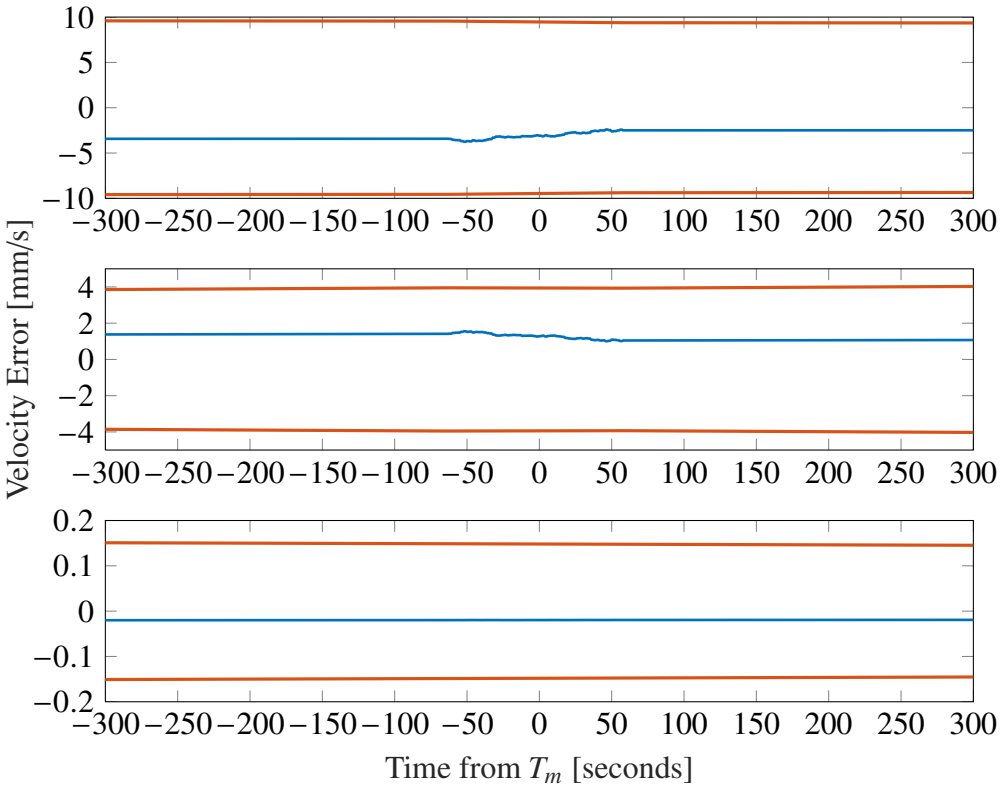

Figure 5.3. Velocity errors for Case 1 with primary-only measurements

these components are so close to zero that the measurements barely drift the states from zero before they inevitably drift back, the drift is so negligibly small that it appears as if measurements have no effect on these components.

If one expands the limits of Figures 5.2 and 5.3 to encompass the entire time from epoch to TCA, then a highly oscillatory motion appears. The highly oscillatory motion within the errors and intervals is generated by the multiple orbital periods that occur during the propagation from epoch to TCA.

5.3.1.2. Case 2. From the nonlinear results in Section 3.2.2, it is known that the nonlinear adjoining cylinders method estimated the probability of collision for Case 2 to be 0.016239 using Equation (3.22). Taking and processing measurements of only the primary

object results in the covariance (in [m] and [m/s]) of the primary object at TCA to be

$$\mathbf{C}_p = \begin{bmatrix} 6272.6915 & -363.22402 & -2.0791 \times 10^{-7} \\ -363.22402 & 21.806116 & 1.1943 \times 10^{-8} \\ -2.0791 \times 10^{-7} & 1.1943 \times 10^{-8} & 1.2050205 \end{bmatrix}, \tag{5.9}$$

which is a slight decrease from the original covariance of the primary object at TCA, as seen in the Appendix. This once again shows that only 60 measurements, each one second apart during a time span of 280,800 seconds, can affect the covariance of the states. The effect that these measurements have on the probability of collision can be seen in Figure 5.4.

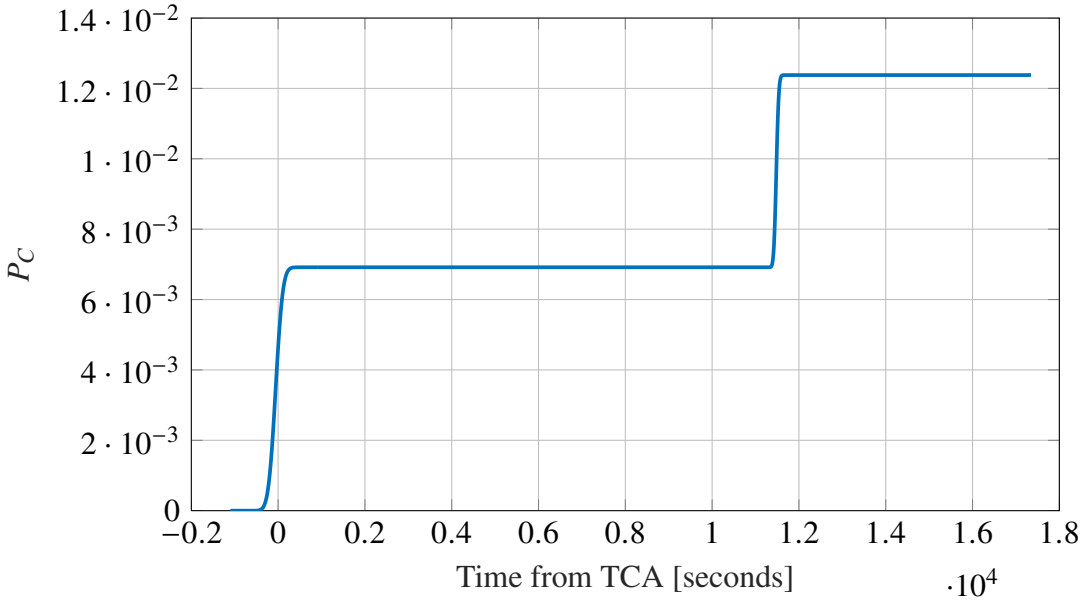

Figure 5.4. Cumulative probability of collision for Case 2 with primary-only measurements

Figure 5.4 illustrates that the collision probability dropped by 26% to 0.012014 from the original value, 0.016239. This is a significant decrease in collision probability for only utilizing 60 measurements. The state estimation errors and associated uncertainties of the primary object from the EKF in Case 2 can be seen in Figures 5.5 and 5.6.

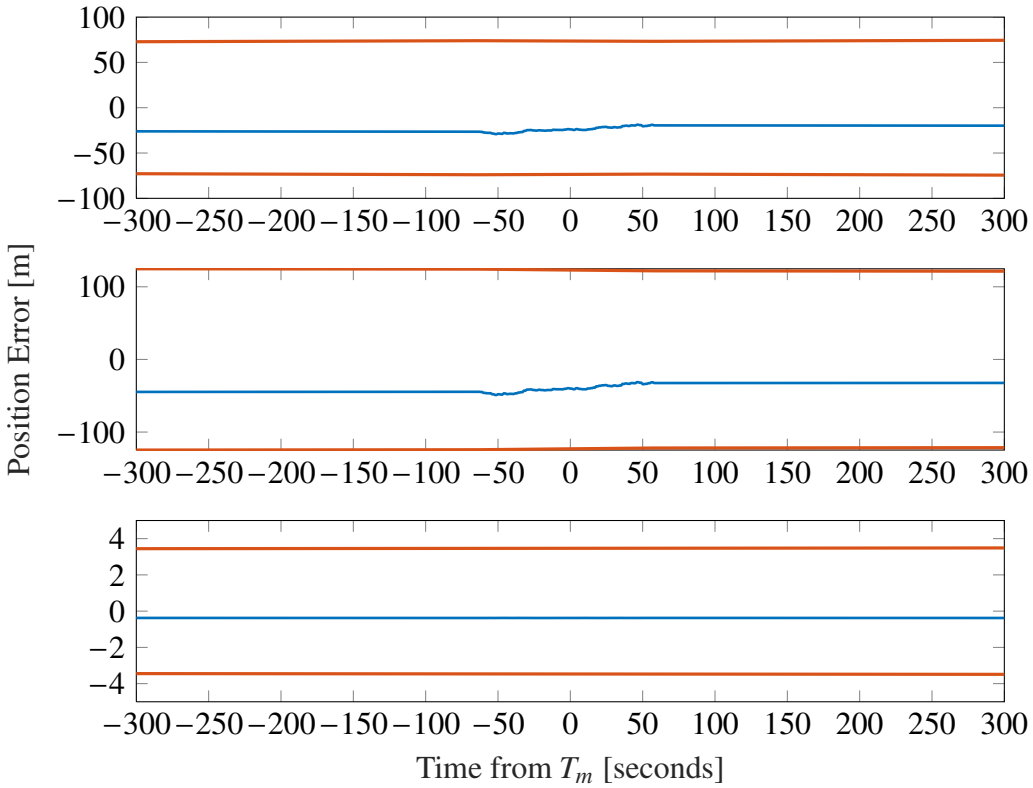

Figure 5.5. Position errors for Case 2 with primary-only measurements

Figures 5.5 and 5.6 illustrate similar estimates as those from Case 1. The trajectories of the primary spacecraft between Case 1 and Case 2 are the exact same, and the estimates are extremely close, the difference coming from the random numbers attributed to the measurements. The measurements in Figures 5.5 and 5.6 are seen to have very little effect on the states and almost no discernible effect updating the covariance, but the final value of the covariance at TCA can be seen as a decrease from the original value. If one were to expand the times of Figures 5.5 and 5.6, the same highly oscillatory motion described for Case 1 would be seen. The reasoning for only illustrating this small amount of the EKF results is to view the effects of taking measurements and updating the mean and covariance have on the states, mainly the placement of the primary object and the size of the combined covariance ellipsoid at TCA.

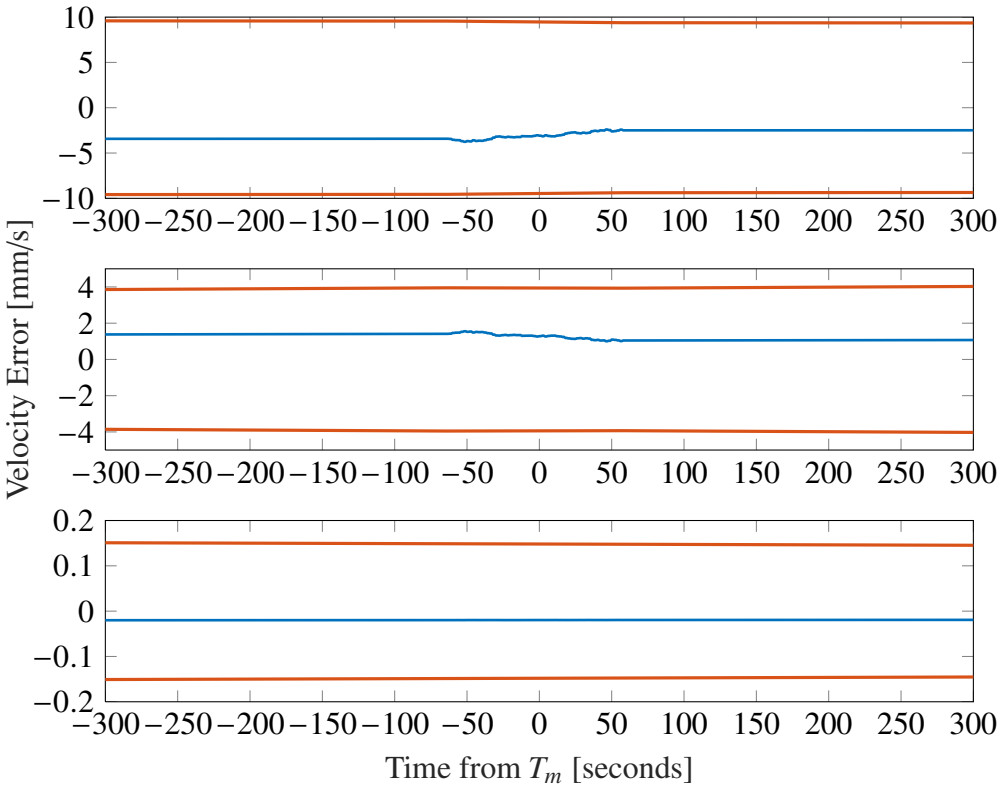

Figure 5.6. Velocity errors for Case 2 with primary-only measurements

5.3.1.3. Case 5. From the nonlinear results in Section 3.2.2, it is known that the nonlinear adjoining cylinders method estimated the probability of collision for Case 5 to be 0.044385. This case only utilizes 20 measurements centered about half the time from epoch to TCA, which 86,400 seconds after epoch. Taking 20 measurements of only the primary object shrinks the covariance (in [m] and [m/s]) of the primary object to

$$\mathbf{C}_p = \begin{bmatrix} 0.03708312 & -7.80692029 & -7.80691709 \\ -7.80692029 & 3293.5183 & 3293.4385 \\ -7.80691709 & 3293.4385 & 3293.5156 \end{bmatrix}, \tag{5.10}$$

which is about half the original covariance of the primary object at TCA, as seen in Equation (5) in the Appendix. This is a significant decrease in covariance compared to the first two cases. Case 5 is the only case involving LEO motion from the three selected cases; therefore, the number of measurements is decreased from 60 to 20, but there is still an immense difference in the change of covariance, partly because the size hard-body sphere is fixed so the data is more informative. The effect that the 20 measurements have on the probability of collision can be seen in Figure 5.7.

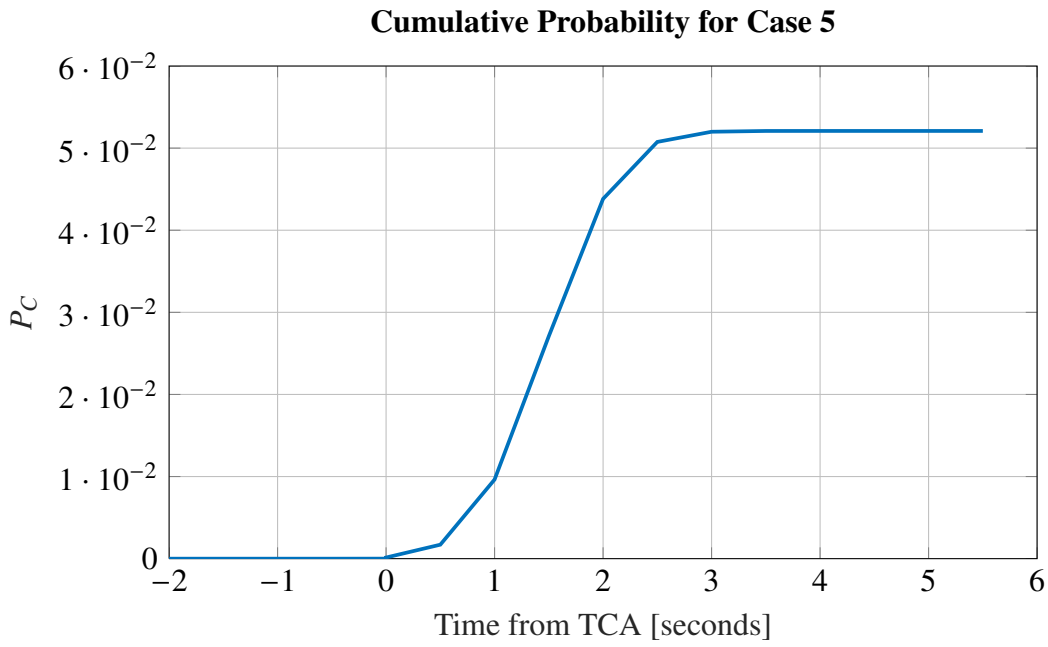

Figure 5.7. Cumulative probability of collision for Case 5 with primary-only measurements

Figure 5.7 illustrates that the probability of collision increased 17% from 0.044385 to 0.051980. This is the first case that the probability of collision increases from a decrease in covariance. This becomes exceptionally important, because it can be seen that utilizing measurements to update the states of the objects, decreasing the size of the covariance, can in fact result in a more definite possibility of collision. This begins to validate the idea that measurements can be taken of the primary object in order to obtain a more confident

probability of collision, providing an alternative to simply maneuvering based on a threshold value. The states of the primary object from the effects of updating via the generated measurements can be seen in Figures 5.8 and 5.9.

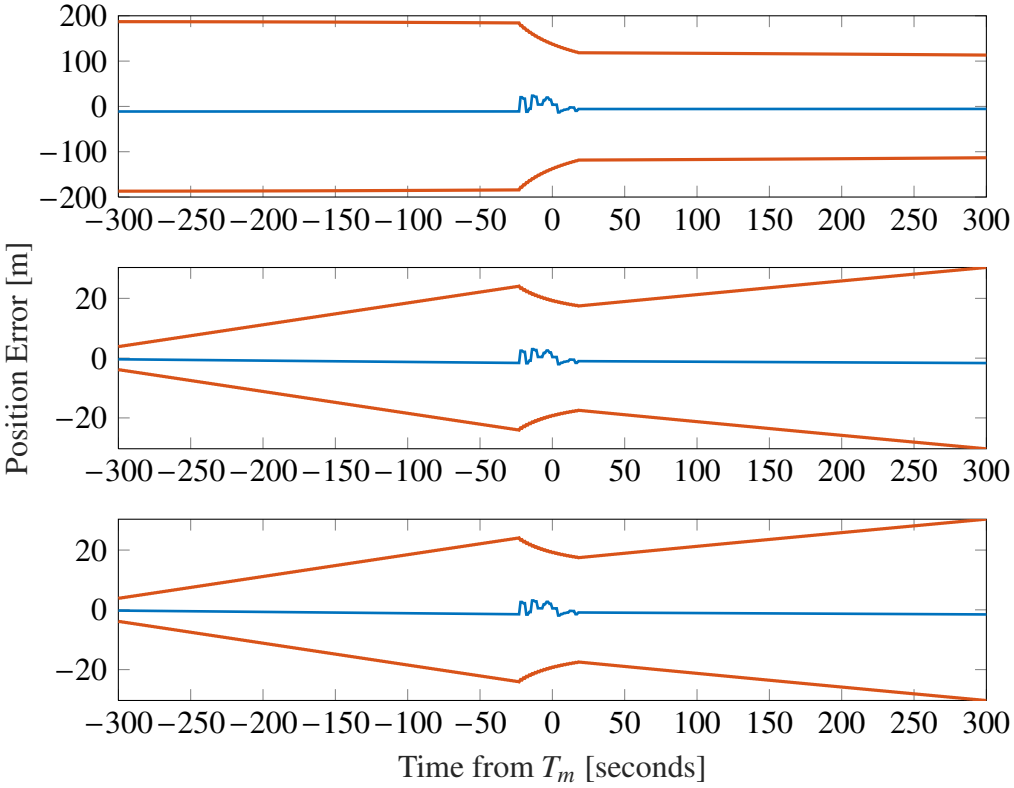

Figure 5.8. Position errors for Case 5 with primary-only measurements

Figures 5.8 and 5.9 illustrate the oscillatory motion in the covariance, described in the results section for Cases 1 and 2. Figures 5.8 and 5.9 show how the covariance generally grows over time, then has a sharp decrease as it is updated with the new measurement information. At the same time, the position and velocity errors can be seen to stray from the zero-line due to the noise in the measurements.

5.3.1.4. Monte Carlo study. The random measurement noise used to corrupt the measurements results in random outcomes for the results. Without a set random number seed, the measurements will affect the covariance and the states in a way that may possibly result in either a growth or decrease in collision probability for any chosen case. Suppose that the primary object is originally located just outside of the combined covariance el-

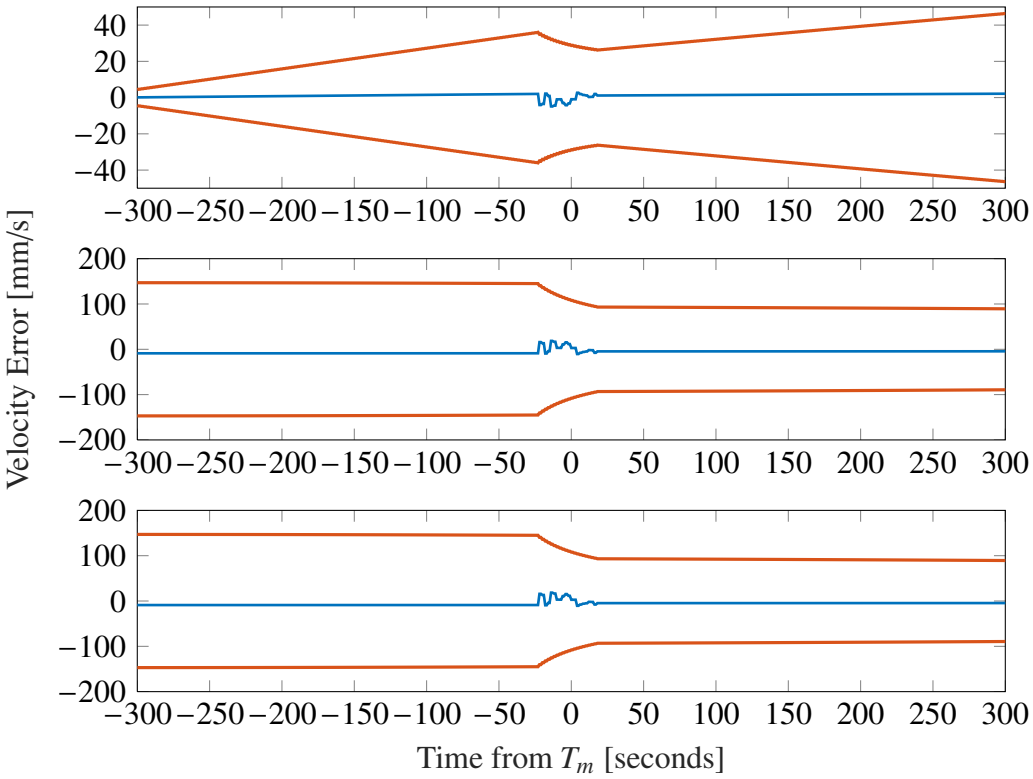

Figure 5.9. Velocity errors for Case 5 with primary-only measurements

lipsoid, the hard-body sphere would barely cross the ellipsoid, generating some value of collision probability. Processing one possible set of measurements may place the new primary deeper inside the ellipsoid, increasing the collision probability. Processing a different set of measurements over the exact same interval may place the primary object further outside the ellipsoid, decreasing the collision probability. The question then has to be asked, what is the overall effect of the measurements on the probability of collision? A Monte Carlo simulation is conducted to evaluate this process with 200 trials on a single case. Case 5 is chosen because it can be deduced from the relative geometry that a decrease in covariance should increase the overall probability of collision. Figure 5.10 shows the results of these 200 trials on Case 5 through the effect of measurements of only the primary object.

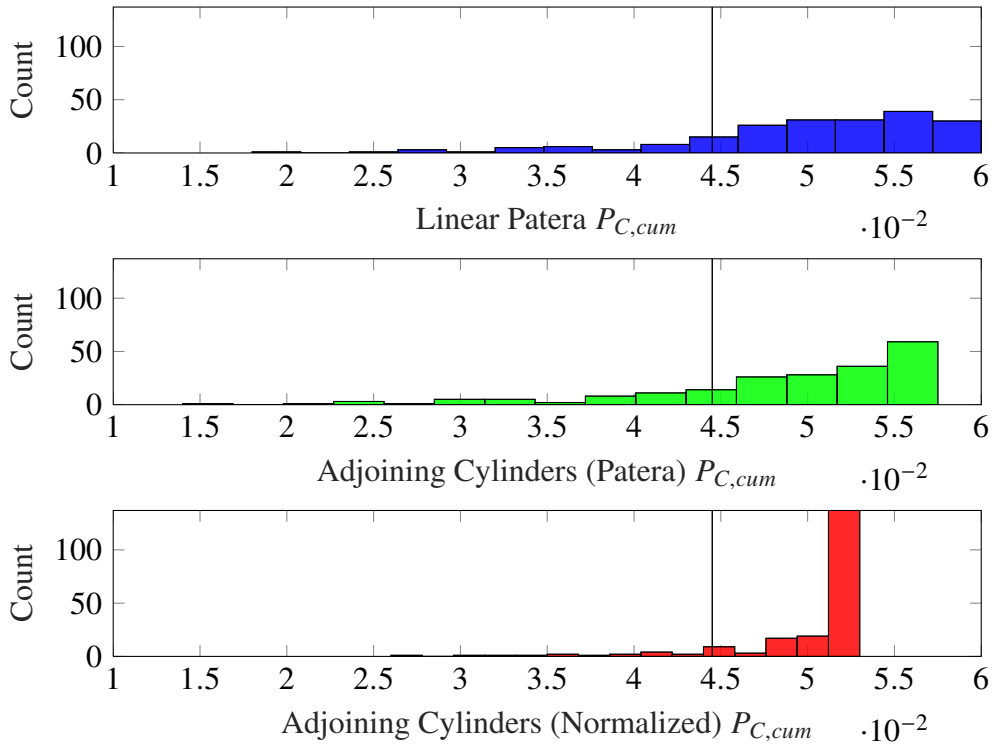

Figure 5.10. Histograms of the trials for the probability of collision for Case 5

The first subplot in Figure 5.10 are the results for the 200 trials where the probability of collision is calculated with Patera's linear method. The remaining two subplots are the probability of collision results of the 200 trials calculated by the two nonlinear adjoining cylinders methods introduced in Section 3. The black vertical line in all three subplots denotes the probability of collision for Case 5 without any measurements. It is clear from the results of Figure 5.10 that at least two-thirds of the trials from Case 5, the probability of collision increased. However, the random numbers used to corrupt the measurements can cause the collision probability of Case 5 to drop as low as 0.015.

5.3.2. Measurements on Both Objects. If taking measurements to update the states of one object were to decrease the probability of collision, then taking measurements of both objects could decrease the probability of collision further. This section implements the exact same process as observing only the primary object, but now both objects are observed for the same three cases during the same times. Cases 1 and 2 utilize 60 mea-

Table 5.2. Effects of measurements on both objects on probability of collision

	Patera's Linear Method $P_{C,cum}$	**Adj. Cylinders Patera's** 2-d $P_{C,cum}$	**Adj. Cylinders Normalized** $P_{C,cum}$
Case 1	0.143477	0.207722	0.207134
Case 2	0.006139	0.014338	0.014128
Case 5	0.068887	0.070144	0.070033

surements for each object and Case 5 uses 20, all centered about the time halfway between epoch and TCA. The results for the three chosen cases can be seen in Table 5.2 and will be discussed further in later sections.

5.3.2.1. Case 1. From Section 5.3.1.1, the probability of collision for Case 1 is 0.195181 using measurements to update the estimates of the primary object and is 0.218165 without measurements. Taking measurements of the secondary object decreases the secondary object's covariance (in [m] and [m/s]) at TCA to

$$\mathbf{C}_s = \begin{bmatrix} 6272.8949 & -363.24390 & -4.3434 \times 10^{-5} \\ -363.24390 & 21.807376 & 2.4636 \times 10^{-6} \\ -4.3434 \times 10^{-5} & 2.4636e-06 & 1.2046558 \end{bmatrix}. \tag{5.11}$$

This is extremely similar to the primary object's covariance after measurement based updates, which is an expected result. With both the primary and secondary objects' covariance decreased from the original, which is given in the Appendix, the confidence in the resulting probability of collision should increase. The effect that processing measurements on both objects has on the probability of collision can be seen in Figure 5.11.

Figure 5.11 illustrates that the probability of collision decreased by only 5% from 0.218165, without measurements, to 0.207134. This is an interesting result because this is an increase from the probability of collision found when implementing only measuring the primary object, 0.195181. This could be a result of the random corruption from the

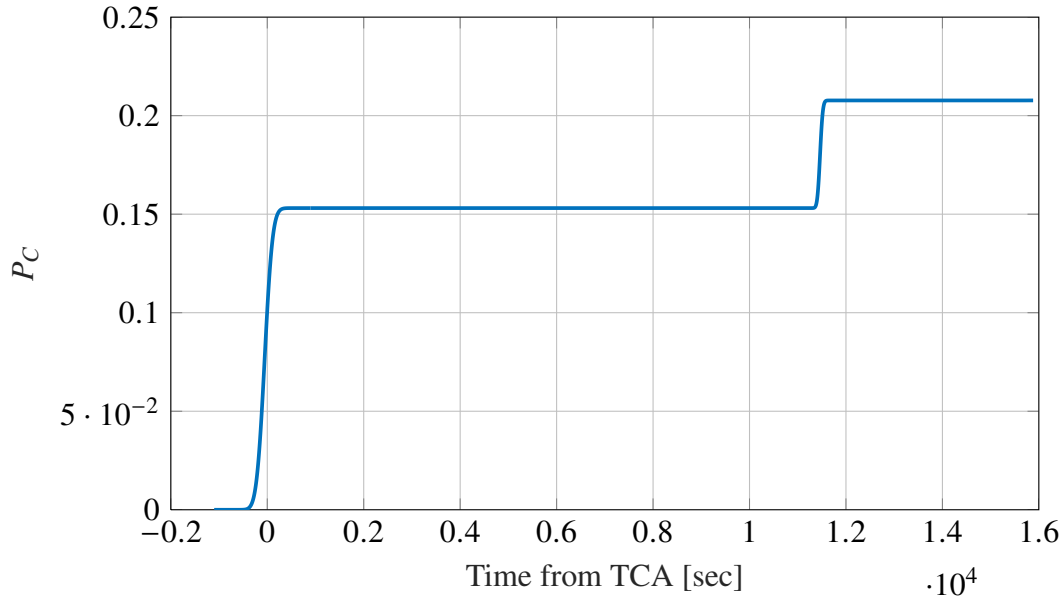

Figure 5.11. Cumulative probability of collision for Case 1, measuring both objects

measurements, as discussed earlier, or this could in fact be a further level of confidence in the probability of collision by taking additional measurements. The states of the secondary object using the measurements to update the states can be seen in Figures 5.12 and 5.13.

The estimates in the primary object remain the exact same as in section 5.3.1.1, due to processing the same data, so only the secondary object will be discussed in this section. The same trends in the measurement based updates on the estimated states for the primary object can be seen in Figures 5.12 and 5.13 for the secondary object. The state estimation errors all tend to sit on a horizontal line near zero until the time of the measurements, then the state errors tend to drift away, but then converge to the straight line. If the times in Figures 5.12 and 5.13 were extended, the same highly oscillatory motion from the multiple orbits would occur.

5.3.2.2. Case 2. From Section 5.3.1.2, the probability of collision for Case 2 is 0.012014 using measurements on only the primary object and is 0.016239 when utilizing no measurements. Taking measurements of the secondary object decreases the covariance

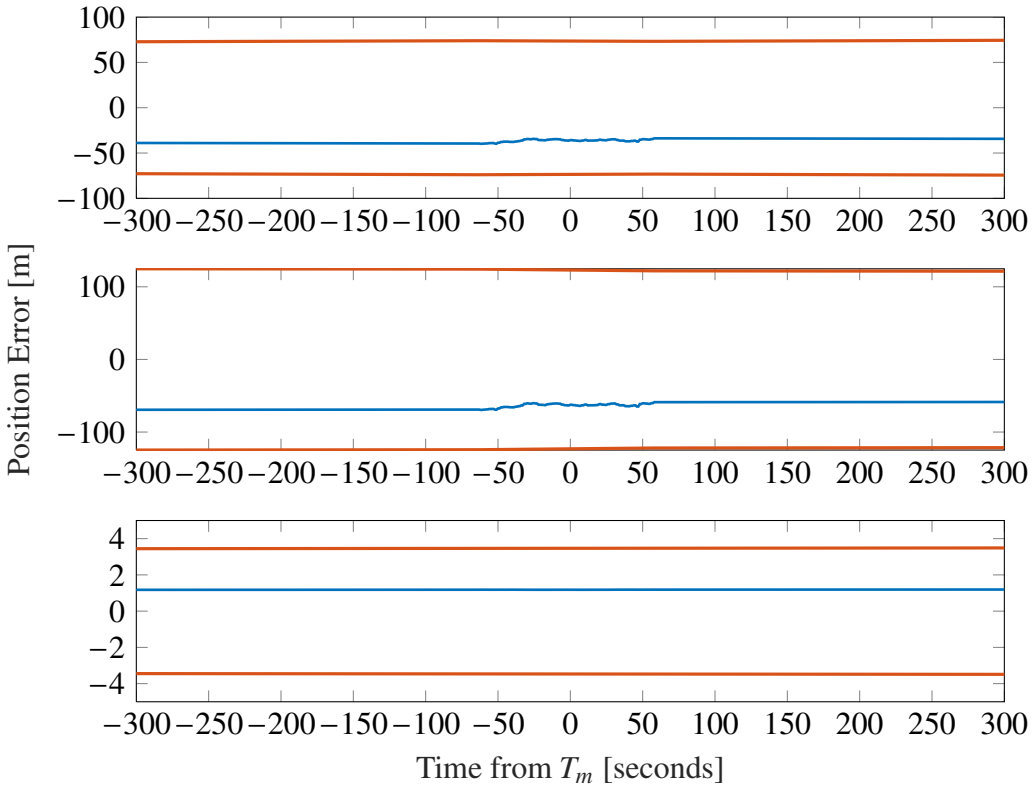

Figure 5.12. Position errors for Case 1, measuring both objects

(in [m] and [m/s]) of the secondary object at TCA to

$$\mathbf{C}_s = \begin{bmatrix} 6272.8949 & -363.24382 & -4.3434 \times 10^{-5} \\ -363.24382 & 21.807365 & 2.4636 \times 10^{-6} \\ -4.3434 \times 10^{-5} & 2.4636 \times 10^{-6} & 1.2046558 \end{bmatrix}. \tag{5.12}$$

This is an extremely similar covariance as seen in Section 5.3.1.1; typically, the covariances for the secondary objects in Cases 1 and 2 would be exactly the same because Case 1 and 2 follow the exact same trajectory. The difference between these covariances comes from the random measurement noise used to corrupt the measurements that are processed in the EKF. The effect that taking measurements on both objects has on the probability of collision can be seen in Figure 5.14.

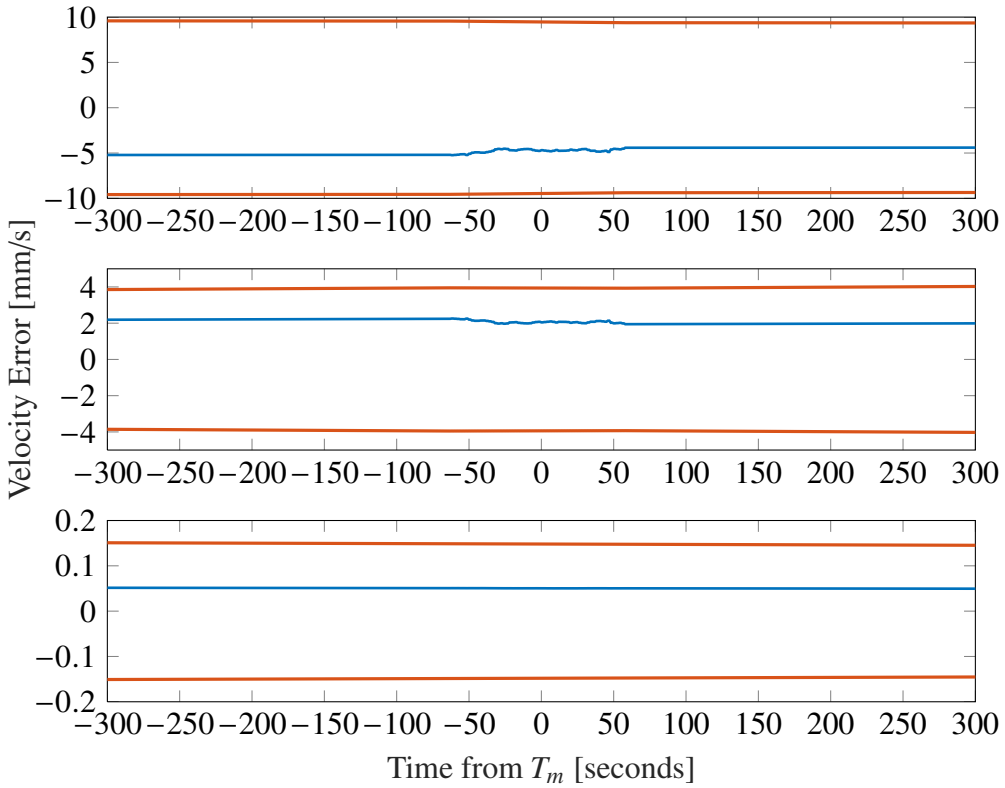

Figure 5.13. Velocity errors for Case 1, measuring both objects

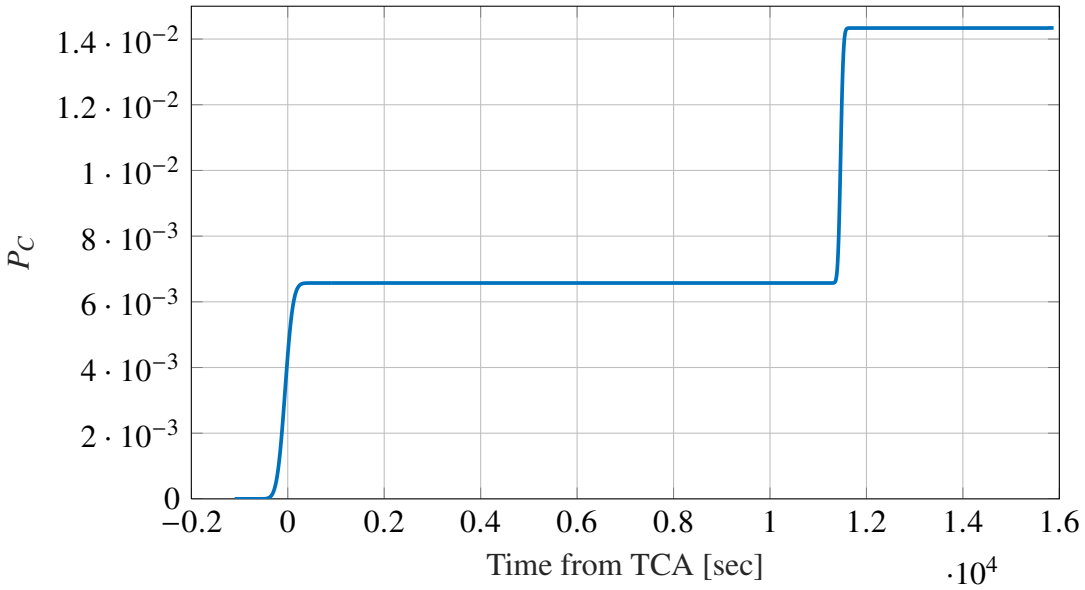

Figure 5.14. Cumulative probability of collision for Case 2, measuring both objects

Figure 5.14 displays the same trend that was seen in Case 1 with both measured objects. The probability of collision for Case 2 decreases from the original probability, 0.016239 by 13% to 0.014128. This is, however, still an increase in probability from the computation using only measurements based on the primary object, 0.012014. A similar Monte Carlo method that was completed on Case 5 should be done to validate whether the computation of collision probability is gaining accuracy from taking measurements for both objects or if the results for Cases 1 and 2 are simply due to the discrepancies in random measurement noise. The state estimation errors of the secondary object are seen in Figures 5.15 and 5.16.

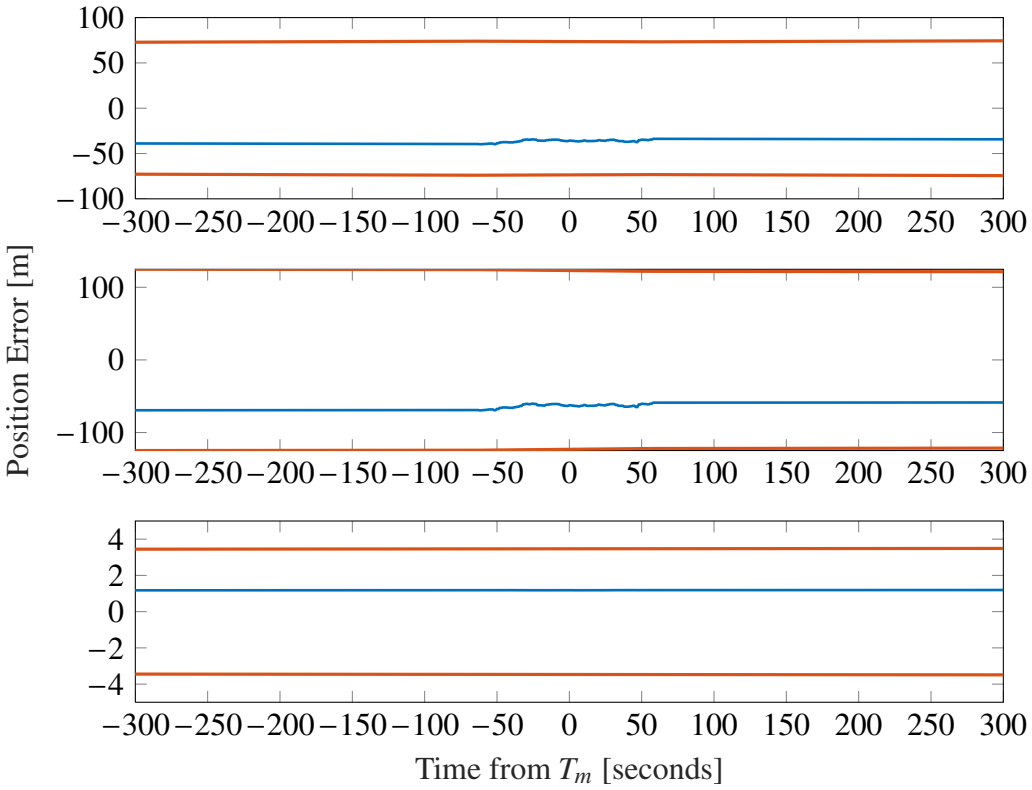

Figure 5.15. Position errors for Case 2, measuring both objects

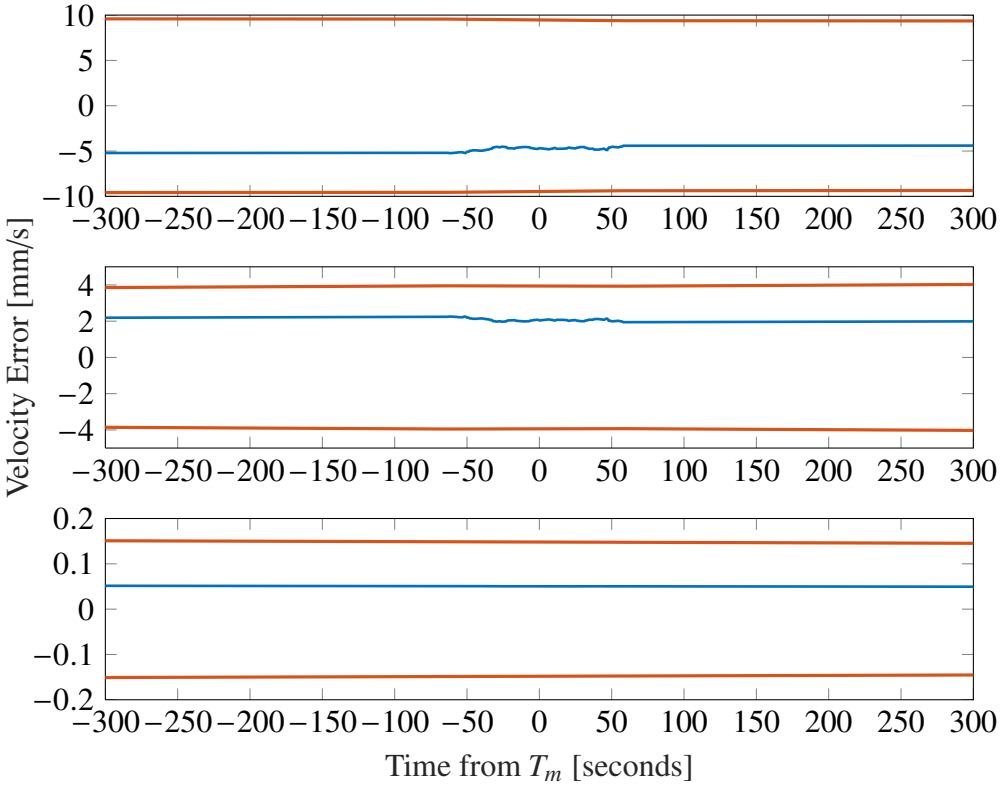

Figure 5.16. Velocity errors for Case 2, measuring both objects

Once again, Figures 5.15 and 5.16 illustrate similar estimates as Case 1. This is attributed to the general nature of Cases 1 and 2, where both of the initial positions, velocities, and covariances are exactly the same. The only difference between the cases, as seen in Figures 5.15 and 5.16, is that the effects of the random measurement noise. Without the processed measurements, the estimates would remain exactly the same.

5.3.2.3. Case 5. From Section 5.3.1.3, the probability of collision for Case 5 is 0.051980 using measurements of only the primary object and is 0.044385 when utilizing no measurements. The effects of the 20 measurements on the covariance (in [m] and [m/s])

of the secondary object at TCA can be seen by

$$\mathbf{C}_s = \begin{bmatrix} 0.0362050 & -7.6213574 & -7.6205048 \\ -7.6213574 & 3294.9035 & 3294.4564 \\ -7.6205048 & 3294.4564 & 3294.1663 \end{bmatrix}. \tag{5.13}$$

This is similar to the covariance of the primary object, seen in Section 5.3.1.3, which is also half of the original covariance of the secondary object at TCA without measurements. This significant decrease in both of the objects' covariances will have an immense effect on the probability of collision. The effect that the measurements of both objects have on the probability of collision can be seen in Figure 5.17.

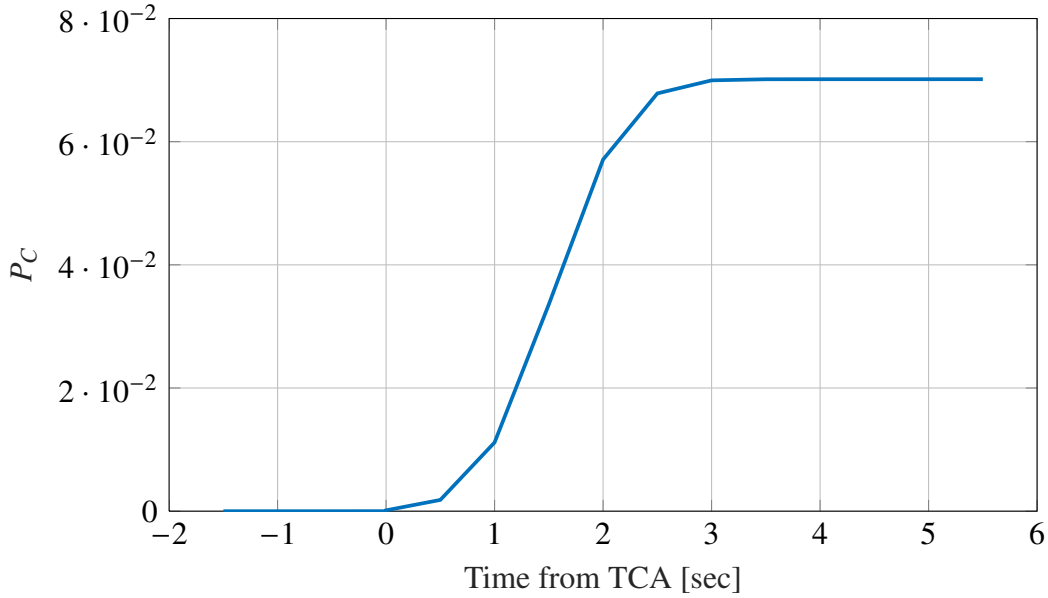

Figure 5.17. Cumulative probability of collision for Case 5, measuring both objects

Figure 5.17 illustrates an immense jump the in probability of collision, as the value increases to 0.070033, which is about 58% greater than the original probability, 0.044385. This is a significant increase in the probability of collision and could prove useful, as it

shows that a drastic decrease in covariance could increase the collision probability if the primary object remains completely engulfed within the covariance ellipsoid at TCA, which is the situation in Case 5.

Figures 5.18 and 5.19 illustrate that the states of the secondary object update extremely similar to the primary object, as seen in Section 5.3.1.3. The covariance can be seen to readjust and gain confidence at the time of the measurements in Figures 5.18 and 5.19.

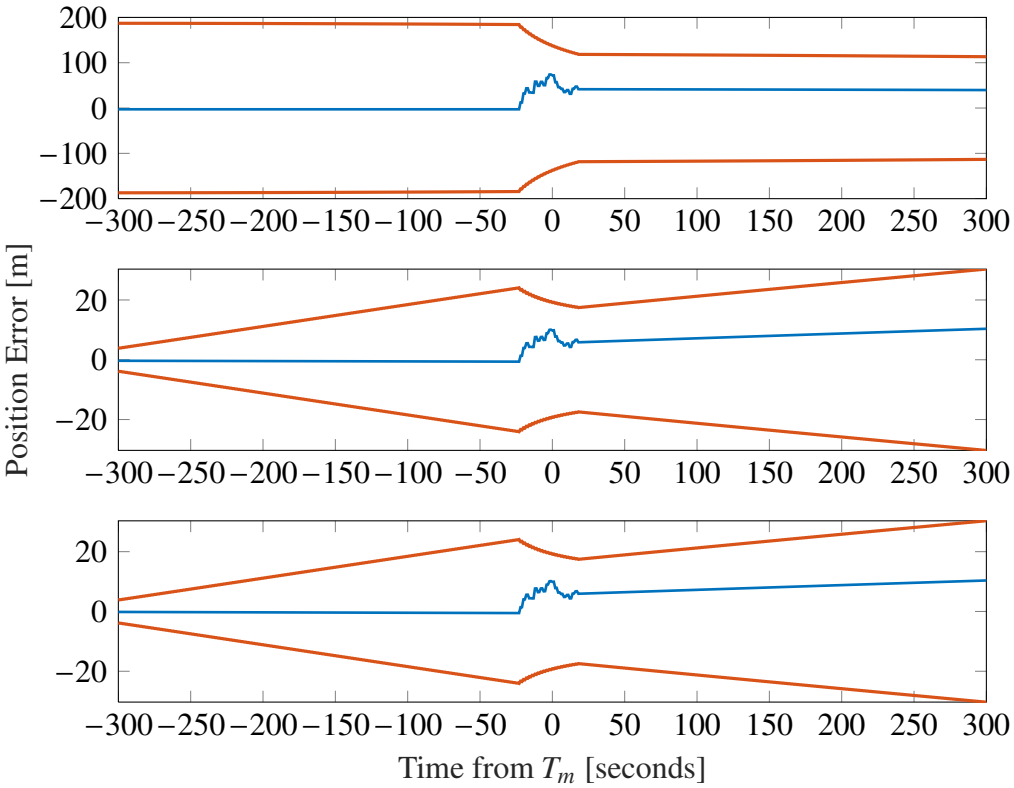

Figure 5.18. Position errors for Case 5, measuring both objects

Cases 1, 2, and 5 illustrate that the probability of collision is extremely sensitive to the size of the covariance. The probability of collision is also sensitive to the location of the primary with respect to the combined covariance ellipsoid, as seen in both Cases 2 and 5. In either case, the probability of collision can either increase or decrease, dependent on the random noise measurements, making it imperative to analyze all measurement effects with Monte Carlo trials.

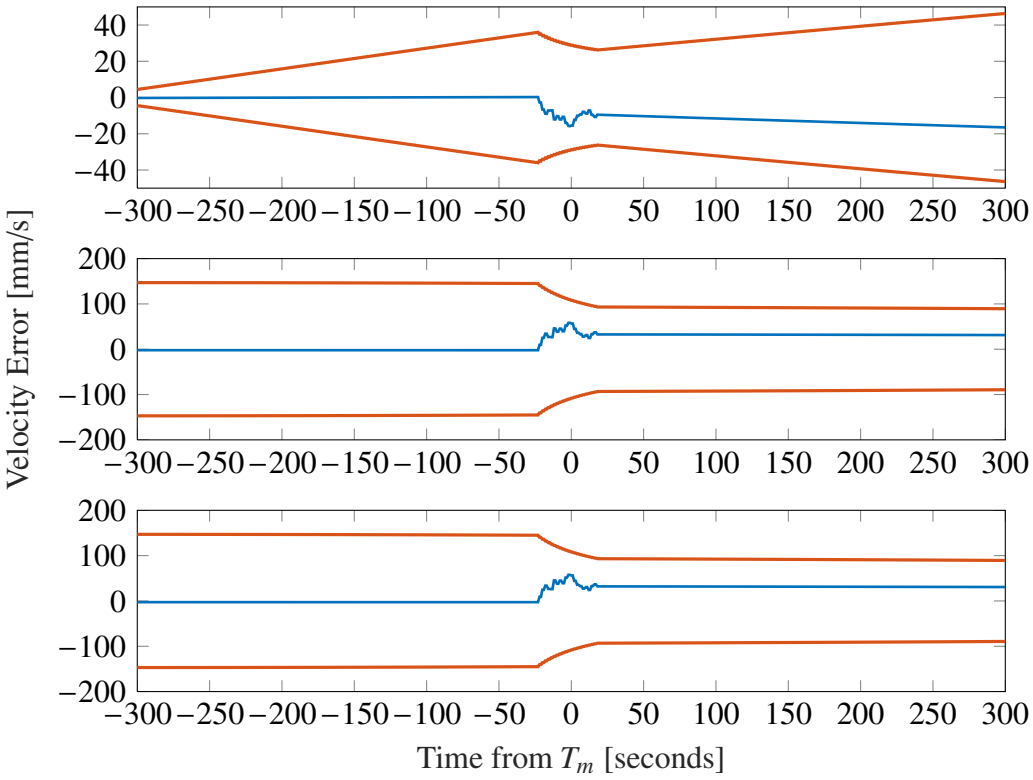

Figure 5.19. Velocity errors for Case 5, measuring both objects

6. CONCLUSION

In this work, various methods of calculating the probability of collision were presented and compared. For cases involving low relative velocity motion, the nonlinear adjoining cylinders method is recommended to calculate the collision probability between two objects. If the case in question involves two objects with high relative velocity motion, then any of the analytical methods presented in this work will suffice. It should be kept in mind that cases with extremely low relative velocities may behave highly nonlinearly at the time of closest approach (TCA), causing the adjoining cylinders method to struggle to correctly estimate the probability of collision. To effectively analyze the probability of collision for a highly nonlinear case, the adjoining cylinders method needs to be readjusted so there are no overlaps or gaps. This can be done by shifting the endpoints to begin at certain points in time instead of the current method of building the endpoints of the cylinders based on the relative velocity at TCA.

Beyond presenting and comparing analytical methods, the intent of this work was to analyze the effects of utilizing measurements to update the estimates of the objects on the probability of collision in order to offer an alternative to maneuvering. Currently, if a conjunction is deemed to have too high of a collision risk when compared to a specified threshold value, a maneuver is performed. However, based on the results in Section 5, it is clear that measurements not only have an effect on the covariance, but also on the probability of collision. Measurements could therefore be used to gain a better understanding of the probability of collision for each case in order to truly understand if a spacecraft maneuver is required.

The observers used in this work were simply generated at some arbitrary point on the surface of the Earth, which is not realistic in the scope of an actual mission application. For more realistic results, it would be recommended that the observers be set at a real ob-

servation location. If two objects are to be tracked, then multiple sites should be tasked to track one of the objects at the same time then coordinate the results to form the measurements to be input into the EKF. This should allow for an effective increase on accuracy for the probability of collision.

The measurements were used to gain confidence in the position and velocity states of one or both of the tracked objects, as seen by the decrease in the covariance. Utilizing the estimated states and covariances from the EKF to recompute the probability of collision was found to result in an increase or decrease in the probability of collision. The effects on the change in probability of collision is an outcome from the random noise used to generate the measurements. Several trial runs should be used on the process with the measurements to develop a trend to analyze whether the probability of collision for a specific case is likely to increase or decrease from the measurement-based updates. It is clear that the covariance did not alter greatly when tracking the objects in the GEO cases, this is due to the fact that the measurement noise was generated from a 10 arcsecond value. This value is sufficient to update the covariance in the LEO case, but to gain more confidence in the states, one would need a more accurate measurement of the system.

Future work from the results presented in this work should involve a re-examination of the bounds of the endpoints of each individual cylinder within the adjoining cylinders method. Future work could also include the effects of tracking both objects at different times on the probability of collision; for example, tracking the primary object for 40 seconds right after epoch and tracking the secondary object for 20 seconds right before conjunction. It could also be interesting to see how a different filtering system, such as the unscented Kalman filter, would estimate the states and covariances, and the effect that has on the probability of collision. An extension of this work would be to examine optimization utilizing the tracking of both objects to better understand a necessary maneuver.

APPENDIX

THE 6 SELECTED TEST CASES

1. CASE 1

The position and velocity of the primary object at epoch is

$$\mathbf{r}_p = \begin{bmatrix} -33552459.274056 & -23728303.048015 & 0.0 \end{bmatrix} \text{ [m]}$$
$$\mathbf{v}_p = \begin{bmatrix} -1828.9971793970 & 2534.1074695609 & 0.0 \end{bmatrix} \text{ [m/s].}$$

The position and velocity of the secondary object at epoch is

$$\mathbf{r}_s = \begin{bmatrix} -33547125.485964 & -23734789.446136 & -2.8340295187 \end{bmatrix} \text{ [m]}$$
$$\mathbf{v}_s = \begin{bmatrix} -1829.5395947473 & 2533.7604928826 & 0.0003025433 \end{bmatrix} \text{ [m/s].}$$

The covariances (in [m] and [m/s]) of the primary and secondary objects at epoch, respectively, are

$$\mathbf{C}_p = \begin{bmatrix} 0.057125290239 & -0.023727388103 & 0.0 & 0.0 & 0.0 & 0.0 \\ -0.023727388103 & 0.072874709760 & 0.0 & 0.0 & 0.0 & 0.0 \\ 0.0 & 0.0 & 0.04 & 0.0 & 0.0 & 0.0 \\ 0.0 & 0.0 & 0.0 & 1 \times 10^{-8} & 0.0 & 0.0 \\ 0.0 & 0.0 & 0.0 & 0.0 & 1 \times 10^{-8} & 0.0 \\ 0.0 & 0.0 & 0.0 & 0.0 & 0.0 & 1 \times 10^{-8} \end{bmatrix}$$

$$\mathbf{C}_s = \begin{bmatrix} 0.057135052 & -0.023730626 & -2.833 \times 10^{-9} & 0.0 & 0.0 & 0.0 \\ -0.023730626 & 0.072864947 & 3.924 \times 10^{-9} & 0.0 & 0.0 & 0.0 \\ -2.833 \times 10^{-9} & 3.924 \times 10^{-9} & 0.04 & 0.0 & 0.0 & 0.0 \\ 0.0 & 0.0 & 0.0 & 1 \times 10^{-8} & 0.0 & 0.0 \\ 0.0 & 0.0 & 0.0 & 0.0 & 1 \times 10^{-8} & 0.0 \\ 0.0 & 0.0 & 0.0 & 0.0 & 0.0 & 1 \times 10^{-8} \end{bmatrix}$$

The time of closest approach (TCA) occurs 280800 seconds after epoch. The position and velocity of the primary object at TCA is

$$\mathbf{r}_p = \begin{bmatrix} 153321.16965476 & 41874161.3623902 & 0 \end{bmatrix} \text{ [m]}$$
$$\mathbf{v}_p = \begin{bmatrix} 3066.87442751798 & -11.3641133112826 & 0 \end{bmatrix} \text{ [m/s]}.$$

The position and velocity of the secondary object at TCA is

$$\mathbf{r}_s = \begin{bmatrix} 153321.667331387 & 41874161.8628867 & 4.99996644336043 \end{bmatrix} \text{ [m]}$$
$$\mathbf{v}_s = \begin{bmatrix} 3066.86442727559 & -11.3541130234207 & -1.356914987 \times 10^{-6} \end{bmatrix} \text{ [m/s]}.$$

The covariances (in [m] and [m/s]) of the primary and secondary objects at TCA, respectively, are

$$\mathbf{C}_p = \begin{bmatrix} 6494.08 & -376.118 & 0.0 & 0.015991 & -0.49426 & 0.0 \\ -376.118 & 22.5571 & 0.0 & -0.00099 & 0.02857 & 0.0 \\ 0.0 & 0.0 & 1.20504 & 0.0 & 0.0 & -6.071 \times 10^{-5} \\ 0.015991 & -0.00099 & 0.0 & 4.438 \times 10^{-8} & -1.212 \times 10^{-6} & 0.0 \\ -0.49426 & 0.028568 & 0.0 & -1.212 \times 10^{-6} & 3.762 \times 10^{5} & 0.0 \\ 0.0 & 0.0 & -6.071 \times 10^{-5} & 0.0 & 0.00 & 3.390 \times 10^{-9} \end{bmatrix} \quad (1)$$

$$\mathbf{C}_s = \begin{bmatrix} 6494.22 & -376.135 & -4.491 \times 10^{-5} & 0.01599 & -0.49427 & -5.902 \times 10^{-8} \\ -376.135 & 22.5583 & 2.549 \times 10^{-6} & -0.00099 & 0.02857 & 3.418 \times 10^{-9} \\ -4.491 \times 10^{-5} & 2.549 \times 10^{-6} & 1.20468 & -1.180 \times 10^{-10} & 3.419 \times 10^{-9} & -6.071 \times 10^{-5} \\ 0.01599 & -0.00099 & -1.180 \times 10^{-10} & 4.439 \times 10^{-8} & -1.212 \times 10^{-6} & -1.448 \times 10^{-13} \\ -0.49427 & 0.028569 & 3.418 \times 10^{-9} & -1.212 \times 10^{-6} & 3.762 \times 10^{-5} & 4.492 \times 10^{-12} \\ -5.902 \times 10^{-8} & 3.418 \times 10^{-9} & -6.071 \times 10^{-5} & -1.448 \times 10^{-13} & 4.492 \times 10^{-12} & 3.392 \times 10^{-9} \end{bmatrix}$$

2. CASE 2

The position and velocity of the primary object at epoch is

$$\mathbf{r}_p = \begin{bmatrix} -33552458.925202 & -23728303.531359 & 0.0 \end{bmatrix} \text{ [m]}$$
$$\mathbf{v}_p = \begin{bmatrix} -1828.9972161528 & 2534.1074435672 & 0.0 \end{bmatrix} \text{ [m/s]}.$$

The position and velocity of the secondary object at epoch is

$$\mathbf{r}_s = \begin{bmatrix} -33547125.137007 & -23734789.929413 & -2.8340295764 \end{bmatrix} \text{ [m]}$$
$$\mathbf{v}_s = \begin{bmatrix} -1829.5396314989 & 2533.7604668807 & 0.0003025433 \end{bmatrix} \text{ [m/s]}.$$

The covariances (in [m] and [m/s]) of the primary and secondary objects at epoch, respectively, are

$$\mathbf{C}_p = \begin{bmatrix} 0.057125290923276 & -0.023727388329881 & 0.0 & 0.0 & 0.0 & 0.0 \\ -0.023727388329881 & 0.072874709076724 & 0.0 & 0.0 & 0.0 & 0.0 \\ 0.0 & 0.0 & 0.04 & 0.0 & 0.0 & 0.0 \\ 0.0 & 0.0 & 0.0 & 1 \times 10^{-8} & 0.0 & 0.0 \\ 0.0 & 0.0 & 0.0 & 0.0 & 1 \times 10^{-8} & 0.0 \\ 0.0 & 0.0 & 0.0 & 0.0 & 0.0 & 1 \times 10^{-8} \end{bmatrix}$$

$$\mathbf{C}_s = \begin{bmatrix} 0.05713505341 & -0.023730626101 & -2.83355 \times 10^{-9} & 0.0 & 0.0 & 0.0 \\ -0.023730626101 & 0.072864946588 & 3.92423 \times 10^{-9} & 0.0 & 0.0 & 0.0 \\ -2.83355 \times 10^{-9} & 3.92423 \times 10^{-9} & 0.04 & 0.0 & 0.0 & 0.0 \\ 0.0 & 0.0 & 0.0 & 1 \times 10^{-8} & 0.0 & 0.0 \\ 0.0 & 0.0 & 0.0 & 0.0 & 1 \times 10^{-8} & 0.0 \\ 0.0 & 0.0 & 0.0 & 0.0 & 0.0 & 1 \times 10^{-8} \end{bmatrix}$$

The time of closest approach (TCA) occurs 280800 seconds after epoch. The position and velocity of the primary object at TCA is

$$\mathbf{r}_p = \begin{bmatrix} 153320.58467023 & 41874161.3645583 & 0.0 \end{bmatrix} \text{ [m]}$$
$$\mathbf{v}_p = \begin{bmatrix} 3066.8744276767 & -11.3640699516664 & 0.0 \end{bmatrix} \text{ [m/s]}.$$

The position and velocity of the secondary object at TCA is

$$\mathbf{r}_s = \begin{bmatrix} 153321.082302062 & 41874161.8650566 & 4.99996647748931 \end{bmatrix} \text{ [m]}$$
$$\mathbf{v}_s = \begin{bmatrix} 3066.86442743414 & -11.3540696602929 & -1.356911578 \times 10^{-6} \end{bmatrix} \text{ [m/s]}.$$

The covariances (in [m] and [m/s]) of the primary and secondary objects at TCA, respectively, are

$$\mathbf{C}_p = \begin{bmatrix} 6494.0806 & -376.11793 & 0.0 & 0.01599093 & -0.4942615 & 0.0 \\ -376.11793 & 22.557075 & 0.0 & -0.0009883 & 0.0285679 & 0.0 \\ 0.0 & 0.0 & 1.2050448 & 0.0 & 0.0 & -6.071 \times 10^{-5} \\ 0.01599093 & -0.0009883 & 0.0 & 4.438 \times 10^{-8} & -1.212 \times 10^{-6} & 0.0 \\ -0.4942615 & 0.02856788 & 0.0 & -1.212 \times 10^{-6} & 3.762 \times 10^{5} & 0.0 \\ 0.0 & 0.0 & -6.071 \times 10^{-5} & 0.0 & 0.0 & 3.390 \times 10^{-9} \end{bmatrix} \tag{2}$$

$$\mathbf{C}_s = \begin{bmatrix} 6494.2259 & -376.13547 & -4.491 \times 10^{-5} & 0.0159936 & -0.4942719 & -5.902 \times 10^{-8} \\ -376.13547 & 22.558256 & 2.549 \times 10^{-6} & -0.0009885 & 0.0285692 & 3.418 \times 10^{-9} \\ -4.491 \times 10^{-5} & 2.549 \times 10^{-6} & 1.2046799 & -1.180 \times 10^{-10} & 3.419 \times 10^{-9} & -6.071 \times 10^{-5} \\ 0.0159936 & -0.0009885 & -1.180 \times 10^{-10} & 4.439 \times 10^{8} & -1.212 \times 10^{-6} & -1.448 \times 10^{-13} \\ -0.4942719 & 0.02856918 & 3.418 \times 10^{-9} & -1.212 \times 10^{-6} & 3.762 \times 10^{-5} & 4.492 \times 10^{-12} \\ -5.902 \times 10^{-8} & 3.418 \times 10^{-9} & -6.071 \times 10^{-5} & -1.448 \times 10^{-13} & 4.492 \times 10^{-12} & 3.392 \times 10^{-9} \end{bmatrix}$$

3. CASE 3

The position and velocity of the primary object at epoch is

$$\mathbf{r}_p = \begin{bmatrix} -33552760.26664 & -23727886.012085 & 0.0 \end{bmatrix} \text{ [m]}$$
$$\mathbf{v}_p = \begin{bmatrix} -1828.9654659653 & 2534.1298970058 & 0.0 \end{bmatrix} \text{ [m/s]}.$$

The position and velocity of the secondary object at epoch is

$$\mathbf{r}_s = \begin{bmatrix} -33161707.806638 & -24056602.536394 & 122462.53057353 \end{bmatrix} \text{ [m]}$$
$$\mathbf{v}_s = \begin{bmatrix} -1859.4197012053 & 2523.7257583343 & 6.9196063841 \end{bmatrix} \text{ [m/s]}.$$

The covariances (in [m] and [m/s]) of the primary and secondary objects at epoch, respectively, are

$$\mathbf{C}_p = \begin{bmatrix} 0.057124700466574 & -0.023727192359376 & 0.0 & 0.0 & 0.0 & 0.0 \\ -0.023727192359376 & 0.072875299533426 & 0.0 & 0.0 & 0.0 & 0.0 \\ 0.0 & 0.0 & 0.04 & 0.0 & 0.0 & 0.0 \\ 0.0 & 0.0 & 0.0 & 1 \times 10^{-8} & 0.0 & 0.0 \\ 0.0 & 0.0 & 0.0 & 0.0 & 1 \times 10^{-8} & 0.0 \\ 0.0 & 0.0 & 0.0 & 0.0 & 0.0 & 1 \times 10^{-8} \end{bmatrix}$$

$$\mathbf{C}_s = \begin{bmatrix} 0.057592112492 & -0.02387716308 & -0.0000654669 & 0.0 & 0.0 & 0.0 \\ -0.02387716308 & 0.072407643880 & 0.0000888559 & 0.0 & 0.0 & 0.0 \\ -0.0000654669 & 0.0000888559 & 0.0400002436273 & 0.0 & 0.0 & 0.0 \\ 0.0 & 0.0 & 0.0 & 1 \times 10^{-8} & 0.0 & 0.0 \\ 0.0 & 0.0 & 0.0 & 0.0 & 1 \times 10^{-8} & 0.0 \\ 0.0 & 0.0 & 0.0 & 0.0 & 0.0 & 1 \times 10^{-8} \end{bmatrix}$$

The time of closest approach (TCA) occurs 280800 seconds after epoch. The position and velocity of the primary object at TCA is

$$\mathbf{r}_p = \begin{bmatrix} 153825.880402651 & 41874159.4891089 & 0.0 \end{bmatrix} \text{ [m]}$$
$$\mathbf{v}_p = \begin{bmatrix} 3066.87429032037 & -11.4015229317906 & 0.0 \end{bmatrix} \text{ [m/s]}.$$

The position and velocity of the secondary object at TCA is

$$\mathbf{r}_s = \begin{bmatrix} 153825.770713806 & 41874161.8046658 & 3.21944850575784 \end{bmatrix} \text{ [m]}$$
$$\mathbf{v}_s = \begin{bmatrix} 3066.86428799712 & -0.0354534936458784 & -11.3560258390883 \end{bmatrix} \text{ [m/s]}.$$

The covariances (in [m] and [m/s]) of the primary and secondary objects at TCA, respectively, are

$$\mathbf{C}_p = \begin{bmatrix} 6494.0697 & -376.19687 & 0.0 & 0.0159849 & -0.4942613 & 0.0 \\ -376.19687 & 22.566257 & 0.0 & -0.0009882 & 0.0285739 & 0.0 \\ 0.0 & 0.0 & 1.205046 & 0.0 & 0.0 & -6.071 \times 10^{-5} \\ 0.0159849 & -0.0009882 & 0.0 & 4.435 \times 10^{-8} & -1.212 \times 10^{-6} & 0.0 \\ -0.4942613 & 0.0285739 & 0.0 & -1.212 \times 10^{-6} & 3.762 \times 10^{-5} & 0.0 \\ 0.0 & 0.0 & -6.071 \times 10^{-5} & 0.0 & 0.0 & 3.390 \times 10^{-9} \end{bmatrix} \tag{3}$$

$$\mathbf{C}_s = \begin{bmatrix} 6539.7169 & -354.46196 & -24.215837 & 0.0161379 & -0.4975674 & -6.678 \times 10^{-5} \\ -354.46196 & 19.985432 & 1.3127637 & -0.0009366 & 0.0269101 & 3.837 \times 10^{-6} \\ -24.215837 & 1.3127637 & 1.2675008 & -5.999e-05 & 0.0018428 & -6.024 \times 10^{-5} \\ 0.0161379 & -0.0009366 & -5.999 \times 10^{-5} & 4.479 \times 10^{-8} & -1.223 \times 10^{-6} & -1.698 \times 10^{-10} \\ -0.4975674 & 0.02691012 & 0.0018428 & -1.223 \times 10^{-6} & 3.7862 \times 10^{-5} & 5.047 \times 10^{-9} \\ -6.678 \times 10^{-5} & 3.837 \times 10^{-6} & -6.024 \times 10^{-5} & -1.698 \times 10^{-10} & 5.047 \times 10^{-9} & 3.446 \times 10^{-9} \end{bmatrix}$$

4. CASE 4

The position and velocity of the primary object at epoch is

$$\mathbf{r}_p = \begin{bmatrix} -30285329.869738 & -27707671.298553 & 0.0 \end{bmatrix} \text{ [m]}$$
$$\mathbf{v}_p = \begin{bmatrix} -2131.9561967731 & 2289.9864650781 & 0.0 \end{bmatrix} \text{ [m/s]}.$$

The position and velocity of the secondary object at epoch is

$$\mathbf{r}_s = \begin{bmatrix} -30289645.651968 & -27703079.378773 & -3.5557323237 \end{bmatrix} \text{ [m]}$$
$$\mathbf{v}_s = \begin{bmatrix} -2131.6028955093 & 2290.3175429528 & 0.0002668288 \end{bmatrix} \text{ [m/s]}.$$

The covariances (in [m] and [m/s]) of the primary and secondary objects at epoch, respectively, are

$$\mathbf{C}_p = \begin{bmatrix} 0.063215391925112 & -0.024936222128042 & 0.0 & 0.0 & 0.0 & 0.0 \\ -0.024936222128042 & 0.066784608074888 & 0.0 & 0.0 & 0.0 & 0.0 \\ 0.0 & 0.0 & 0.04 & 0.0 & 0.0 & 0.0 \\ 0.0 & 0.0 & 0.0 & 1 \times 10^{-8} & 0.0 & 0.0 \\ 0.0 & 0.0 & 0.0 & 0.0 & 1 \times 10^{-8} & 0.0 \\ 0.0 & 0.0 & 0.0 & 0.0 & 0.0 & 1 \times 10^{-8} \end{bmatrix}$$

$$\mathbf{C}_s = \begin{bmatrix} 0.063207674212 & -0.024935668595 & -2.90508 \times 10^{-9} & 0.0 & 0.0 & 0.0 \\ -0.024935668595 & 0.066792325788 & 3.12138 \times 10^{-9} & 0.0 & 0.0 & 0.0 \\ -2.90508 \times 10^{-9} & 3.12138 \times 10^{-9} & 0.04 & 0.0 & 0.0 & 0.0 \\ 0.0 & 0.0 & 0.0 & 1 \times 10^{-8} & 0.0 & 0.0 \\ 0.0 & 0.0 & 0.0 & 0.0 & 1 \times 10^{-8} & 0.0 \\ 0.0 & 0.0 & 0.0 & 0.0 & 0.0 & 1 \times 10^{-8} \end{bmatrix}$$

The time of closest approach (TCA) occurs 250560 seconds after epoch. The position and velocity of the primary object at TCA is

$$\mathbf{r}_p = \begin{bmatrix} -28570246.9654646 & -29444249.7488823 & 0.0 \end{bmatrix} \text{ [m]}$$
$$\mathbf{v}_p = \begin{bmatrix} -2264.38498740899 & 2161.38908399998 & 0.0 \end{bmatrix} \text{ [m/s]}.$$

The position and velocity of the secondary object at TCA is

$$\mathbf{r}_s = \begin{bmatrix} -28570365.77831 & -29444187.0221777 & -3.75799801838644 \end{bmatrix} \text{ [m]}$$
$$\mathbf{v}_s = \begin{bmatrix} -2264.37610255555 & 2161.40591449933 & 0.000250330649170032 \end{bmatrix} \text{ [m/s]}.$$

The covariances (in [m] and [m/s]) of the primary and secondary objects at TCA, respectively, are

$$\mathbf{C}_p = \begin{bmatrix} 3149.7592 & -3009.1232 & 0.0 & -0.2330265 & -0.2322077 & 0.0 \\ -3009.1232 & 2874.8534 & 0.0 & 0.2226141 & 0.2218381 & 0.0 \\ 0.0 & 0.0 & 0.0459368 & 0.0 & 0.0 & -7.602 \times 10^{-6} \\ -0.2330265 & 0.2226141 & 0 & 1.724 \times 10^{-5} & 1.718 \times 10^{-5} & 0.0 \\ -0.2322077 & 0.2218381 & 0 & 1.718 \times 10^{-5} & 1.712 \times 10^{-5} & 0.0 \\ 0.0 & 0.0 & -7.602 \times 10^{-6} & 0.0 & 0.0 & 9.966 \times 10^{-9} \end{bmatrix} \tag{4}$$

$$\mathbf{C}_s = \begin{bmatrix} 3149.8 & -3009.2 & -0.00034854 & -0.23303 & -0.23221 & -2.9683 \times 10^{-8} \\ -3009.2 & 2875 & 0.00033299 & 0.22262 & 0.22184 & 2.8358 \times 10^{-8} \\ -0.00034854 & 0.00033299 & 0.045967 & 2.5785e-08 & 2.5696e-08 & -7.6215 \times 10^{-6} \\ -0.23303 & 0.22262 & 2.5785 \times 10^{-8} & 1.7245 \times 10^{-5} & 1.7184 \times 10^{-5} & 2.1965 \times 10^{-12} \\ -0.23221 & 0.22184 & 2.5696 \times 10^{-8} & 1.7184 \times 10^{-5} & 1.7124 \times 10^{-5} & 2.1877 \times 10^{-12} \\ -2.9683 \times 10^{-8} & 2.8358 \times 10^{-8} & -7.6215 \times 10^{-6} & 2.1965 \times 10^{-12} & 2.1877 \times 10^{-12} & 9.9656 \times 10^{-9} \end{bmatrix}$$

5. CASE 5

The position and velocity of the primary object at epoch is

$$\mathbf{r}_p = \begin{bmatrix} -6384206.8367291 & -1809788.8923854 & -1809788.8923854 \end{bmatrix} \text{ [m]}$$
$$\mathbf{v}_p = \begin{bmatrix} 2832.7325382671 & -4996.3701601034 & -4996.3701601034 \end{bmatrix} \text{ [m/s].}$$

The position and velocity of the secondary object at epoch is

$$\mathbf{r}_s = \begin{bmatrix} -6384500.2941289 & -1809180.343264 & -1808975.9125458 \end{bmatrix} \text{ [m]}$$
$$\mathbf{v}_s = \begin{bmatrix} 2831.9641937123 & -4996.9514349091 & -4996.3957233165 \end{bmatrix} \text{ [m/s].}$$

The covariances (in [m] and [m/s]) of the primary and secondary objects at epoch, respectively, are

$$\mathbf{C}_p = \begin{bmatrix} 0.04692331661 & -0.01221133731 & -0.01221133731 & 0.0 & 0.0 & 0.0 \\ -0.01221133731 & 0.08653834169 & -0.003461658306 & 0.0 & 0.0 & 0.0 \\ -0.01221133731 & -0.003461658306 & 0.08653834169 & 0.0 & 0.0 & 0.0 \\ 0.0 & 0.0 & 0.0 & 1 \times 10^{-8} & 0.0 & 0.0 \\ 0.0 & 0.0 & 0.0 & 0.0 & 1 \times 10^{-8} & 0.0 \\ 0.0 & 0.0 & 0.0 & 0.0 & 0.0 & 1 \times 10^{-8} \end{bmatrix}$$

$$\mathbf{C}_s = \begin{bmatrix} 0.046919356993 & -0.01220909565 & -0.01220771607 & 0.0 & 0.0 & 0.0 \\ -0.01220909565 & 0.086539930551 & -0.003459678474 & 0.0 & 0.0 & 0.0 \\ -0.01220771607 & -0.003459678474 & 0.086540712456 & 0.0 & 0.0 & 0.0 \\ 0.0 & 0.0 & 0.0 & 1 \times 10^{-8} & 0.0 & 0.0 \\ 0.0 & 0.0 & 0.0 & 0.0 & 1 \times 10^{-8} & 0.0 \\ 0.0 & 0.0 & 0.0 & 0.0 & 0.0 & 1 \times 10^{-8} \end{bmatrix}$$

The time of closest approach (TCA) occurs 172800 seconds after epoch. The position and velocity of the primary object at TCA is

$$\mathbf{r}_p = \begin{bmatrix} 6878090.42688427 & -18088.0480546556 & -18088.0480546556 \end{bmatrix} \text{ [m]}$$
$$\mathbf{v}_p = \begin{bmatrix} 28.3121285934114 & 5382.88885559858 & 5382.88885559858 \end{bmatrix} \text{ [m/s]}.$$

The position and velocity of the secondary object at TCA is

$$\mathbf{r}_s = \begin{bmatrix} 6878089.41881137 & -18086.0593684701 & -18087.043190241 \end{bmatrix} \text{ [m]}$$
$$\mathbf{v}_s = \begin{bmatrix} 28.6121377430165 & 5383.18886578179 & 5382.5888576694 \end{bmatrix} \text{ [m/s]}.$$

The covariances (in [m] and [m/s]) of the primary and secondary objects at TCA, respectively, are

$$\mathbf{C}_p = \begin{bmatrix} 0.062678 & -18.67 & -18.67 & 0.02921 & -0.00016679 & -0.00016679 \\ -18.67 & 7904 & 7904 & -12.38 & 0.064451 & 0.064419 \\ -18.67 & 7904 & 7904 & -12.38 & 0.064419 & 0.064451 \\ 0.02921 & -12.38 & -12.38 & 0.019392 & -0.0001009 & -0.0001009 \\ -0.00016679 & 0.064451 & 0.064419 & -0.0001009 & 5.4881 \times 10^{-7} & 5.2467 \times 10^{-7} \\ -0.00016679 & 0.064419 & 0.064451 & -0.0001009 & 5.2467 \times 10^{-7} & 5.4881 \times 10^{-7} \end{bmatrix} \tag{5}$$

$$\mathbf{C}_s = \begin{bmatrix} 0.060621 & -18.231 & -18.229 & 0.028521 & -0.0001632 & -0.00016319 \\ -18.231 & 7905.4 & 7904.4 & -12.382 & 0.064456 & 0.064423 \\ -18.229 & 7904.4 & 7903.6 & -12.38 & 0.064418 & 0.064447 \\ 0.028521 & -12.382 & -12.38 & 0.019393 & -0.0001009 & -0.0001009 \\ -0.0001632 & 0.064456 & 0.064418 & -0.0001009 & 5.4881 \times 10^{-7} & 5.2466 \times 10^{-7} \\ -0.00016319 & 0.064423 & 0.064447 & -0.0001009 & 5.2466 \times 10^{-7} & 5.4878 \times 10^{-7} \end{bmatrix}$$

6. CASE 6

The position and velocity of the primary object at epoch is

$$\mathbf{r}_p = \begin{bmatrix} -6345736.9319327 & -1876218.4567378 & -1876218.4567378 \end{bmatrix} \text{ [m]}$$
$$\mathbf{v}_p = \begin{bmatrix} 2936.7099630585 & -4966.263070953 & -4966.263070953 \end{bmatrix} \text{ [m/s]}.$$

The position and velocity of the secondary object at epoch is

$$\mathbf{r}_s = \begin{bmatrix} -6345839.97926 & -1876012.2715538 & -1875945.3383511 \end{bmatrix} \text{ [m]}$$
$$\mathbf{v}_s = \begin{bmatrix} 2936.4524265637 & -4966.4623670708 & -4966.2765632153 \end{bmatrix} \text{ [m/s]}.$$

The covariances (in [m] and [m/s]) of the primary and secondary objects at epoch, respectively, are

$$\mathbf{C}_p = \begin{bmatrix} 4.7440894789163 & -1.258327906777 & -1.258327906777 & 0.0 & 0.0 & 0.0 \\ -1.258327906777 & 6.1279552605419 & 2.1279552605419 & 0.0 & 0.0 & 0.0 \\ -1.258327906777 & 2.1279552605419 & 6.1279552605419 & 0.0 & 0.0 & 0.0 \\ 0.0 & 0.0 & 0.0 & 1 \times 10^{-6} & 1 \times 10^{-22} & 1 \times 10^{-22} \\ 0.0 & 0.0 & 0.0 & 1 \times 10^{-22} & 1 \times 10^{-6} & 1 \times 10^{-22} \\ 0.0 & 0.0 & 0.0 & 1 \times 10^{-22} & 1 \times 10^{-22} & 1 \times 10^{-6} \end{bmatrix}$$

$$\mathbf{C}_s = \begin{bmatrix} 4.7439512624 & -1.2582550000 & -1.258207926 & 0.0 & 0.0 & 0.0 \\ -1.2582550000 & 6.1281039833 & 2.128024367 & 0.0 & 0.0 & 0.0 \\ -1.258207926 & 2.128024367 & 6.127944754 & 0.0 & 0.0 & 0.0 \\ 0.0 & 0.0 & 0.0 & 1 \times 10^{-6} & 0.0 & 0.0 \\ 0.0 & 0.0 & 0.0 & 0.0 & 1 \times 10^{-6} & 1 \times 10^{-22} \\ 0.0 & 0.0 & 0.0 & 0.0 & 1 \times 10^{-22} & 1 \times 10^{-6} \end{bmatrix}$$

The time of closest approach (TCA) occurs 172800 seconds after epoch. The position and velocity of the primary object at TCA is

$$\mathbf{r}_p = \begin{bmatrix} 6877718.80777668 & 53694.8624938714 & 53694.8624938714 \end{bmatrix} \text{ [m]}$$
$$\mathbf{v}_p = \begin{bmatrix} -84.0444719409842 & 5382.59802357631 & 5382.59802357631 \end{bmatrix} \text{ [m/s]}.$$

The position and velocity of the secondary object at TCA is

$$\mathbf{r}_s = \begin{bmatrix} 6877719.80536988 & 53695.8588902137 & 53696.8637016744 \end{bmatrix} \text{ [m]}$$
$$\mathbf{v}_s = \begin{bmatrix} -83.944457617452 & 5382.69801757 & 5382.49799313066 \end{bmatrix} \text{ [m/s]}.$$

The covariances (in [m] and [m/s]) of the primary and secondary objects at TCA, respectively, are

$$\mathbf{C}_p = \begin{bmatrix} 428.54 & -18362 & -18362 & 28.762 & 0.14901 & 0.14901 \\ -18362 & 7.9019 \times 10^5 & 7.9019e \times 10^5 & -1237.9 & -6.4762 & -6.4774 \\ -18362 & 7.9019 \times 10^5 & 7.9019 \times 10^5 & -1237.9 & -6.4774 & -6.4762 \\ 28.762 & -1237.9 & -1237.9 & 1.9392 & 0.010149 & 0.010149 \\ 0.14901 & -6.4762 & -6.4774 & 0.010149 & 5.5063 \times 10^{-5} & 5.3513 \times 10^{-5} \\ 0.14901 & -6.4774 & -6.4762 & 0.010149 & 5.3513 \times 10^{-5} & 5.5063 \times 10^{-5} \end{bmatrix} \tag{6}$$

$$\mathbf{C}_s = \begin{bmatrix} 427.86 & -18348 & -18347 & 28.739 & 0.14889 & 0.1489 \\ -18348 & 7.9024 \times 10^5 & 7.902 \times 10^5 & -1237.9 & -6.4765 & -6.478 \\ -18347 & 7.902 \times 10^5 & 7.9018 \times 10^5 & -1237.9 & -6.4775 & -6.4766 \\ 28.739 & -1237.9 & -1237.9 & 1.9393 & 0.010149 & 0.01015 \\ 0.14889 & -6.4765 & -6.4775 & 0.010149 & 5.5066 \times 10^{-5} & 5.3518 \times 10^{-5} \\ 0.1489 & -6.478 & -6.4766 & 0.01015 & 5.3518 \times 10^{-5} & 5.5071 \times 10^{-5} \end{bmatrix}$$

REFERENCES

Alfano, S., 'A numerical implementation of spherical object collision probability,' Journal of the Astronautical Sciences, 2005, **53**, pp. 103–109.

Alfano, S., 'Beta conjunction analysis tool,' Advances in the Astronautical Sciences, 2008.

Alfano, S., 'Satellite conjunction monte carlo analysis,' Advances in the Astronautical Sciences, 2009, **134**, pp. 2007–2024.

Burgio, E. and Grant, K., 'Unique search and track procedures utilizing the ground-based electro-optical deep space surveillance worldwide sites,' Technical report, BAE Systems, 2011.

Burton, A., Frueh, C., and Zielinski, M., 'Assessing measures to reliably predict collision in the presence of uncertainty,' in 'AAS/AIAA Astrodynamics Specialist Conference,' 2018 .

Chan, K. F., *Spacecraft Collision Probability*, The Aerospace Press, 2008.

Chan, K. F., 'Miss distance generalized variance non-central chi distribution,' in 'AAS/AIAA Astrodynamics Specialist Conference,' 2011 .

Coppola, V. T., Woodburn, J., and Hujsak, R., 'Effects of cross correlated covariance on spacecraft collision probability,' Advances in the Astronautical Sciences, 2005.

Council, N. R., *Orbital Debris: A Technical Assessment*, The National Academies Press, Washington, DC, 1995, ISBN 978-0-309-05125-5, doi:10.17226/4765.

DeMars, K. J., Cheng, Y., and Jah, M. K., 'Collision probability with gaussian mixture orbit uncertainty,' Journal of Guidance, Control, and Dynamics, 2014, **37**(3).

Easton, R. L. and Votaw, M. J., 'Vanguard i igy satellite (1958 beta),' Review of Scientific Instruments, 1959, **30**(2), pp. 70–75.

Gottlieb, R. G., Sponaugle, S. J., and Gaylor, D., 'Orbit determination accuracy requirements for collision avoidance,' in 'AAS/AIAA Space Flight Mechanics Meeting,' 2001 .

Green, C. M. and Lomask, M., *Vanguard - A History*, U.S. Government Printing Office, 1970.

Grewal, M. S. and Andews, A. P., 'Applications of kalman filtering in aerospace 1960 to the present,' IEEE Control Systems, 2010.

Hall, L., 'The history of space debris,' in 'Space Traffic Management Conference,' 2019 .

Harris, M., 'Spacex claims to have redesigned its starlink statellites to eliminate casualty risks,' IEEE Spectrum, 2019.

Hejduk, M. D. and Johnson, L. C., 'Approach to evaluating probability of collision,' in 'AAS Space Flight Mechanics Meeting,' 2016 .

Hintz, G. R., 'Survey of orbit element sets,' Journal of Guidance, Control, and Dynamics, 2008, **31**(3).

Julier, S. J. and Uhlmann, J. K., 'New extension of the kalman filter to nonlinear systems,' in 'SPIE 3068, Signal Processing, Sensor Fusion, and Target Recognition VI,' 1997 .

Kalman, R. E., 'A new approach to linear filtering and prepredict problems,' Journal of Basic Engineering, 1960.

Kelso, T. S., 'Space surveillance,' Satellite Times, 1997.

Kessler, D., 'Sources of orbital debris and the projected environment for future spacecraft,' Journal of Spacecraft and Rockets, 1981, **18**(4), pp. 357–360.

Lear, W. M., *Kalman Filtering Techniques*, Mission Planning and Analysis Division, National Aeronautics and Space Administration, Lyndon B. Johnson Space Center, 1985.

McGee, L. A. and Schmidt, S. F., 'Discovery of the kalman filter as a practical tool for aerospace and industry,' Technical report, National Aeronautics and Space Administration, 1985.

Patera, R. P., 'General method for calculating satellite collision probability,' Journal of Guidance, Control, and Dynamics, 2001.

Patera, R. P., 'Satellite collision probability for nonlinear relative motion,' Journal of Guidance, Control, and Dynamics, 2003.

Patera, R. P., 'Calculating collision probability for arbitrary space vehicle shapes via numerical quadrature,' Journal of Guidance, Control, and Dynamics, 2005.

Prussing, J. E. and Conway, B. A., *Orbital Mechanics*, Oxford University Press, 2013.

Sorenson, H. W., *Kalman filtering: theory and Application*, IEEE Press, 1985.

U.S. Congress, O. o. T. A., 'Orbiting debris: A space environmental problem-background paper,' U.S. Government Printing Office, 1990.

Vallado, D. A., *Fundamentals of Astrodynamics and Applications*, Microcosm Press and Kluwer Academic Publishers, 2004.

VITA

Bruce Morrison studied Aerospace Engineering at Missouri University of Science and Technology starting in the Fall of 2013, where he obtained his Bachelor of Science degree in August of 2017. The following fall he returned to Missouri University of Science and Technology pursuing a graduate degree in aerospace engineering. He worked as a graduate research assistant under Dr. Kyle DeMars, where he studied uncertainty quantification and satellite collision probability. In May 2019, he received his Master of Science in Aerospace Engineering from Missouri University of Science and Technology.